Characterizing and Mitigating Phase Distortions in Quantum and Nonlinear Optical Systems

by

Andy Nicholas Black

Submitted in Partial Fulfillment of the

Requirements for the Degree

Doctor of Philosophy

Supervised by Prof. Robert W. Boyd

Department of Physics and Astronomy
Arts, Sciences and Engineering
School of Arts and Sciences

University of Rochester

Rochester, New York

2022

To Libby

Contents

Biographical Sketch

Andy Nicholas (Nick) Black began his collegiate career in 2008 as an Audio Engineering Technology major at Belmont University in Nashville, TN. During his time at Belmont, Nick conducted undergraduate research with Prof. Robert Magruder on the optical properties of metal nanoparticles implanted in silica and acoustics. He was on the Dean's List for all but one semester at Belmont. After earning a Bachelor of Science degree with the distinction of cum laude from Belmont in the spring of 2013, Nick enrolled as a physics major at Middle Tennessee State University.

While at MTSU, Nick was awarded the Excellence in Modern Physics Award, the Sigma Pi Sigma Achievement Award, and the Faculty Achievement Award in Physics. Nick also served at the Vice President and the Director of Outreach for the Society of Physics Students chapter at MTSU. Under the guidance of Prof. Nat Smith, Nick conducted research exploring the fluid dynamics of spin-coating. Nick also conducted research in quantum optics under the guidance of Prof. Daniel Erenso and was awarded an MTSU URECA Silver Level Undergraduate Reserach grant for his work. During his final summer at MTSU, Nick conducted research at Oak Ridge National Laboratory as an intern in the Department of Energy's Science Undergraduate Laboratory Internship (SULI) program. His research at Oak Ridge was advised by Dr. Raphael C. Pooser and Dr. Benjamin J. Lawrie, and it explored the generation of continuous variable entanglement in modes of light produced from four-wave mixing in hot atomic Rb vapor. Nick graduated from MTSU in the spring of 2016 with Bachelor of Science degree in physics, earning a 4.0 GPA every semester while at MTSU.

The summer after graduating from MTSU, Nick returned to Oak Ridge National Laboratory to continue his research with Dr. Raphael Pooser and Dr. Benjamin J. Lawrie. During this summer at Oak Ridge, Nick researched the generation of continuous-variable cluster states using four-wave mixing in hot Rb vapor. In the fall of 2016, Nick enrolled as a physics PhD student at the University of Rochester. Nick was the teaching assistant for the undergraduate Advanced Laboratory course and the Introductory Physics lab course. After his first year, Nick joined the research group of Prof. Robert W. Boyd and began conducting research in spatial entanglement and nonlinear self-focusing. Nick served as the teaching assistant for Prof. Boyd's Nonlinear Optics course for two semesters before becoming a research assistant. As the Vice President of Mentorship in the Physics and Astronomical Sciences Student Association for Graduate Engagement, Nick fostered a welcoming and supportive graduate mentorship program. Nick is set to defend this thesis in route to earning a PhD in physics in the winter of 2022.

Published Works Resulting from this Thesis:

1. **A. N. Black**, E. Giese, B. Braverman, N. Zollo, S. Barnett, and R. W. Boyd, "Quantum nonlocal aberration cancellation", Physical Review Letters (selected for Editor's Suggestion) **123**, 143603 (2019).
2. **A. N. Black**, S. Choudhary, E. S. Arroyo-Rivera, H. Woodworth, and R. W. Boyd, "Suppression of nonlinear optical rogue wave formation using polarization-structured beams", Physical Review Letters **129**, 133902 (2022).
3. **A. N. Black** and R. W. Boyd, "Generation of volumetrically-full Poincaré beams", Journal of the Optica Society of America A **39**(12), C161 (2022).

4. **A. N. Black**, L. D. Nguyen, B. Braverman, K. T. Crampton, J. E. Evans, and R. W. Boyd, “Quantum-enhanced quantitative phase imaging”, submitted to Optica, (2022).

Conference Presentations Resulting from this Thesis:

1. **A. N. Black**, E. Giese, B. Braverman, N. Zollo, and R. W. Boyd, “Quantum, nonlocal aberration cancellation”, in Conference on Lasers and Electro-Optics, OSA Technical Digest (Optica Publishing Group, 2019), paper FF3A.6.
2. **A. N. Black**, S. Choudhary, and R. W. Boyd, “Suppression of nonlinear caustic formation in polarization-structured beams", in OSA Nonlinear Optics 2021, R. Boyd, C. Conti, D. Christodoulides, and P. Rakich, eds., OSA Technical Digest (Optica Publishing Group, 2021), paper NM1B.5.
3. **A. N. Black** and R. W. Boyd, “Generation of volumetrically-full Poincaré beams”, in Frontiers in Optics + Laser Science 2021, C. Mazzali, T. (T.-C.) Poon, R. Averitt, and R. Kaindl, eds., Technical Digest Series (Optica Publishing Group, 2021), paper JTh5A.106.
4. **A. N. Black**, L. D. Nguyen, J. E. Evans, and R. W. Boyd, “Quantum-enhance phase imaging”, in Frontiers in Optics + Laser Science 2022, Technical Digest Series (Optica Publishing Group, 2022), paper FM3B.3, (selected as a finalist, Emil Wolf Student Paper Competition)

Other Works Published While at the University of Rochester:

1. C. Banerjee, Y. Solomons, **A. N. Black** (corresponding author), G. Marcucci, D. Eger, N. Davidson, O. Firstenberg, and R. W. Boyd, “Anomalous optical drag”, Physical Review Research **4**, 033124 (2022).
2. S. Choudhary, **A. N. Black**, A. Antikainen, and R. W. Boyd, “Controlling nonlinear rogue wave formation using the coherence length of phase noise”, under review at Physical Review Research (2022).

Acknowledgments

I would first like to thank God for providing me with many opportunities to learn and grow as both a physicist and a person. I am also very thankful for the guidance and fellowship my advisor, Prof. Robert W. Boyd, has shown me during my time conducting research in his group. Through his infectious excitement for physics, I have learned how to become a better scientist, write grants, think about new avenues of research, and have become a better writer. Bob places a lot of trust in his students and shows them unwavering support in their academic endeavors. I am also thankful to have become a reasonably competent sailor under Bob's tutelage during our many outings on his sailboat. The most lasting lessons Bob has passed along to me are the importance of developing friendships through a shared excitement for physics and the importance of being a friendly colleague to those around me.

Next, I would like to thank my wife Libby for her love and support during this challenging time of growth and change in my life. She has been by my side from the time that I was a musician to the time I decided to pursue physics and now as I finish this stage of my academic journey. Without her, I am not sure that I would have had the discipline and support to become the physicist that I am today.

I would like to thank my mother, Susan Black, and my father, Andy Black, for always having confidence in me. Every day before school, my mother would tell me, "Think big, and do the impossible!" While I took it her support for granted in my youth, I now realize how important it was as I searched for my place in the world. Furthermore, being an artist, she taught me the importance of being creative. My father instilled in me the importance of taking pride in one's work and being self-motivated. As a respected machinist, he taught me to strive for perfection. Though he never attended college, he taught himself mathematics for engineering and spent a lot of time studying the Bible. I would like to thank my brother, Steven Black, for his supportive conversations during my PhD, and I would also like to acknowledge Jon and Claudia Thorndike. Jon and Claudia have provided tremendous support to Libby and myself during our time in Rochester, allowing me to focus on my studies and being there when I needed advice.

Last, I would like to thank my colleagues for their friendship, support, and enlightening discussions during my PhD studies. In particular, I am grateful for discussions, both academic and otherwise, held with Saumya Choudhary. She is a very talented and hardworking physicist whom I have learned a lot from. I am also thankful for enlightening discussions with Saleem Iqbal, who can quickly understand many aspects of the research ideas we discuss. I would also like to acknowledge Samuel Lemieux for teaching me experimental techniques and for being a great lab partner and friend. Enno Giese taught me how to write papers, make nice figures, and analyze the physics of my experiments. Boris Braverman taught me how troubleshoot experimental apparatuses and develop an intuition for the physics inherent in a problem. I would also like to thank the many other students and postdocs I have worked with and learned from in Bob's group: Jerry Kuper, Yiyu Zhou, Jiapeng Zhao, Samuel Arroyo-Rivera, Surendar Vijayakumar, Long Nguyen, Dhanush Dinesha, Aku Antikainen, Yang Xu, Hayden Woodworth, Melanie Murillo, Michelle Wang, Madeline Bergay, Mohammad Hashemi, Stephen Chapman, Yi Wang, Nicholas Zollo, Stone Oliver, Huilong Gao, Dongxi Fu, and Shuai Sun.

Abstract

Light passing through an optical system can undergo phase distortions due to linear and nonlinear optical phenomena. These phase distortions can degrade imaging resolution and cause a well-defined laser beam to break up into an unpredictable intensity structure. The strong spatial correlation between entangled photons is used to nonlocally cancel the effects of linear phase distortions (aberrations) introduced to one photon in a quantum imaging experiment. The effects of these aberrations on a measurement of transverse entanglement and the limits of this cancellation scheme are also demonstrated. A quantum-enhanced quantitative phase imaging method that achieves twice the signal to noise ratio and approximately 1.7 times the resolution of classical phase imaging is also presented. By using only 40 photons/s/μm^2 and having data collection times that are three orders of magnitude faster than coincidence imaging techniques, this technique can be used to image light-sensitive biological samples. In a separate experiment, a polarization-structured beam containing all polarization states on the surface of the Poincaré sphere is shown to have a lower likelihood of developing optical caustics upon propagation through a nonlinear self-focusing medium. Mitigating nonlinear phase distortions by applying polarization-structuring to a beam can improve stability in high intensity laser systems, like those used in directed energy defense systems. A method of generating polarization-structured beams that contain states of both full and partial polarization is also presented. This method is used to generate a beam that contains all possible states of polarization, which may have an increased stability under nonlinear propagation. By utilizing the properties of spatially entangled photons and polarization-structured beams, this thesis presents new methods of mitigating and characterizing linear and nonlinear phase distortions.

Contributors and Funding Sources

The committee overseeing the defense of this thesis was made up of the following members: Prof. Robert W. Boyd (advisor), Professor of Optics and Physics; Prof. Nick Vamivakas, Professor of Quantum Optics and Quantum Physics; Prof. Alice C. Quillen, Professor of Physics and Astronomy; Prof. Todd D. Krauss, Professor of Chemistry and Optics; Prof. J. Albert C. Uy (committee chair), Professor of Biology.

In all of the experiments presented in this thesis, I designed and constructed the experimental apparatuses, developed the theoretical analysis of the physics presented, collected and analyzed data, developed simulations to describe experimental results, and wrote scientific papers describing the results of the experiments. I developed the original idea for the content of Chaps. 3 and 5. The original idea for the content of Chaps. 2 and 4 were developed in collaboration with others (listed below).

The contributors to the content of Chap. 2 and their contributions are as follows:

- Enno Giese served as a post-doctoral advisor during the undertaking of the experiment and the development of the theory describing nonlocal aberration cancellation. He helped develop the idea for nonlocal aberration cancellation. He also helped with editting the manuscript we published describing this effect.
- Boris Braverman served as a post-doctoral advisor during the undertaking of the

experiment. He also helped with editting the manuscript we published describing this effect.

- Nicholas Zollo helped with data collection and building the experimental apparatus as a summer student.
- Stephen Barnett developed the initial idea for quantum aberration cancellation (though it was a local scheme) in collaboration with my advisor, Robert Boyd.
- Robert Boyd developed the initial idea for quantum aberration cancellation in collaboration with Stephen Barnett. He also advised the undertaking of the experiment and writing of the manuscript.

The contributors to the content of Chap. 3 and their contributions are as follows:

- Long D. Nguyen helped to collect data and construct the experimental apparatus.
- Boris Braverman served as a postdoctoral advisor for the early stages of the experiment and helped with editing the manuscript that reported the experimental results.
- Kevin Crampton served as an external collaborator that advised the undertaking of the experiment and helped with editing the manuscript that reported the experimental results.
- James E. Evans served as an external collaborator that advised the undertaking of the experiment and helped with editing the manuscript that reported the experimental results.
- Robert Boyd advised the undertaking of the experiment and helped with editing the manuscript that reported experimental results.

The contributors to the content of Chap. 4 and their contributions are as follows:

- Saumya Choudhary helped develop the idea to explore the resistance of polarization-structured beams to nonlinear optical caustic development. She also helped with the construction of the experimental apparatus, data collection, and helped edit the manuscript that published our findings.

- Samuel Arroyo helped with the construction of an early version of the experimental apparatus.
- Hayden Woodworth helped with the construction of an early version of the experimental apparatus as a summer student.
- Robert Boyd helped develop the idea to explore the resistance of polarization-structured beams to nonlinear optical caustic development. He also advised the undertaking of the experiment and helped with editing the manuscript that reported experimental results.

There was only one other contributor to the content of Chap. 5, Robert Boyd. He helped advise the undertaking of the experiment and helped edit the manuscript that reported our findings.

The content of Chap. 2 was funded by the US Office of Naval Research under Award No. N00014-17-1-2443. The research in Chap. 3 was funded by the US Department of Energy Office of Science Biological and Environmental Research program under award FWP 76295. The content of Chap. 4 was funded by the US Office of Naval Research under Awards No. N00014-19-1-2247 and No. MURI N00014-20-1-2558. Chapter 5 was funded by the US Office of Naval Research under awards N00014-19-1-2247 and N00014-20-1-2558 and by the Natural Sciences and Engineering Research Council of Canada and the Canada Research Chairs program.

List of Tables

List of Figures

1. Introduction

Phase irregularities can degrade an optical system's imaging resolution and distort the intended intensity profile of laser beams. Individual optical elements in imaging systems can introduce phase distortions that are characterized in terms functions belonging to orthogonal basis sets, generally referred to as aberrations. Similarly, light propagating through the atmosphere can experience phase distortions due to turbulence induced by temperature gradients and air currents. This effect is responsible for the twinkling of the stars at night. In extreme cases, linear phase distortions can cause beams to collapse in such a way that their energy is confined to small regions of space [1, 2]. This effect, known as optical caustic generation, is mostly clearly visible in the network-like pattern formed on the bottom of a swimming pool as light passes through waves on the water surface. The effects described above are all *linear* optical effects. That is to say, the phase distortion experienced by the light field does not depend on the amount of energy contained in the field.

Generally, *nonlinear* optical effects occur in materials whose polarization depends nonlinearly on the field passing through them. This nonlinear polarization acts as a driving term in the Helmholtz equation, generating new optical fields in the material. For example, materials whose polarization depends on the square of the input field can generate new light fields oscillating at twice the input field's frequency (second harmonic generation) or create a DC field inside the material (optical rectification) [3]. Several other nonlinear optical effects are possible, such as difference frequency generation, sum frequency generation, self-focusing, two-beam coupling, and higher harmonic generation, just to name a few. Self-focusing and two-beam coupling are of particular interest to this thesis. Self-focusing is characterized by a third-order dependence on the optical field such that the phase of the field propagating in the material depends upon its own intensity. Or, framed a bit differently, the refractive index of the material depends upon the intensity of the light illuminating it,

$$n = n_0 + n_2 I(\boldsymbol{r}), \tag{1.1}$$

where n_0 is the linear refractive index, n_2 is the nonlinear refractive index, and $I(\boldsymbol{r})$ is the intensity of the beam. Thus, the transverse intensity structure of the beam forms an effective lens in the material. Irregularities in the transverse intensity structure of the beam can cause the beam to breakup into several smaller beams, known as filaments, under nonlinear self-focusing. Filamentation can even be seeded by quantum fluctuations in the beam intensity [4].

Two-beam coupling occurs when the refractive index experienced by one beam is modified by the presence of another beam,

$$n = n_0 + n_2 \left[I_1(\boldsymbol{r}) + \mu I_2(\boldsymbol{r}) \right], \tag{1.2}$$

where $I_1(\boldsymbol{r})$ and $I_2(\boldsymbol{r})$ are the intensities of the two beams and μ is a coupling parameter. The two beams can be distinguished by their frequency, polarization, or direction of propagation, among other degrees of freedom. Thus, the effective lens mentioned earlier can now be controlled by an auxilliary beam. Whether it be through self-focusing or two-beam coupling, a material with an intensity dependent refractive index introduces phase distortions to light passing through it.

Characterizing and mitigating phase distortions, both linear and nonlinear, are crucial for high resolution imaging, optical communications [5], remote atmospheric sensing [6], laser-based lightning strike control [7], and directed energy applications [8]. Quantum imaging is a quickly developing field that harnesses the strong spatial correlation entangled photons to enhance or provide alternatives to classical imaging techniques. In particular, ghost imaging is a scheme that allows one to image an object at wavelengths where detectors are either unavailable or cost-prohibitive. This is accomplished by illuminating the object with a photon from an entangled pair and detecting it in coincidence with its entangled partner photon. However, like classical imaging techniques, aberrations degrade the image obtained from this method. Extending the characterization and compensation of optical aberrations into the quantum domain pushes the boundaries of current adaptive optics techniques.

In Chap. 2, the strong position and momentum correlation of spatially entangled photons are used to demonstrate a *nonlocal* aberration correction scheme. Aberrations introduced into the path of one photon in an entangled pair degrade the amount of position correlations measured between the two photons. In a ghost imaging setup, these aberrations are shown to degrade the imaging resolution. However, by introducing the proper conjugate aberration to the other photon's path, the position correlation of the two photons and the original ghost imaging resolution are recovered. The experiment and results of Chap. 2 extends the field of adaptive optics into the quantum domain.

In some cases the phase distortion introduced to a light field is the primary object of interest. Such is the case in the imaging of phase-only objects, which includes the imaging of live biological samples. Some biological cells, like an alga studied for biofuel production known as chlamydomonas reinhardtii, are sensitive to illumination at certain wavelengths [9, 10]. As a result, it is difficult to image samples like chlamydomonas reinhardtii at a high resolution and high signal-to-noise ratio without changing the state of the cell. In Chap. 3, a quantum-enabled phase imaging method is presented that achieves twice the signal-to-noise ratio and approximately 1.7 times the resolution of classical low-light phase imaging. This quantum phase imaging technique relies upon the quantum interference between cascaded spontaneous parametric down-conversion processes. The strong position correlation between photons created in spontaneous parametric down conversion is used to achieve twice the phase shift of classical quantitative phase imaging. Furthermore, the wide spatial bandwidth of spontaneous parametric down-conversion photons leads to an increase in the imaging resolution compared to illumination with a classical laser beam. These enhancements are obtained without measuring the entangled photons in coincidence. As a result, the data collection requires approximately ten seconds, which is three orders of magnitude faster than state-of-the-art coincidence imaging techniques [11] and closer to the relevant time scales of biological processes.

As mentioned earlier, a nonlinear material with an intensity-dependent refractive index can introduce significant phase distortions to high intensity laser beams. In particular, nonlinear self-focusing can cause caustic features to develop in a beam that wouldn't develop caustics under linear propagation [12]. High intensity laser beams are central to the developing fields of remote atmospheric sensing, laser-enabled lightning strike control, and directed energy defense systems. Mitigating nonlinear phase distortions will be essential in the continuing development of these fields. Laser beams with a transversely varying polarization, sometimes referred to as polarization-structured beams, have been shown to be more stable against effects due to nonlinear self-focusing [13]. In Chap. 4, a particular polarization-structured beam that contains all states of full polarization, known as a full-Poincaré beam, is studied under conditions that lead to the development of nonlinear optical caustics. Compared to a uniformly polarized beam with the same intensity structure, the full Poincaré beam is less likely to develop nonlinear optical caustics for a range of beam powers. Thus, the nonlinear phase distortion is mitigated by imposing polarization structuring on the beam. The results of this chapter may also be useful for fiber-based optical communications, where some polarization-structured beams form the mode basis of certain optical fibers [14].

So far, the study of polarization structured beams under nonlinear propagation has been limited to beams that contain only states of full polarization. However, more complicated polarization-structured beams that contain states of both full and partial polarization may result in a greater resistance to the effects resulting from an intensity-dependent refractive index [15]. Chapter 5 presents a method of generating polarization-structured beams that contain both full and partial polarization. This method is then used to generate a beam that contains all possible states of polarization at some point along the transverse and longitudinal extent of the beam. Because this beam contains all states on the interior and surface of the Poincaré sphere, it is referred to here as a volumetrically-full Poincaré beam. Beams that contain orbital angular momentum are more likely to break up under nonlinear propagation [16, 17]. Though the full-Poincaré beam in Chap. 4 is more stable against nonlinear beam breakup, it contains a nonzero orbital angular momentum. The volumetrically-full Poincaré beam generated in Chap. 5 has the same intensity structure as the full-Poincaré beam, but it contains zero orbital angular momentum. As a result, it may have an increased stability to nonlinear beam breakup beyond that of a full-Poincaré beam.

In applications ranging from high resolution imaging to remote atmospheric sensing, one must contend with phase distortions introduced from either linear or nonlinear effects. The methods presented in this thesis provide new ways to characterize and mitigate phase distortions using the properties of spatially entangled photons and polarization structured beams. The experiments using spatially entangled photons open up new avenues for quantum-enhanced phase imaging and improve existing quantum imaging protocols. It is also shown that polarization-structured beams can be used to improve high intensity laser systems, and a new type of polarization-structured beam involving all possible states of polarization is demonstrated. By reaching into the quickly developing fields of quantum optics and structured-light generation, this thesis provides new alternatives to current methods of handling phase distortions.

2. Quantum Nonlocal Aberration Cancellation

2.1 Introduction

Correlations between entangled particles have been widely studied since Einstein, Podolsky, and Rosen published an argument regarding the incompleteness of quantum mechanics [18]. Through the use of spontaneous parametric down-conversion in birefringent crystals, photons entangled in energy-time [19], position-momentum [20], polarization [21], and angular momentum [22] can be readily produced for experiments. Generally speaking, the optical path through which the entangled photons propagate determines the level of correlation that can be measured in the modulus of the two photon wave function [23]. In the case of energy-time entangled photons, the group velocity dispersion (GVD) of the media through which each photon passes will effect the amount of correlation measured in the time of creation of the two photons. This idea was first explored by J.D. Franson with the result that when the GVD parameters of the media in each photon's path were equal in magnitude, but opposite in sign, the effect of GVD on the temporal correlation between the two photons could be cancelled nonlocally [24]. A local dispersion cancellation scheme relying upon path distinguishability was reported experimentally by Steinberg et al. shortly after Franson's proposal [25].

Group velocity dispersion represents only the second-order term in a frequency-dependent phase shift that can be composed of both even- and odd-order terms of various powers. Non-simultaneous local cancellation of both even- and odd-order terms in this phase shift has been demonstrated [26] and the simultaneous cancellation of higher-order frequency-dependent phase shifts was demonstrated as a quantum encryption method that is analogous to orthogonal optical coding [27]. Despite being proposed thirty year ago, Franson's nonlocal dispersion cancellation scheme was only recently demonstrated experimentally [19]. Classical dispersion cancellation has also been demonstrated since time-frequency correlation can be achieved classically [28, 29].

The Fourier transform relationship between the basis in which the phase shift is introduced and the basis of the correlation measurement allows one to extend the ideas of dispersion cancellation to the position-momentum domain. A transverse momentum-dependent phase shift introduced to a photon's path is equivalent to introducing aberration [30]. Such an aberration will alter the joint probability of detection in the image plane of the crystal where two position-momentum entangled photons are produced, suggesting the possibility of a spatial analogue to Franson's nonlocal dispersion cancellation experiment. No such experiment has been reported at the time of this writing. Furthermore, no experiment has demonstrated the simultaneous cancellation of both even- and odd-order aberrations. Local even-order aberration cancellation has been demonstrated, and revealed through Hong-Ou-Mandel interference [31]. Local odd-order aberration cancellation has also been demonstrated [32]. All-order aberration compensation has also been demonstrated recently, but was still performed locally [33]. The nonlocal compensation of pure phase objects has been reported, but it was only revealed through polarization correlations [34].

This chapter demonstrates the effect of defocus and its subsequent cancellation on transverse entanglement measurements and the first successful nonlocal cancellation of both even- and odd-order aberrations. Further, defocus is cancelled nonlocally in a quantum imaging experiment, demonstrating the utility of nonlocal aberration cancellation in optimizing quantum imaging setups [35–37].

2.2 Background

The two-photon wave function for the entangled photons emitted during spontaneous parametric down conversion (SPDC), known as the signal and idler, has been derived by a number of workers in quantum optics [38–41]. This derivation will be summarized in order to set up the discussion of nonlocal aberration cancellation.

To obtain the two photon wave function for the signal and idler photons, it is necessary to first derive the Hamiltonian that governs the SPDC process. The energy of the electromagnetic field inside the material used to produce SPDC is given by,

$$\mathcal{E} = \frac{1}{2}\int_V d^3r\,\left[\boldsymbol{D}\cdot\boldsymbol{E} + \boldsymbol{H}\cdot\boldsymbol{B}\right], \tag{2.1}$$

where the integration is performed over the volume of the material, V. The displacement field, $\boldsymbol{D}$, is defined in terms of the permittivity of free space, ϵ_0, the dielectric susceptibility tensor, $\overleftrightarrow{\chi}$, and the electric field, $\boldsymbol{E}$: $\boldsymbol{D} = \epsilon_0(1+\overleftrightarrow{\chi})\boldsymbol{E}$. The magnetic induction, $\boldsymbol{H} = \boldsymbol{B}/\mu$, also stores energy, where μ is the permiability of the material, and $\boldsymbol{B}$ is the magnetic field. However, the materials typically used for SPDC are non-magnetic. In such cases, $\boldsymbol{H} = \boldsymbol{B}/\mu_0$, where μ_0 is the permiability of free space. The energy can now be expressed as,

$$\mathcal{E} = \frac{1}{2}\int_V d^3r\left[\epsilon_0\boldsymbol{E}\cdot\boldsymbol{E} + \frac{1}{\mu_0}\boldsymbol{B}\cdot\boldsymbol{B}\right] + \frac{1}{2}\int_V d^3r\left[\epsilon_0\overleftrightarrow{\chi}\boldsymbol{E}\cdot\boldsymbol{E}\right]. \tag{2.2}$$

The first term on the R.H.S. of Eq. (2.2) is the free space energy of the EM field. The second term on the R.H.S. of Eq. (2.2) accounts for the interaction of the field with the material.

Generally, the electric susceptibiliy depends upon the electric field inside the material,

$$\overset{\leftrightarrow}{\chi} = \overset{\leftrightarrow}{\chi}^{(1)} + \overset{\leftrightarrow}{\chi}^{(2)} \boldsymbol{E}_1 + \overset{\leftrightarrow}{\chi}^{(3)} \boldsymbol{E}_1 \boldsymbol{E}_2 + \cdots \tag{2.3}$$

The first term on the R.H.S of Eq. (2.3) accounts for the linear response of the material, whereas the terms involving higher orders of $\boldsymbol{E}$ account for the nonlinear response of the material. Accordingly, the susceptibility can be written as, $\overset{\leftrightarrow}{\chi} = \overset{\leftrightarrow}{\chi}^{(1)} + \overset{\leftrightarrow}{\chi}_{NL}$. Because the process of SPDC involves the interaction of multiple fields, it is only the nonlinear term in the susceptibility that gives rise to SPDC. In particular, SPDC arises from the second order susceptibility, $\overset{\leftrightarrow}{\chi}^{(2)}$. In addition to SPDC, the second-order susceptibility leads to effects such as sum-frequency generation, difference-frequency generation, and optical rectification [42]. However, in SPDC only a single field, known as the pump, is incident on the nonlinear material that generates SPDC. Furthermore, the generated signal and idler fields are very weak and will be assumed to produce a negligible sum-frequency, difference-frequency, or optical rectification field through a cascaded nonlinearity. Thus, the relevant energy associated with the SPDC process is then,

$$\mathcal{E}_{NL} = \frac{1}{2} \int_V d^3r \left[\epsilon_0 \overset{\leftrightarrow}{\chi}^{(2)} \boldsymbol{E}_p \boldsymbol{E}_s \boldsymbol{E}_i \right], \tag{2.4}$$

where p, s, i represent the pump, signal, and idler fields respectively. Equation (2.4) can be simplifed if only type-II phase matching is considered. In this case, the polarizations of the pump and signal photons lie in the plane of the optical axis of the crystal used to generate SPDC. This polarization is known as extraordinary polarization [43]. The idler photon's polarization is orthogonal to the optic axis of the crystal, known as ordinary polarization. The signal and idler fields can be cast as operators to switch to the quantum mechanical picture. The pump field will remain classical under the assumption that it is minimally depleted during the SPDC process. Thus, the effective Hamiltonian for the interaction of a pump field with a nonlinear crystal producing a two-photon state under nearly collinear type-II phase matching is given by,

$$\hat{\mathcal{H}} = \epsilon_0 \int_V d^3r \chi^{(2)}_{eeo} E^{(+)}_{p,e} \hat{E}^{(-)}_{s,e} \hat{E}^{(-)}_{i,o} \tag{2.5}$$

where $\chi^{(2)}$ is the second order nonlinear susceptibility. $E^{(+)}_{p,e}$ is the positive frequency, extraordinarily polarized, classical electric field of the pump given by,

$$E^{(+)}_{p,e} = \int d^3k_p A(\boldsymbol{k}_p) exp[i(\boldsymbol{k}_p \cdot \boldsymbol{r} - \omega_p(k_p)t)] \tag{2.6}$$

The bounds of integration in Eq. (2.6) are suppressed and range from $-\infty$ to ∞. $\hat{E}^{(-)}_{j,\sigma}$ is the negative frequency component of the electric field operator for the signal or idler photon ($j = s, i$; $\sigma = e, o$):

$$\hat{E}^{(-)}_{j,\sigma} = \int d^3k_j \epsilon_\sigma(\omega_j) \hat{a}^\dagger(\boldsymbol{k}_j, \sigma) exp[-i(\boldsymbol{k}_j \cdot \boldsymbol{r} - \omega_j(k_j)t)] \tag{2.7}$$

where

$$\epsilon_\sigma(\omega_j) = \frac{i}{(2\pi)^3} \sqrt{\frac{\hbar\omega_j(k_j)V_Q}{2\epsilon_0 n^2_\sigma(\omega_j)}} \tag{2.8}$$

The quantization volume is represented as V_Q and $\boldsymbol{k}_j = \kappa_j \hat{\rho}_j + k_{j,z}\hat{z}_j$ ($j = s, i$). The transverse wavevector is connected to the transverse momentum through the de Broglie relation, $\boldsymbol{p}_\perp = \hbar\boldsymbol{\kappa}$. The state of the field after the crystal is obtained by acting upon the vacuum with the time translation operator approximated to the first order.

$$|\psi(t)\rangle = \hat{U}(t)|0\rangle = \left(1 - \frac{i}{\hbar}\int_0^t d\tau \hat{\mathcal{H}}(\tau)\right)|0\rangle \tag{2.9}$$

Evaluating the right-hand-side (RHS) of Eq. 2.9 results in a rather lengthy expression:

$$\begin{aligned}|\psi(t)\rangle = \frac{-i\epsilon_0\chi^{(2)}_{eeo}}{2\hbar}\int d\tau \int_V d^3r \int d^3k_p \int d^3k_s \int d^3k_i \epsilon_e(\omega_s)\epsilon_o(\omega_i) \\ \times A(\boldsymbol{k}_p)\exp\left[i(\boldsymbol{k}_p-\boldsymbol{k}_i-\boldsymbol{k}_s)\cdot\boldsymbol{r}-i(\omega_p-\omega_s-\omega_i)\tau\right] \\ \times |\omega_s,\boldsymbol{k}_s,e\rangle|\omega_i,\boldsymbol{k}_i,o\rangle,\end{aligned} \tag{2.10}$$

where the vacuum contribution to the state has been dropped (though it will be important in Chap. 3). After evaluating the time and volume integrals, Eq. (2.10) becomes

$$\begin{aligned}|\psi(t)\rangle = \frac{-i\epsilon_0\chi^{(2)}_{eeo}}{2\hbar}\int d^3k_p \int d^3k_s \int d^3k_i \epsilon_e(\omega_s)\epsilon_o(\omega_i)A(\boldsymbol{k}_p) \\ \times \exp\left[i(\omega_s+\omega_i-\omega_p)\frac{t}{2}\right]\operatorname{sinc}\left[(\omega_s+\omega_i-\omega_p)\frac{t}{2}\right] \\ \times \prod_m \exp\left[-i(\boldsymbol{k}_s+\boldsymbol{k}_i-\boldsymbol{k}_p)_m\frac{\ell_m}{2}\right]\operatorname{sinc}\left[(\boldsymbol{k}_s+\boldsymbol{k}_i-\boldsymbol{k}_p)_m\frac{\ell_m}{2}\right] \\ \times |\omega_s,\boldsymbol{k}_s,e\rangle|\omega_i,\boldsymbol{k}_i,o\rangle,\end{aligned} \tag{2.11}$$

where $m = \{x, y, z\}$, and ℓ_m is the length of the crystal along a particular dimension.

A few approximations can be made to simplify the (RHS) Eq. (2.11) [39]. The first approximation is that the transverse dimensions of the crystal are large compared to the transverse size of the pump beam. Put another way, the pump, signal, and idler effectively don't "see" the edges of the crystal. This approximation leads to

$$\operatorname{sinc}\left[(\boldsymbol{k}_s+\boldsymbol{k}_i-\boldsymbol{k}_p)_x\frac{\ell_x}{2}\right]\operatorname{sinc}\left[(\boldsymbol{k}_s+\boldsymbol{k}_i-\boldsymbol{k}_p)_y\frac{\ell_y}{2}\right] \approx \delta(\boldsymbol{\kappa}_s+\boldsymbol{\kappa}_i-\boldsymbol{\kappa}_p) \tag{2.12}$$

Next, the paraxial approximation is employed, and the crystal is taken to be thin enough to ignore transverse walk-off of the beam [39] such that,

$$k_{z,j} \approx k_j\left(1-\frac{\kappa_j^2}{2k_j^2}\right) \qquad j = \{i, s, p\} \tag{2.13}$$

Similarly, is it assumed that $dk_{z,j} \approx dk_j$. The pump is assumed to be approximately monochromatic, resulting in $A(\boldsymbol{k}_p) = v(\boldsymbol{\kappa}_p)\delta(k_p - k_0)$, where $v(\boldsymbol{\kappa}_p)$ is the angular spectrum of the pump. Finally, perfect phase matching is assumed, $k_s + k_i - k_p = 0$. With these approximations, the two photon wave function becomes

$$\begin{aligned}|\psi(t)\rangle = \frac{-i\epsilon_0\chi^{(2)}_{eeo}}{2\hbar}&\int dk_s\int dk_i\int d^2\kappa_i\int d^2\kappa_s\epsilon_e(\omega_s)\epsilon_o(\omega_i)v(\boldsymbol{\kappa}_s+\boldsymbol{\kappa}_i)\\
&\times\exp\left[-i\left(\frac{|\boldsymbol{\kappa}_s+\boldsymbol{\kappa}_i|^2}{2k_0}-\frac{|\boldsymbol{\kappa}_s|^2}{2k_s}-\frac{|\boldsymbol{\kappa}_i|^2}{2k_i}\right)\frac{\ell_c}{2}\right]\\
&\times\operatorname{sinc}\left[\left(\frac{|\boldsymbol{\kappa}_s+\boldsymbol{\kappa}_i|^2}{2k_0}-\frac{|\boldsymbol{\kappa}_s|^2}{2k_s}-\frac{|\boldsymbol{\kappa}_i|^2}{2k_i}\right)\frac{\ell_c}{2}\right]\\
&\times\exp\left[-i(\omega_s+\omega_i-\omega_0)\frac{t}{2}\right]\operatorname{sinc}\left[(\omega_s+\omega_i-\omega_0)\frac{t}{2}\right]\\
&\times|\omega_s,\boldsymbol{\kappa}_s,e\rangle|\omega_i,\boldsymbol{\kappa}_i,o\rangle\end{aligned}\tag{2.14}$$

where the substitution $\ell_z = \ell_c$ has been made for the length of the crystal along the propagation direction.

After creation, the signal and idler photons are split by a polarizing beamsplitter, passed through an optical system that adds a transverse momentum-dependent phase shift (aberration), and are detected in either the position basis or the momentum basis. The amplitude for coincident detection in the position basis can be evaluated as follows [38]:

$$A(\boldsymbol{\rho}_s,\boldsymbol{\rho}_i) = \langle 0|\hat{E}^{(+)}_{s,e}(\boldsymbol{\rho}_s)\hat{E}^{(+)}_{i,o}(\boldsymbol{\rho}_i)|\psi(t)\rangle \tag{2.15}$$

where,

$$\begin{aligned}\hat{E}^{(+)}_{j,\sigma} = \int d^2\kappa'_j\epsilon_\sigma\left(\frac{\omega_p}{2}\right)H_j(\boldsymbol{\kappa}'_j)\hat{a}\left(\boldsymbol{\kappa}'_j,\sigma,\frac{\omega_0}{2}\right)\\
\times\exp\left[i\left(\boldsymbol{\kappa}'_j\cdot\boldsymbol{\rho}_j-\frac{\omega_0}{2}T\right)\right]\end{aligned}\tag{2.16}$$

Note that it has been explicitly required that the photons be detected at time T and at a frequency $\frac{\omega_0}{2}$. In practice, the frequency of the signal and idler photons are well-defined by narrow-band interference filters. $H(\boldsymbol{\kappa}'_j)$ represents the transfer function of the optical system containing the aberration and is given by,

$$H_j(\boldsymbol{\kappa}'_j) = exp\left[i\phi_j(\boldsymbol{\kappa}'_j)\right] \tag{2.17}$$

The coincident detection amplitude is given approximately by,

$$\begin{aligned} A(\boldsymbol{\rho}_s, \boldsymbol{\rho}_i) = C \int d^2\kappa_s \int d^2\kappa_i \, \nu(\boldsymbol{\kappa}_s + \boldsymbol{\kappa}_i) \, \mathrm{sinc}\left[\frac{\ell_c|\boldsymbol{\kappa}_s - \boldsymbol{\kappa}_i|^2}{4k_0}\right] \\ \times \exp\left[-i\left(\frac{\ell_c|\boldsymbol{\kappa}_s - \boldsymbol{\kappa}_i|^2}{4k_0}\right)\right] H_s(\boldsymbol{\kappa}_s) H_i(\boldsymbol{\kappa}_i) \\ \times \exp[i(\boldsymbol{\kappa}_s \cdot \boldsymbol{\rho}_s + \boldsymbol{\kappa}_i \cdot \boldsymbol{\rho}_i)] \end{aligned} \tag{2.18}$$

where all factors not depending upon the transverse wavenumber have been subsumed by C. The integrand in Eq. (2.18) sans the kernel is the wave function for the photons in transverse wavenumber space. Writing it in a more compact form,

$$\psi\left(\boldsymbol{\kappa}_s, \boldsymbol{\kappa}_i\right) = C\nu\left(\boldsymbol{\kappa}_s + \boldsymbol{\kappa}\right)\tilde{\chi}^{(2)}(\boldsymbol{\kappa}_s - \boldsymbol{\kappa}_i) H_s(\boldsymbol{\kappa}_s) H_i(\boldsymbol{\kappa}_i) \tag{2.19}$$

Because $\tilde{\chi}^{(2)}$ is effectively the Fourier transform of the nonlinear susceptibility along the propagation direction, it is typically referred to as the phase-matching function.

2.2.1 Nonlocal Aberration Cancellation

One can see from the functional dependence on $\boldsymbol{\kappa}_s$ and $\boldsymbol{\kappa}_i$ that the wave function is nonseparable in this basis. The term $\nu(\boldsymbol{\kappa}_s + \boldsymbol{\kappa}_i)$ depends upon the transverse momentum coherence properties of the pump and will influence the transverse momentum anticorrelation of the signal and idler photons [44, 45]. In the case that the pump is a plane wave, the transverse momentum anticorrelation of the signal and idler will be perfect. In most cases the pump profile is a Gaussian, resulting in less momentum anticorrelation between the signal and idler than for a plane-wave pump. The remaining terms in the momentum-basis wave function,

$$\exp\left[-i\left(\frac{\ell_c|\boldsymbol{\kappa}_s-\boldsymbol{\kappa}_i|^2}{4k_0}\right)\right]\operatorname{sinc}\left[\frac{\ell_c|\boldsymbol{\kappa}_s-\boldsymbol{\kappa}_i|^2}{4k_0}\right]H_s(\boldsymbol{\kappa}_s)H_i(\boldsymbol{\kappa}_i) \tag{2.20}$$

will also influence the transverse position and momentum correlations of the signal and idler photons. In particular, the transverse momentum-dependent phase shift introduced to each beam will influence the form of the coincidence distribution in the position basis. To explore this effect, the momentum-dependent phase shift introduced to each photon can be expanded in a Taylor series. For the sake of simplicity, the phase shift will be introduced in one dimension only.

$$\phi_j(\kappa_{j,x})=\phi_{j,0}+\phi_j'(0)\,\kappa_{j,x}+\phi_j''(0)\,\kappa_{j,x}^2/2+\cdots \tag{2.21}$$

where $j=s,\ i$. The pump is taken to be a plane wave, leading to $v(\boldsymbol{\kappa}_s+\boldsymbol{\kappa}_i)=\delta(\boldsymbol{\kappa}_s+\boldsymbol{\kappa}_i)$. In order to simplify the integration of Eq. (2.18), the sinc function can be approximated by a Gaussian [23],

$$\operatorname{sinc}\left[\frac{\ell_c\ |\boldsymbol{\kappa}_s-\boldsymbol{\kappa}_i|^2}{4k_0}\right]\approx\exp\left[-\frac{\gamma\ell_c\ |\boldsymbol{\kappa}_s-\boldsymbol{\kappa}_i|^2}{4k_0}\right] \tag{2.22}$$

where $\gamma=0.455$. The amplitude for coincident detection becomes,

$$\begin{aligned}A(\boldsymbol{\rho}_s,\boldsymbol{\rho}_i)\approx A_1(y_s,y_i)&\int d\kappa_x\ \exp\left[-if(\kappa_x)\right]\\&\times\exp\left[-\frac{\gamma\ell_c\kappa_x^2}{k_0}\right]\exp[i(\kappa_x[x_s-x_i])],\end{aligned} \tag{2.23}$$

where

$$f(\kappa_x) = \frac{\ell_c \kappa_x^2}{k_0} - (\Phi_0 + \kappa_x(\alpha_s - \alpha_i) + \kappa_x^2(\beta_s + \beta_i) + \cdots). \tag{2.24}$$

In arriving at Eqs. (2.23) and (2.24), the plane wave pump approximation led to the substitution $\boldsymbol{\kappa}_i = -\boldsymbol{\kappa}_s = -\boldsymbol{\kappa}$. The coefficients of the expansion (2.21) have been subsumed by α_j and β_j, and $\Phi_0 = \phi_{s,0} + \phi_{i,0}$. One can already see in Eq. (2.24) that under certain circumstances the effect of the momentum-dependent phase shift introduced to one photon can be cancelled by the momentum-dependent phase shift introduced to the other in the two-photon wave function. In particular, if all of the even terms in the expansion (2.21) are equal in magnitude but opposite in sign for the two photons and all the odds terms are equal, the two phase shifts will cancel. This leads to the condition

$$\phi_s(\kappa_x) = -\phi_i(-\kappa_x) \tag{2.25}$$

for full cancellation to occur. This functional dependence is result of the momentum *anti-correlation* of the signal and idler. If the aberrations occurred in the plane where positions of the signal and idler photons were positively correlated (such as the output facet of the nonlinear crystal), the condition for all-order aberration cancellation would instead be $\phi_s(x) = -\phi_i(x)$.

If only the terms through second order are kept in Eq. (2.21) and the integration is carried out in Eq. (2.23) the result is,

$$A(\boldsymbol{\rho}_s, \boldsymbol{\rho}_i) \propto \exp\left[-\frac{(x_- + \alpha_-)^2}{2\left(\frac{\gamma\,\ell_c}{k_0} + i\left(\frac{\ell_c}{k_0} - \beta_s - \beta_i\right)\right)}\right]. \tag{2.26}$$

where $x_- = (x_s - x_i)/\sqrt{2}$. The terms involving the y-direction and a constant of integration have been dropped in Eq. (2.26). The probability for coincident detection is then,

$$P(\boldsymbol{\rho}_s, \boldsymbol{\rho}_i) \propto \exp\left[\frac{-\frac{2\gamma\,\ell_c}{k_0}\,(x_- + \alpha_-)^2}{\left(\frac{(\gamma\,\ell_c)^2}{k_0^2} + \left(\frac{\ell_c}{k_0} - \beta_s - \beta_i\right)^2\right)}\right] \tag{2.27}$$

From Eq. (2.27) is it clear that the width of the coincidence distribution in the x_--direction is influenced by the sum $\beta_s + \beta_i$. Intuitively, this is expected because the Fourier transform of a Gaussian is a Gaussian. The location of the coincidence distribution's mean in the x_-- direction is influenced by $\alpha_- = (\alpha_s - \alpha_i)/\sqrt{2}$. This can be understood intuitively by noting that a linear phase results in a displacement in the Fourier space according to the Fourier shift theorem [46]. If the transverse momentum dependent phase shifts satisfy the criteria in Eq. (2.25), then the effects of these shifts on the coincidence distribution will be cancelled nonlocally. This cancellation is the spatial analogue of Franson's nonlocal dispersion cancellation [24]. Because the aberration is a phase in the momentum-basis, it does not affect the form of the probably distribution in this domain. One can generalize the findings above to include higher-order terms in the expansion of the momentum-dependent phase shift. For example, if a cubic momentum-dependent phase is introduced to the signal and idler without cancellation, the skew of the joint position distribution will change.

It should be noted that aberration cancellation relies solely upon transverse momentum correlation between the signal and idler. Because momentum correlation between two beams can be achieved classically [47, 48], this effect may be possible in the classical regime.

2.2.2 Common Optical Aberrations

The terms in expansion of the momentum-depdendent phase, Eq. (2.21), are useful for demonstrating nonlocal aberration canellation but lack a clear connection between common

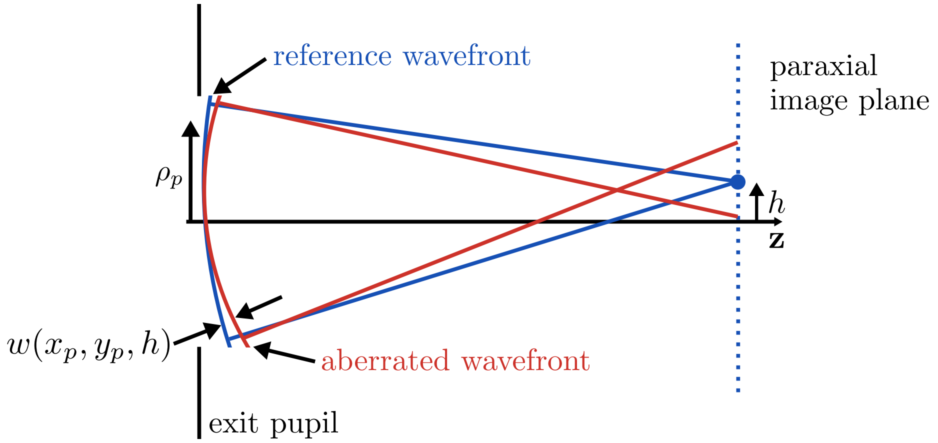

Figure 2.1: Diagram depicting the wavefront expansion method of classifying optical aberrations, adapted from [49]. The reference wavefront (blue) propagates to a point on the paraxial image plane from the exit pupil of an optical system. Aberrations (undefined in this example) cause the aberrated wavefront (red) to focus at a location other than the paraxial image plane. The wavefront error, $w(x_p, y_p, h)$, is defined in terms of the pupil coordinates x_p and y_p and the normalized image height, h.

optical aberrations used in optical engineering and adaptive optics. Figure 2.1 diagrams the wavefront expansion method of classifying optical aberrations [49]. An ideal imaging system will cause a wavefront at the exit pupil of an imaging system to focus to a point on the paraxial image plane (blue). This wavefront, the reference wavefront, will be compared with the wavefront at the exit pupil of an imaging system that contains aberrations (red). The difference in the reference wavefront and the aberration wavefront is known as the wavefront error, $w(x_p, y_p, h)$, and is defined in terms of the exit pupil coordinate, x_p and y_p, and the normalized image height, h. By convention, the exit pupil coordinates in the polar basis are defined as $x_p = \rho_p \sin(\theta_p)$ and $y_p = \rho_p \cos(\theta_p)$, where θ_p is angle in the clockwise direction from the y_p axis. By definition, the exit pupil is assumed to be the location of the Fraunhoffer diffraction pattern formed by the object to be imaged and the imaging system. Thus, the coordinates of the exit pupil plane are directly proportional to the transverse momentum coordinates, $x_p \propto \kappa_x$ and $y_p \propto \kappa_y$. As such, any deviations from an ideal phase (i.e. spherical reference wavefront) in this plane correspond to a momentum-dependent phase shift.

For rotationally symmetric systems, the wavefront error is expanded in terms of h^2, ρ_p^2, and $h\rho_p \cos(\theta_p)$,

$$w(\rho_p, \theta_p, h) = \sum_i \sum_j \sum_k W_{2i+k,2j+k,k} \left(h^2\right)^i \left(\rho_p^2\right)^j \left[h\rho_p \cos(\theta_p)\right]^k . \tag{2.28}$$

The coefficient W and its subscripts are a shorthand way of referring to a particular type of aberration. The subscripts on the coefficient W are chosen to make them consistent with the convention used on Ref. [49]. Table 2.1 shows terms in the wavefront expansion of order five and below, their common name, and their W coefficient. By convention, the order is assigned based upon the order of the ray aberration–one less than the order of the wavefront aberration.

The dependence of the terms in the wavefront expansion on the image height, h, makes a straightforward connection between the terms in momentum-dependent phase, Eq. (2.21), and the terms in Eq. (2.28) difficult. However, if the wavefront is measured for the maximum image point, $h = 1$, the connection is more clear. Furthermore, when h is set equal to one, the terms in the wavefront expansion can be described using the Zernike polynomials [50]. The Zernike polynomials are an orthogonal basis set of polynomials defined on a unit disk that satisfy the requirement of rotational symmetry common to most optical systems. Their mathematical form is that of a product solution [51],

$$Z_n^m \left(\rho_p, \theta_p\right) = R_n^m \left(\rho_p\right) \exp\left(im\theta_p\right) \tag{2.29}$$

The radial function, R_n^m, is a real polynomial in ρ_p. Typically, the real part of Z_n^m is chosen if the angular symmetry of the optical system is relative to the y-axis. However, the imaginary part of Z_n^m may be chosen if the symmetry is relative to the x-axis. Because the Zernike

Table 2.1: Common optical aberrations.

aberration	coefficient	functional form
piston	W_{000}	1
defocus	W_{020}	ρ_p^2
wavefront tilt	W_{111}	$h\rho_p \cos\left(\theta_p\right)$
spherical aberration (SA)	W_{040}	ρ_p^4
coma	W_{131}	$h\rho_p^3 \cos\left(\theta_p\right)$
astigmatism	W_{222}	$h^2\rho_p^2 \cos^2\left(\theta_p\right)$
field curvature	W_{220}	$h^2\rho_p^2$
distortion	W_{311}	$h^3\rho_p \cos\left(\theta_p\right)$
fifth-order SA	W_{060}	ρ_p^6
fifth-order linear coma	W_{151}	$h\rho_p^5 \cos\left(\theta_p\right)$
fifth-order astigmatism	W_{422}	$h^4\rho_p^2 \cos^2\left(\theta_p\right)$
fifth-order field curvature	W_{420}	$h^4\rho_p^2$
fifth-order distortion	W_{511}	$h^5\rho_p \cos\left(\theta_p\right)$
sagittal oblique SA	W_{240}	$h^2\rho_p^4$
tangential oblique SA	W_{242}	$h^2\rho_p^4 \cos^2\left(\theta_p\right)$
cubic coma	W_{331}	$h^3\rho_p^3 \cos\left(\theta_p\right)$
line coma	W_{333}	$h^3\rho_p^3 \cos^3\left(\theta_p\right)$

Table 2.2: Zernike polynomials, $n, m <= 3$

aberration	n	m	Z_n^m
piston	0	0	1
y tilt	1	1	$\rho_p \cos\left(\theta_p\right)$
defocus and piston	2	0	$2\rho_p^2 - 1$
astigmatism and defocus	2	2	$\rho_p^2 \cos\left(2\theta_p\right)$
coma and y tilt	3	1	$\left(3\rho_p^2 - 2\rho_p\right) \cos\left(\theta_p\right)$

polynomials do not depend upon the image coordinates, their use to characterize aberrations can lead to errors, such as mistaking field curvature for defocus [52]. The first several Zernike polynomials and their resulting aberrations are shown in Table 2.2 [52]. Recall that the exit pupil coordinates are proportional to the transverse wave-vector, $\boldsymbol{\rho}_p \propto \boldsymbol{\kappa}$. Thus, comparing the expansion of the momentum-dependent phase shift, Eq. (2.21), and the Zernike polynomials in Table 2.2, it is clear that the first-order term in the momentum-dependent phase shift is most closely related to wavefront tilt. The second-order term in Eq. (2.21) is related to defocus and the third-order term is related to coma. Higher-order terms follow a similar relationship.

2.2.3 Transverse Entanglement

A well-known signature of transverse entanglement is the violation of the Heisenberg-type inequality [20, 45, 53],

$$\Delta x_-^2 \Delta p_{x,+}^2 \geq \frac{\hbar^2}{4}. \tag{2.30}$$

Because it is possible to increase the width of the joint probability distribution in the image plane along the the x_--direction without affecting the widths of the distribution in the Fourier plane, one can arrive at a scenario where no entanglement is observed due to defocus being

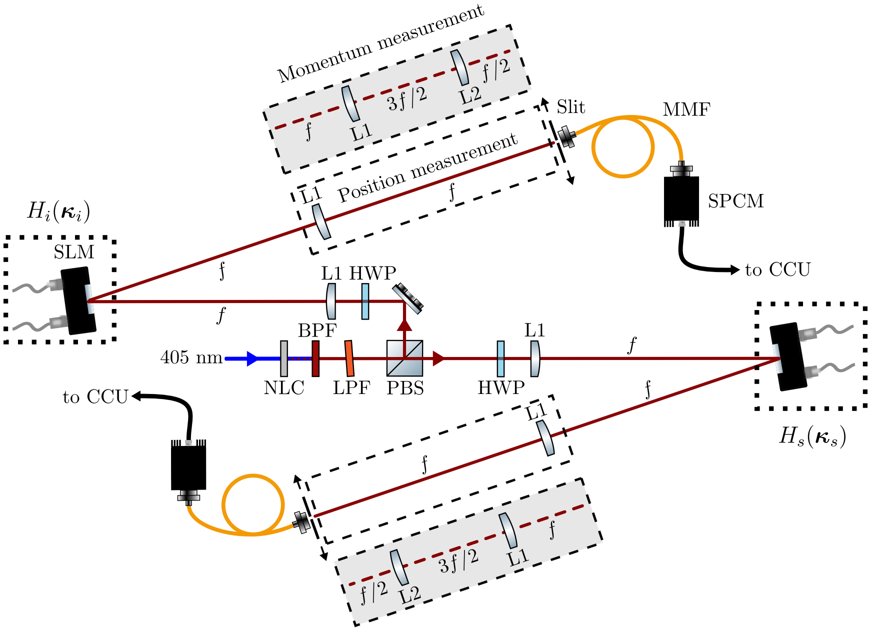

Figure 2.2: Experimental setup for measuring the position and momentum correlation between signal and idler photons. The signal and idler photons are split by a polarizing beamsplitter (PBS) and pass through a $4f$ imaging system for the position measurement. Spatially-resolved detection is achieved using translatable slits. Spatial light modulators (SLM) located in the Fourier plane of the crystal introduce aberrations to each path. For the momentum measurement, the SLMs are imaged onto the plane of the slits. The lenses L1 and L2 have focal lengths $f = 40\,\text{cm}$ and $f/2$ respectively. (BPF–band-pass filter; CCU–coincidence counting unit; HWP–half-wave plate; LPF–low-pass filter; MMF–multimode fiber; SPCM–single-photon counting module

introduced without cancellation in the signal or idler paths. After the nonlocal cancellation of defocus, one can arrive back to a scenario where transverse entanglement is observed. It must be emphasized that the inseparability of the state does not change upon the introduction of aberrations since they are a unitary operation. For this reason, the effect described above is a form of entanglement migration [23, 54].

2.3 Experiment

Correlation measurements were performed in the position and momentum bases to study the effects of introducing aberration to the signal and idler beams separately. Both quadratic and cubic aberrations were introduced into each path with and without cancellation. When only quadratic aberration was introduced, and the level of transverse entanglement was evaluated using the Mancini criterion [Eq. (2.30)]. The setup for this transverse entanglement measurement is shown in Fig. 2.2.

To create spatially entangled photons, a beta barium borate (BBO) crystal was pumped by an ~ 19 mW Gaussian beam of diameter ~ 1 mm centered at 405 nm under type-II phase-matching. The output of the pump laser (Roithner LaserTechnik RLDE405M-100-5) was filtered by a single-mode fiber to achieve a Gaussian profile. The output signal and idler photons were nearly collinear with the pump beam and spectrally filtered with a narrow-band (~ 10 nm) interference filter centered at 810 nm followed by a long-pass filter with a cutoff wavelength at 594 nm. Transverse momentum-dependent phase shifts were implemented using spatial light modulators (SLM, Hamamatsu X10468 − 02) in the signal and idler paths using a reflective geometry. The SLM pixels were 20 μm x 20 μm. The transverse momenta of the signal and idler photons are accessible in the Fourier plane of the BBO crystal. Placing a lens of focal length f a distance f away from the output facet of the BBO crystal maps the transverse wave vectors of the signal and idler photons to transverse position in a plane a distace f behind the lens. This mapping is described by the following relationship: $\boldsymbol{\eta}_{s,i} = f\boldsymbol{\kappa}_{s,i}/k_{s,i}$, where $\boldsymbol{\eta}_{s,i}$ is the transverse position in a plane a distance f behind the Fourier transforming lens.

2.3.1 Calibration of Spatial Light Modulators

Before using the SLMs, it is necessary to calibrate them so that the desired phase shift is achieved. The computer that controls the SLMs treats them as a black-and-white external monitor that displays an 8-bit grayscale value. The exact correspondence between a particular grayscale value and the phase shift imparted by the SLM is dependent upon the angle of

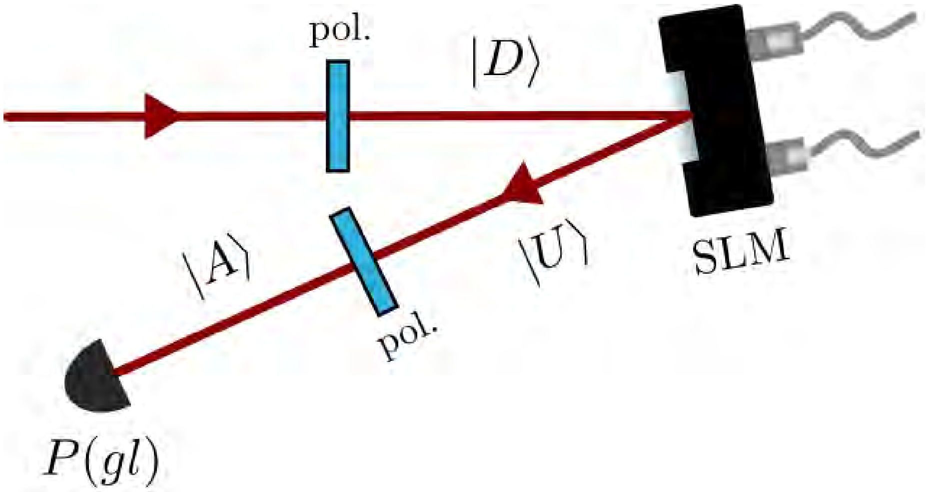

Figure 2.3: Spatial light modulator calibration procedure. A polarizer (pol.) sets the polarization of the light interacting with the SLM to diagonal ($|D\rangle$). The spatial light modulator changes the polarization of the light to a state $|U\rangle$ that depends upon phase shift imparted by the SLM. A final polarizer projects the state onto the anti-diagonal polarization basis $|A\rangle$. Finally, the power (P) is measured.

incidence and wavelength of the light interacting with the SLM. For this reason, the SLMs needed to be calibrated with each new alignment of the optical setup in Fig. 2.2. This process is described in Fig. 2.3. The input polarization is set to diagonal by a polarizer (pol.). The SLM is a birefringent device that only operates on the horizontal polarization component of the input beam. Furthermore, in the absence of any phase shift imparted by the SLM, the reflection from the SLM's surface causes the input diagonally polarized light to be transformed to anti-diagonally polarization. Thus, the polarization state of the beam after reflecting from the SLM is,

$$|U\rangle = \frac{1}{\sqrt{2}}\left(\mathrm{e}^{i\phi(g)}|H\rangle - |V\rangle\right), \tag{2.31}$$

where the phase shift imparted by the SLM, $\phi(g)$, depends on the graylevel, g, programmed on the SLM. Each pixel of the SLM is programmed with the same graylevel in this procedure. A polarizer placed after the SLM projects the polarization state of the beam onto the anti-diagonal basis,

$$\langle A|U\rangle = \frac{1}{2}\left(\mathrm{e}^{i\phi(g)} + 1\right). \tag{2.32}$$

The power measured after the second polarizer is then dependent upon the graylevel displayed on the SLM,

$$P(g) = \cos^2\left(\frac{\phi(g)}{2}\right). \tag{2.33}$$

This expression can then be rearranged to express the phase as a function of the graylevel,

$$\phi(g) = \cos^{-1}\left[2P(g) - 1\right] \tag{2.34}$$

This calibration can be performed pixel-by-pixel if the pixels of the SLM are appropriately imaged onto the pixels of a camera. However, the pixels in the Hamamatsu X10468 − 02 are sufficiently consistent to justify the simple calibration procedure in Fig. 2.3. An example of one such calibration is shown in Fig. 2.4.

To measure coincidences as a function of position in the signal and idler paths, slits of width 100 μm were used to select a small portion of the beam and were moved with servo-controlled micrometer stages in steps of 100 μm. The photons passing through the slits were collected by microscope objectives and coupled into a multimode fiber (MMF) to be detected by single photon counting modules (SPCM). For each setting of the two slits, the coincidence detection rate was recorded using a home-built coincidence-counting unit [55] with a coincidence window of ~ 13 ns. The entire data collection process was automated using a LabVIEW script. From this data the joint probability of detection as a function of the transverse position in the signal and idler beams along one dimension was constructed.

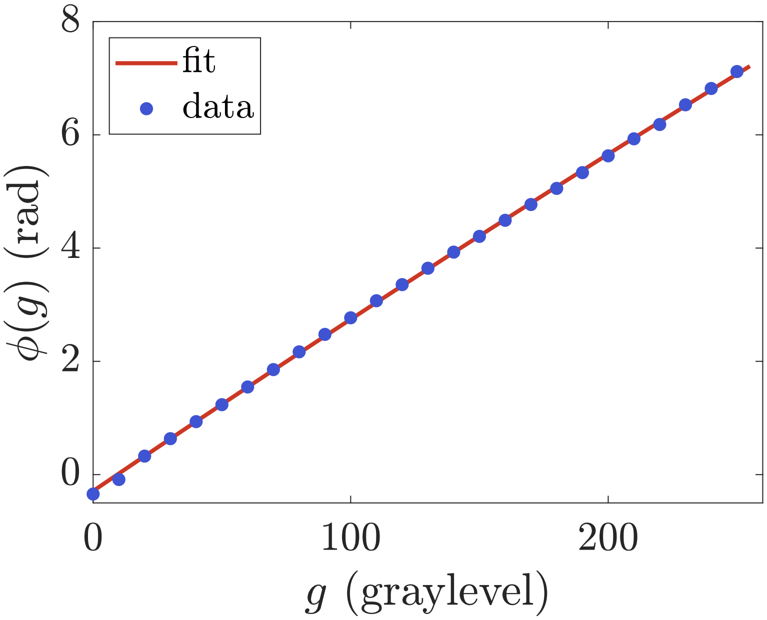

Figure 2.4: Results of the calibration procedure described in Fig. 2.3. A second order polynomial of the form $\phi(g) = ag^2 + bg + c$ is fit to the data using a least squares method. The values of the fitting parameters a, b, and c are $-5.8(7) * 10^{-6}$, $0.0308(2)$, and $-0.29(1)$, respectively. Uncertainties in each data point are too small to visualize on the scale used for $\phi(g)$.

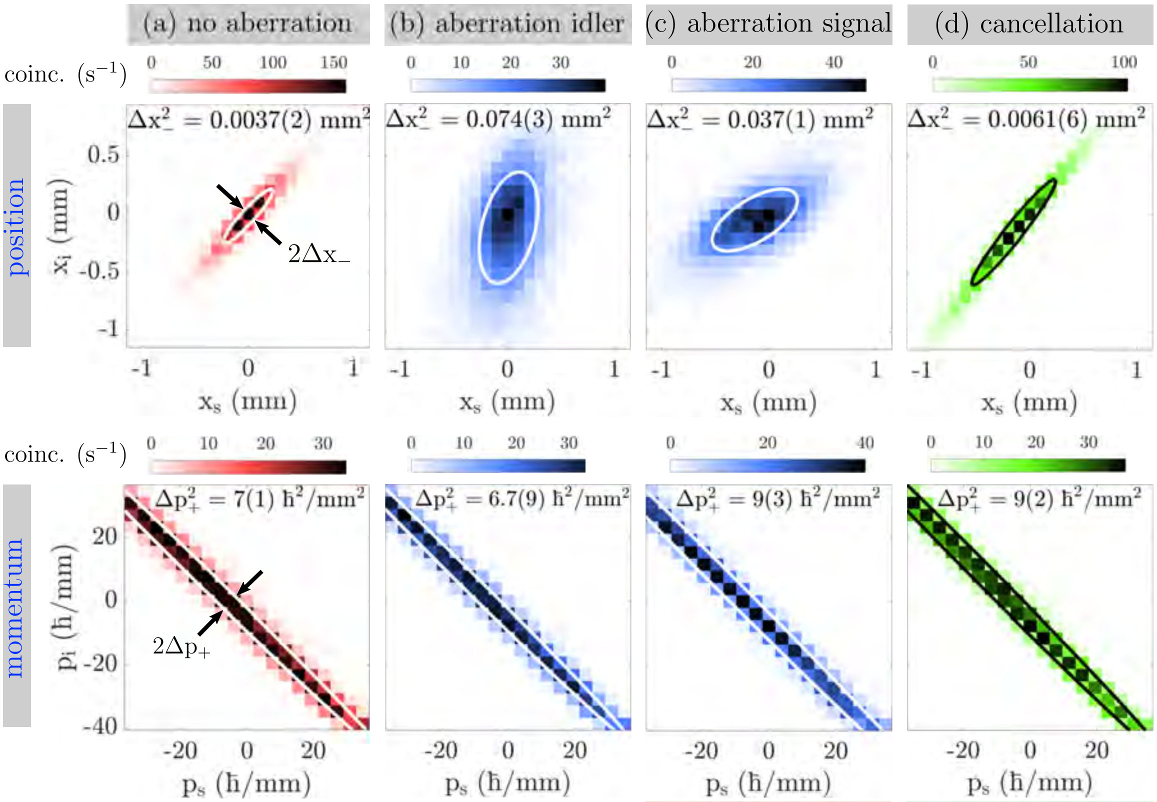

$\phi''_s(0)$	0	0	0.0104 mm^2	0.0104 mm^2
$\phi''_i(0)$	0	-0.0104 mm^2	0	-0.0104 mm^2
$\Delta x_-^2 \Delta p_+^2$	0.026(4) $\hbar^2$	0.50(7) $\hbar^2$	0.3(1) $\hbar^2$	0.05(1) $\hbar^2$

Figure 2.5: The position- and momentum-basis coincidence distributions in the presence of signal and idler defocus. In (a) the state is shown (bottom) to violate Eq. (2.30), a signature of transverse entanglement, without any aberration introduced. (b) and (c) display the broadening of the position-basis coincidence distribution and the subsequent lack of measured entanglement in the presence of defocus. When defocus is introduced to the idler path that is equal in magnitude but opposite in sign to that of the signal path (d), the position-basis coincidence distribution narrows nearly back to its value without aberrations and Eq. (2.30) is again violated. The white (a,b,c) and black (d) lines indicate the 1-σ levels obtained from fitting.

2.4 Results

Data were collected for no aberrations introduced [Fig. 2.5(a)], with only quadratic aberrations introduced [Figs. 2.5(b-d)], and with quadratic and cubic aberrations introduced under conditions of no cancellation [Fig. 2.6(a)], partial cancellation [Fig. 2.6(b)], and full cancellation [Fig. 2.6(c)]. For the case when only quadratic aberrations were introduced to the signal and idler beams (defocus), transverse entanglement was measured according to Eq. (2.30).

To obtain the widths of the coincidence distribution in the + and − directions, maximum likelihood fitting was performed using the model of a bivariate Gaussian distribution,

$$P(y_+, y_-) = \frac{a}{2\pi bc\sqrt{1-d^2}} \exp\left[-\frac{z(y_+, y_-)}{2(1-d^2)}\right], \tag{2.35}$$

where,

$$z(y_+, y_-) = \frac{(y_+ - e)^2}{b^2} - \frac{2d(y_+ - e)(y_- - f)}{bc} + \frac{(y_- - f)^2}{c^2}. \tag{2.36}$$

The variable $y_\pm$ is a stand-in for $x_\pm$ or $\kappa_{x,\pm}$, depending on whether the fitting was performed in the position or momentum basis. The fitting parameters in Eqs. (2.35) and (2.36) are a, b, c, d, e, and f, and the widths along the + and − directions are b and c, respectively. The parameter d describes the correlation in the + and - directions, and the mean of the distribution in the + and - directions are e and f, respectively. The distribution is scaled by the parameter a. In the maximum likelihood estimation routine, the coincidence data were assumed to follow Poisson statistics [56]. The errors on the fitting parameters were obtained through a Monte Carlo simulation.

The results of the entanglement measurement are shown in Fig. 2.5. Without defocus introduced (a), the two-photon state violates Eq. (2.30), as shown at the bottom of Fig. 2.5. This indicates the presence of transverse entanglement. When defocus is introduced to either

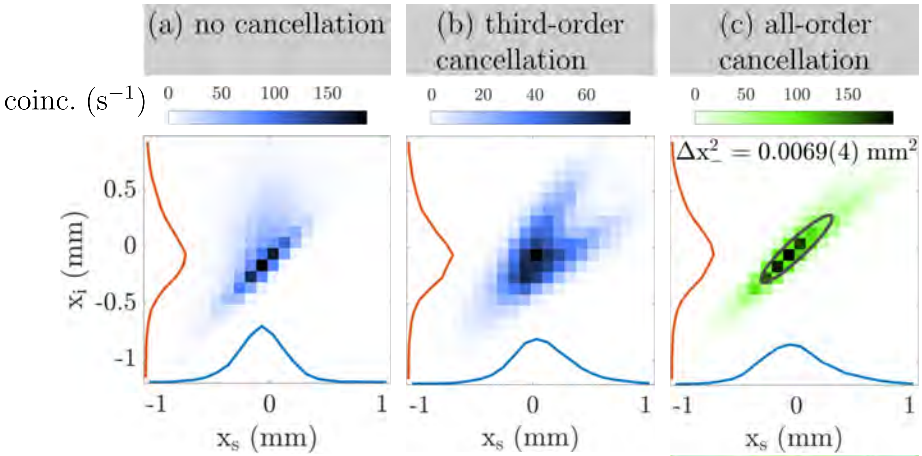

$\phi_s''(0)$	0	0	$-0.0154\ \mathrm{mm}^2$
$\phi_s'''(0)$	0	$0.0008\ \mathrm{mm}^3$	$0.0008\ \mathrm{mm}^3$
all plots	$\phi_i''(0) = 0.0154\ \mathrm{mm}^2,\ \phi_i'''(0) = 0.0008\ \mathrm{mm}^3$		

Figure 2.6: The position-basis coincidence distributions with both even- and odd-order aberrations introduced. (a) Quadratic and cubic aberrations are introduced to the idler path only, leading to a skewing and broadening of the coincidence distribution. In (b) only the cubic aberration is cancelled leading to a broadening of the distribution and the development of a forked structure. When both quadratic and cubic aberrations are cancelled the distribution approaches the form in Fig. 2.5(a).

the idler or the signal (b and c, respectively) the width of the position-basis coincidence distribution broadens substantially in both the x_- and x_+-directions, and Eq. (2.30) is no longer violated. The broadening in the x_+-direction is a result of the requirement that the marginal probability distributions for the signal or idler must broaden in the presence of defocus. After introducing defocus that is equal in magnitude but opposite in sign to both the signal and idler paths, the width of the position basis distribution along the x_--direction approaches the original width without aberrations. The state also returns to a form which violates Eq. (2.30). In all cases, the width of the coincidence distribution in the momentum domain does not change significantly because defocus is a multiplicative phase in this basis.

Fig. 2.6(a) shows the coincidence distribution when both quadratic and cubic aberrations are introduced into the idler path. Cubic aberrations are related to coma. One can observe a clear skewing of the distribution compared with Fig. 2.5(a). In Fig. 2.6(b) the coefficients of the cubic phase terms in each path are the same, leading to cancellation of skew. However, the distribution is broadened due to the inclusion of a quadratic phase shift in the idler path but not the signal path, and it displays a forked structure. The forked structure is consistent with the requirement that the marginal distributions for the signal and idler be skewed, but only the idler's marginal distribution can be broadened. Fig. 2.6(c) shows the coincidence distribution when both paths have the same coefficient for the cubic term in the phase shift, but equal and opposite coefficients for the quadratic term in the phase shift. It is clear that the coincidence distribution in Fig. 2.6(c) is approaching the form of the coincidence distribution without aberrations, but it displays an asymmetry along the x_+ direction. The imperfect cancellation of the phase shift introduced into each arm is a result of using a non-plane-wave pump.

2.4.1 Effect of Pump Profile

As mentioned earlier, the pump used in the generation of the signal and idler photons usually has a Gaussian mode profile. In this case, the momentum anti-correlation between the signal and idler photons is no longer perfect and complete aberration cancellation is no longer possible. To explore this behavior, consider the angular spectrum of a Gaussian pump,

$$v(\boldsymbol{\kappa}_p) = \frac{\pi v_0 w_0 e^{i\Phi(z)}}{w(z)\sqrt{\frac{1}{w(z)^4} + \frac{k^2}{4R(z)^2}}} \exp\left[\frac{-|\boldsymbol{\kappa}_p|^2}{4\left(\frac{1}{w(z)^2} - \frac{ik}{2R(z)}\right)}\right] \tag{2.37}$$

where $w(z) = w_0\sqrt{1 + (\lambda z/\pi w_0^2)^2}$ is the beam's radius, $R(z) = z\left[1 + (\pi w_0^2/\lambda z)^2\right]$ is the radius of the curvature of the beam's wavefront, $\Phi(z) = -\arctan(\lambda z/\pi w_0^2)$ is the Gouy phase, and w_0 is the beam waist. For simplicity, a collimated pump will be assumed such that $1/w(z)^2 >> k/2R(z)$ and $w(z) \to w_0$. Additionally, only quadratic phase aberrations will be introduced to the signal and idler paths such that $\phi_s''(0) = -\phi_i''(0) = 2\beta$. Finally, by setting $x_+ = 0$ only the x_--direction will be considered. After substituting Eq. (2.37) into Eq. (2.18) with these approximations, the spatial probability distribution takes the form $P(x_-) \propto \exp(-x_-^2/2\Delta x_-^2)$, where

$$\Delta x_-^2 = \frac{L_k^2 + (\frac{4\beta^2}{w_0^2} + \gamma L_k)^2}{2(\gamma L_k + \frac{4\beta^2}{w_0^2})}. \tag{2.38}$$

In the above equation $\ell_c/k_0 = L_k$. From Eq. (2.38) it is clear that the defocus introduced broadens the width of the coincidence distribution even though the aberrations were chosen according to the conditions for aberration cancellation. In the limit that $w_0 >> \beta$, the width of the distribution no longer depends upon the defocus introduced, as expected for the plane wave limit. While only quadratic aberrations were considered here, this demonstration shows that the pump profile influences the level of aberration cancellation possible.

One may consider why the incomplete cancellation is more obvious in Fig. 2.6(c) than in Fig. 2.5(d). The reason for this is due to the fact that there is more aberration introduced in the experiment displayed in Fig. 2.6 compared to the experiment in Fig. 2.5. Had $\phi_s''(0)$ and $\phi_i''(0)$ been greater in Fig. 2.5, the incomplete cancellation of defocus would have been more obvious.

2.4.2 Graphical Description of Aberration Cancellation

A graphical description of aberration cancellation[1] is shown in Fig. 2.7 [57]. For the sake of demonstration, a phase in the form of a 1D rectangular function is introduced to the signal and idler photons. Graphically, this process can be described by the grey bars overlayed on top of the joint momentum [Fig. 2.7(left)] or joint position [Fig. 2.7(right)] distributions. The phases introduced to each photon can only cancel one another where they overlap on the joint

---

[1] A conference proceeding for the presentation where this idea was first publicly described is referenced. However, the conference abstract does not reflect the fact that this idea was presented. The graphical interpretation of aberration cancellation can be attributed to my colleague Dr. Boris Braverman, QuEra Computing Inc.

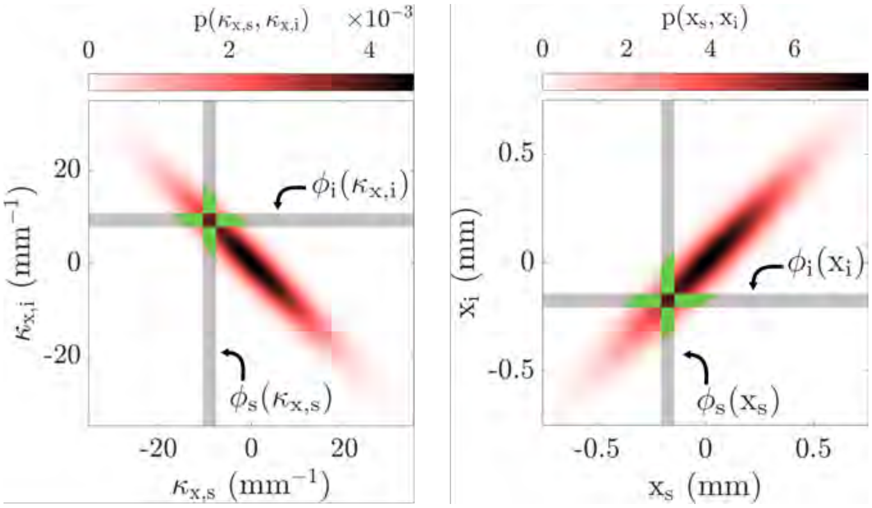

Figure 2.7: A graphical description of aberration cancellation. Phases are introduced to the signal and idler photons (grey bars) at a particular location in either the momentum basis (left) or position basis (right). These phases will only overlap on the joint momentum distribution if they are introduced at opposite locations relative to the origin of each photon's coordinate system. Conversely, in the position basis, the phases will only overlap if they are introduced at the same location relative to origin of each photon's coordinate system. The phases introduced to each photon can only cancel one another where they overlap on the joint distributions. If the signal and idler are not perfectly correlated, uncancelled phases may be present (green regions) and total aberration cancellation will not be possible.

probability distributions. Because the signal and idler produced in SPDC are anticorrelated in momentum, the phases must be introduced at opposite locations relative to the origin of each photon's coordinate system in order for them overlap on the joint momentum distribution. Furthermore, for the phases to cancel they must be equal in magnitude but opposite in sign. If the signal and idler photons are not perfectly anticorrelated in momentum, their joint momentum distribution will have dispersion along the diagonal direction. As a result, there will be areas where the phases introduced to the two photons do not overlap. These areas are highlighted in green in Fig. 2.7(left). Thus, the graphical method shows how complete cancellation of aberrations introduced in the momentum basis is not possible when the signal and idler photons are not perfectly anticorrelated in momentum. If the rectangular phases (aberrations) are introduced in the position basis [Fig. 2.7(right)], they must be introduced at the same location relative to the origin of each photon's coordinate system since the photons are correlated in position. Imperfect cancellation in the position basis results from imperfect position correlation, as indicated by the dispersion of the joint momentum distribution in the antidiagonal direction, Fig 2.7(right). The graphical method of describing aberration cancellation can be extended to other scenarios such as ghost imaging or the method of quantum phase imaging described in Chap. 3.

2.4.3 Aberration Cancellation in Ghost Imaging

To demonstrate the utility of nonlocal aberration cancellation, quantum imaging in the presence of focusing error and the nonlocal cancellation of this error was performed in one dimension. Three parallel Au bars placed in front of a bucket detector in the signal path constituted the image. To implement the bucket detector, photons passing through the Au bars were coupled into a MMF with an NA = 0.39 and a 400 μm core diameter using a 10x microscope objective with an NA = 0.25. The photons were detected using the same

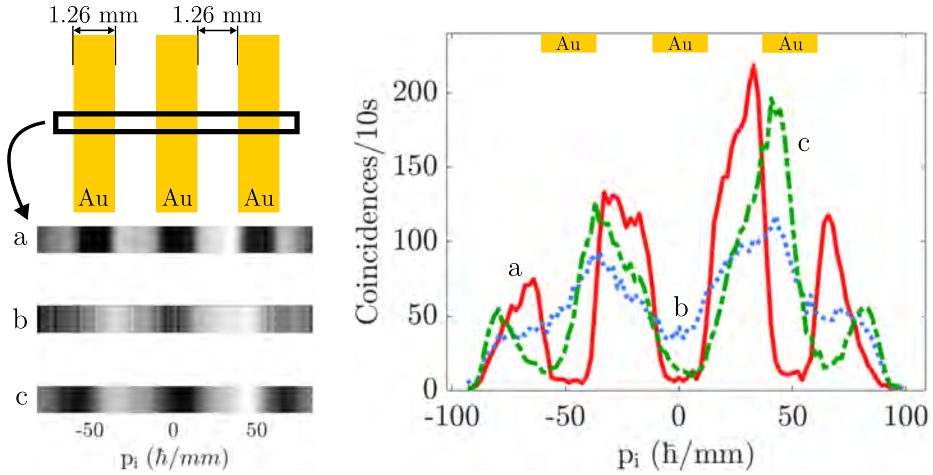

Figure 2.8: The solid red line is the coincidence image of three Au bars placed in the signal path without any aberrations present. Each bar has a width of 1.26 mm and a space of 1.26 mm is between each bar. The dotted blue line is the coincidence image with defocus in the signal path only, according to $\theta_s(x_s) = \theta_s''(0)x_s^2/2$, where $\theta_s''(0) = 73.7$ mm^{-2}. When the defocus is cancelled $[\theta_s''(0) = -\theta_i''(0)]$ nonlocally the coincidence image of the slits is almost completely recovered (dashed green line). An additional defocus of $\theta_i''(0) = -23.3$ mm^{-2} was introduced to account for alignment-related focusing error in the setup for all three cases.

SPCMs in Fig. 2.2. Unlike the experiments shown in Fig. 2.2, defocus was introduced in the image plane of the crystal and coincidence measurements (imaging) took place in the Fourier plane of the crystal. This configuration was chosen to take advantage of the larger beam cross section in the Fourier plane. The x-coordinate of the signal photons was reversed before interacting with the SLM. As a result, the coefficients of the quadratic aberrations in the signal and idler paths must be equal in magnitude and opposite in sign for complete cancellation to occur.

From the results shown in Fig. 2.8, the coincidence image of the slits is clearly lost and then almost completely recovered with defocus cancellation. The lack of perfect recovery is due to the length of the crystal generating the entangled photons. Imperfect cancellation in the momentum basis can be understood following an analysis similar to that which led to Eq. (2.38), but where aberrations are introduced in the position basis and the effect on the joint momentum distribution is measured. In this case, the relevant width to consider is $\Delta\kappa_{x,+}$ since it describes momentum anticorrelation. If second-order aberrations have been introduced in the position basis according to the condition for perfect cancellation ($\theta_s''(0) = -\theta_s''(0) = 2\beta$), and a finite-length crystal is used,

$$\Delta\kappa_{x,+}^2 = \frac{2\left[\frac{1}{4w_0^4\gamma^2} + \left(\frac{1}{2w_0^2} + \frac{4\beta^2 L_k(1+\gamma^2)}{\gamma}\right)^2\right]}{\frac{4\beta^2 L_k(1+\gamma^2)}{\gamma} + \frac{1}{2w_0^2}\left(1 + \frac{1}{\gamma^2}\right)} \tag{2.39}$$

Thus, when $L_k > 0$, the effect of aberrations introduced in the position basis cannot be perfectly cancelled in the joint momentum distribution. As $L_k \longrightarrow 0$, $\Delta\kappa_{x,+}$ no longer depends on β and defocus is perfectly cancelled.

2.5 Conclusion

This chapter shows how aberrations and their subsequent nonlocal cancellation affect the results of transverse entanglement measurements using the criterion defined in Eq. (2.30). Furthermore, the results of this chapter constitute first-reported nonlocal and simultaneous cancellation of even- and odd-order aberrations. This technique was applied to nonlocally correct for focusing error in a quantum imaging setup. By using SLMs to correct for aberrations rather than physically moving optics, the optimization of quantum imaging experiments can be done in a highly controlled manner. Furthermore, aberrations due to the imperfect manufacturing and design of optics can be corrected as well. Future work could more deeply explore the lack of perfect aberration cancellation due to the use of a non-plane-wave pump beam or in the non-paraxial regime. In our experiment, the entangled photons used to demonstrate nonlocal aberration cancellation were the same wavelength. However, non-degenerate SPDC produces entangled signal and idler photons that have different wavelengths. These non-degenerate entangled photons have been used to demonstrate imaging at wavelengths where efficient and affordable cameras are not available [58]. Future research could involve performing nonlocal aberration cancellation in this "two-color" imaging scheme, demonstrating aberration correction at wavelengths where adaptive optics are either unavailable or insufficient. It may also be possible to demonstrate nonlocal aberration cancellation using a light source with classical, rather than quantum mechanical, correlations.

3. Quantum-enhanced phase imaging

3.1 Introduction

Before the advent of phase-contrast [59], differential interference contrast [60], and quantitative phase imaging [61–63] techniques, forming an intensity image of a phase-only object and measuring the phase imparted by that object was an outstanding problem in biological imaging. Briefly, Zernike's phase contrast method relies upon destructive interference between the low and high spatial frequency content of an image, resulting in enhanced contrast near sharp features in the image. Differential interference contrast relies upon interference between light that has passed through nearby points on a phase-only object, allowing the measurement of phase-gradients on a phase-only object. Though they are inherently stable, phase-contrast and differential interference contrast modalities do not measure the value of the phase shift imparted by a phase-only object. Generically, quantitative phase imaging is a method to reconstruct the phase imparted to coherent light that has passed through a phase-only object by interfering it with a reference beam.

Spatially entangled photons have enabled imaging at wavelengths where cameras are inadequate [58] and with a higher resolution than classical coherent imaging [64, 65]. Position-momentum entanglement has also been utilized to develop new adaptive optics schemes [66–68], and recently, new phase imaging modalities have been developed using entangled photons. In 2019, spatially entangled photons were used to measure both amplitude and phase in low-light Fourier ptychography [69]. In 2020, Defienne et al. reported a new phase-shifting holography scheme that utilized spatial and polarization entanglement [70]. Similarly, in 2021 Camphausen et al. demonstrated a version of differential interference contrast imaging that used polarization and spatial entanglement [71]. Induced coherence without induced emission in spontaneous parametric down-conversion was employed by Lemos et al. to image a phase-only object that was opaque at the detection wavelength [72, 73]. Lemos's paper inspired several other demonstrations and ideas based on induced-coherence imaging [74–77]. Induced coherence has also been used to perform infrared spectroscopy of gaseous samples without the use of an infrared source or infrared detection equipment [78].

This chapter reports on a wide-field quantitative phase imaging technique that relies upon quantum interference between sequential down-conversion events in a double-passed nonlinear crystal. As compared to classical phase-shifting holography, the quantum technique reported here achieves twice the phase shift and approximately 1.7 times the resolution when imaging a phase-only object. Furthermore, it is this double phase shift that separates this chapter's quantum phase imaging scheme from similar induced-coherence imaging techniques [73, 76, 79], though the imaging photons must be detected in our scheme. Like quantum-enhanced differential interference contrast microscopy, this method achieves twice the phase shift [71], but the contrast in the measured phase does not come at the expense of resolution. Because the object is illuminated with approximately 40 photons/s/μm^2 and at a near-infrared wavelength (810 nm), this low-light imaging technique may be useful for imaging phase-only biological samples that are sensitive to photon flux or are prone to photobleaching, without the loss of resolution associated with imaging at longer wavelengths [9, 10]. Typically, a biological object is considered phase-only if it is unstained and thin relative to the depth of focus. Importantly, this applies to live-cell imaging in various media. Though this quantum phase imaging method utilizes the strong momentum and position correlation of entangled photons produced in spontaneous parametric down-conversion, detecting the photons in coincidence is not required. The field of coincidence imaging has made strides in recent years [11, 80, 81], but state-of-the-art coincidence imaging still requires tens of hours for data collection. All measurements necessary to generate a phase image using the methods of this chapter were collected in tens of seconds, bringing the timescale of quantum imaging closer to that of biological processes. Though the low-light imaging method reported in this chapter does not take advantage of the signal-to-noise enhancement associated with coincidence imaging [82], it can easily accommodate coincidence imaging techniques as equipment that enables shorter acquisition times becomes more readily available [83, 84].

3.2 Background

The experimental setup (explained in more detail later) for generating entangled photons that interact with a phase-only object is shown in Fig. 3.1(b). Briefly, the method shown in Fig. 3.1(b) relies upon the interference between entangled photons created from spontaneous parametric down-conversion of a pump beam that passes through a nonlinear crystal (BBO) twice. Recalling Eq. (2.19), the momentum-representation wave function for photons created in a single spontaneous parametric down-conversion event is given by,

$$\psi_0(\boldsymbol{\kappa}_\mathrm{s}, \boldsymbol{\kappa}_\mathrm{i}) = C\nu(\boldsymbol{\kappa}_\mathrm{s} + \boldsymbol{\kappa}_\mathrm{i})\tilde{\chi}^{(2)}(\boldsymbol{\kappa}_\mathrm{s} - \boldsymbol{\kappa}_\mathrm{i}). \tag{3.1}$$

where s, i denote the signal and idler photons, respectively, C is a constant that includes properties of the nonlinear crystal [67], and $\boldsymbol{\kappa}$ represents the transverse component of the photons' wave vectors. The two-photon wave function in the position-representation is simply the inverse Fourier transform of $\psi_0(\boldsymbol{\kappa}_\mathrm{s}, \boldsymbol{\kappa}_\mathrm{i})$:

$$\Phi_0(\boldsymbol{x}_\mathrm{s}, \boldsymbol{x}_\mathrm{i}) = \mathcal{F}^{-1}\left\{\psi(\boldsymbol{\kappa}_\mathrm{s}, \boldsymbol{\kappa}_\mathrm{i})\right\}, \tag{3.2}$$

where the inverse Fourier transform, denoted $\mathcal{F}^{-1}$, occurs over both the $\boldsymbol{\kappa}_\mathrm{s}$ and $\boldsymbol{\kappa}_\mathrm{i}$ coordinates. In Fig. 3.1(b), the signal and idler photons experience the same phase-only object described by the function $\phi_\mathrm{obj}(\boldsymbol{x}_j)$, where $j = \mathrm{s}, \mathrm{i}$. As a result, the two photon wave function takes the form

$$\Phi_1(\boldsymbol{x}_\mathrm{s}, \boldsymbol{x}_\mathrm{i}) = \exp\left[i\left(\phi_\mathrm{obj}(\boldsymbol{x}_\mathrm{s}) + \phi_\mathrm{obj}(\boldsymbol{x}_\mathrm{i})\right)\right]\Phi_0(\boldsymbol{x}_\mathrm{s}, \boldsymbol{x}_\mathrm{i}), \tag{3.3}$$

If the photons described by the state in Eq. (3.3) pass back through the nonlinear crystal with the pump beam in such a way that the signal and idler modes from one pass are matched to those of the second pass, it is not possible to determine whether a detected photon was created on the first pass or the second pass through the crystal. Mathematically, this effect can be observed by applying the time translation operator for SPDC to the state in Eq. (3.3) including the vacuum contribution that was omitted:

$$|\psi_2(\boldsymbol{\kappa}_s, \boldsymbol{\kappa}_i, t)\rangle \propto \left(1 - \frac{i}{\hbar}\int_0^t d\tau \hat{\mathcal{H}}(\tau)\right)\left[|0\rangle + |\psi_1(\boldsymbol{\kappa}_s, \boldsymbol{\kappa}_i, t)\rangle\right] \tag{3.4}$$

The application of the SPDC time translation operator to Eq. (3.3) and the vacuum results in several terms on the RHS of Eq. (3.4) resulting from various nonlinear optical processes inside the nonlinear crystal. However, some of these terms can be ignored because $\hat{\mathcal{H}}|\psi_1\rangle$ is proportional to the second order nonlinear susceptibility to the second order. Furthermore, the signal and idler fields are very weak compared to the pump and do not stimulate a significant nonlinear response in the crystal. These factors justify the omission of the term involving $\hat{\mathcal{H}}|\psi_1\rangle$ from Eq. (3.4). Thus, after carrying out a calculation similar to the one that led to Eq. (2.19) and switching to the position representation, the two-photon wave function after the second pass through the crystal is,

$$\Phi_2(\boldsymbol{x}_\mathrm{s}, \boldsymbol{x}_\mathrm{i}) = \Phi_0(\boldsymbol{x}_\mathrm{s}, \boldsymbol{x}_\mathrm{i}) \left(\exp(i\theta) + \exp\left[i \left(\phi_\mathrm{obj}(\boldsymbol{x}_\mathrm{s}) + \phi_\mathrm{obj}(\boldsymbol{x}_\mathrm{i}) \right) \right] \right) / \sqrt{2}, \tag{3.5}$$

where θ is any additional phase acquired by the pump between the first and second pass. The probability of detecting only the signal photon is obtained by integrating $|\Phi_2(\boldsymbol{x}_\mathrm{s}, \boldsymbol{x}_\mathrm{i})|^2$ over the entire coordinate space of $\boldsymbol{x}_\mathrm{i}$, i.e. calculating the marginal probability distribution of the joint probability distribution. In practice, it is easiest to perform the integration numerically. However, if the pump is assumed to be a plane wave and the nonlinear crystal is thin enough so that $\chi^{(2)}(\boldsymbol{x}_\mathrm{s} - \boldsymbol{x}_\mathrm{i}) \approx \delta(\boldsymbol{x}_\mathrm{s} - \boldsymbol{x}_\mathrm{i})$, where $\chi^{(2)}(\boldsymbol{x}_\mathrm{s} - \boldsymbol{x}_\mathrm{i}) = \mathcal{F}^{-1}\left\{ \tilde{\chi}^{(2)}(\boldsymbol{\kappa}_\mathrm{s} - \boldsymbol{\kappa}_\mathrm{i}) \right\}$, it is possible to analytically calculate the probability of detecting only the signal photon,

$$P(\boldsymbol{x}_\mathrm{s}) = C \left(1 + \cos\left[2\phi_\mathrm{obj}(\boldsymbol{x}_\mathrm{s}) - \theta \right] \right) / \sqrt{2} \tag{3.6}$$

Thus, the image formed on the camera (EMCCD) in Fig. 3.1(b) is an interference pattern that corresponds to the phase-only object but with twice the phase shift.

The phase object can be reconstructed by employing phase-shifting holography. In classical phase-shifting holography, the light that interacted with the phase-only object interferes with a reference field, and the resulting interference pattern, I, is recorded for four different phase shifts of the reference field: $\phi = \arg\left[I_0 - I_\pi + i \left(I_{\pi/2} - I_{3\pi/2} \right) \right]$, where the subscript on I indicates the reference phase [62]. In quantum phase-shifting holography, the reference phase is any extra phase acquired by the pump before passing through the nonlinear crystal a second time, θ in Eq. (3.6). Alternatively, the phase of the pump can remain fixed while a constant phase offset is applied to the photons that interacted with the phase object, but the constant phase offset must be negative rather than positive in this case. The absolute value of the reference phase applied to the entangled photons must also be half

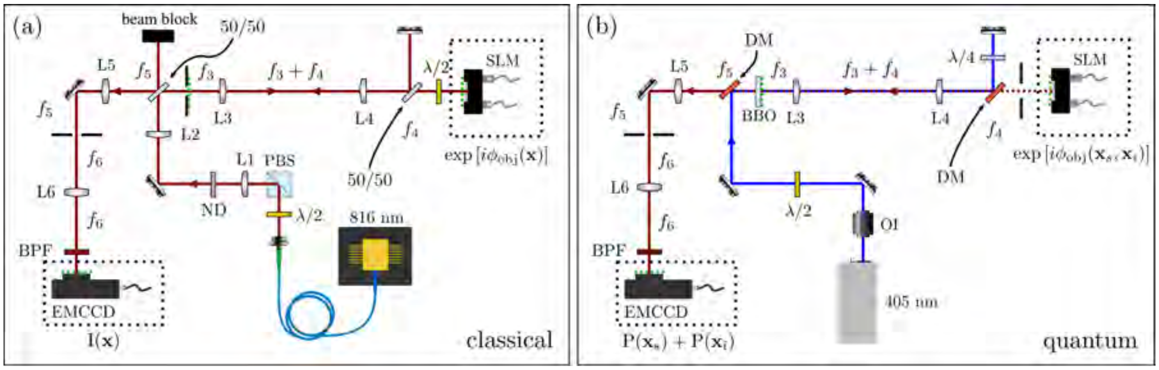

Figure 3.1: Experimental setup for (a) classical phase-shifting holography and (b) quantum phase-shifting holography. Green dotted lines indicate conjugate image planes. 405 nm - narrow linewidth (<5 MHz), 100 mW, 405 nm laser; 50/50 - 50/50 beamsplitter; 816 nm - 33 μW, 816 nm laser; BPF - 810 ± 5 nm bandpass filter; BBO - type-I beta-barium borate crystal; DM - long-pass dichroic mirror; EMCCD - electron-multiplying camera; f_3 = 10 cm; f_4 = 30 cm; f_5 = 12.5 cm; f_6 = 40 cm; L1 - 10 cm lens; L2 = 30 cm lens; L3 - 10 cm achromatic doublet lens; L4 - 30 cm achromatic doublet lens; L5 - 12.5 cm lens; L6 - 40 cm lens; $\lambda/2$ - half-wave plate; $\lambda/4$ - quarter-wave plate; ND - neutral density filters, optical density = 7; OI - optical isolator; PBS - polarizing beamsplitter.

the value used in classical phase shifting holography since both photons acquire the phase shift. In Fig. 3.1(b) the reference phase is applied by the spatial light modulator (SLM) that also forms the phase object, in effect changing the global phase of the phase object. Thus, the phase is reconstructed as follows:

$$\phi_{\text{obj}}(\boldsymbol{x}_{\text{s}}) = \tan^{-1}\left[\frac{P_{-\pi/4}(\boldsymbol{x}_{\text{s}}) - P_{-3\pi/4}(\boldsymbol{x}_{\text{s}})}{P_0(\boldsymbol{x}_{\text{s}}) - P_{-\pi/2}(\boldsymbol{x}_{\text{s}})}\right], \tag{3.7}$$

where the subscript on P is the value of the constant phase offset added to the SLM. It is worth noting that phase-shifting holography with four phase shifts, like in Eq. (3.7), reaches the Cramer-Rao bound for phase estimation [85].

3.3 Experiment

The experimental setups for classical phase-shifting holography and quantum phase-shifting holography are shown in Fig. 3.1(a) and Fig. 3.1(b), respectively.

3.3.1 Classical Experiment

In the classical experiment, an $\sim 33\ \mu$W, 816 nm diode laser is attenuated by a half-wave plate ($\lambda/2$), polarizing beamsplitter (PBS), and a series of neutral density filters (ND) with a total extinction of approximately 10^{-7}. The attenuation is set so that the photon flux incident on the object is the same as in the quantum experiment ($\sim$ 40 photons/s/μm^2), as measured by the EMCCD in photon counting mode. Furthermore, the laser is operated near threshold to mimic the occurrence of background fluorescence created by the 405 nm pump as it passes through lenses in the quantum experiment. To do this, the laser current is set so that the visibility of interference is the same as in the quantum experiment, which is limited by background fluorescence. The polarization is set to vertical by a PBS because the 50/50 plate beamsplitter (50/50) that forms the interferometer is truly 50/50 for the vertical polarization only. The first 50/50 beamsplitter serves to make the layout of the classical experiment similar to the quantum experiment. The beam is expanded to have a diameter of $\sim$ 1 mm using a Keplerian telescope with a magnification of 3X (L1 and L2). The beam is then directed into another Keplerian telescope consisting of two achromatic doublet lenses (L3 and L4) with a 3X magnification. A 5 mm-diameter aperture is placed a distance f in front of L3 to mimic the aperture of the nonlinear crystal used in the quantum experiment (BBO). After passing through the telescope, the beam is split by a 50/50 beamsplitter to form a Michelson interferometer. One arm of the Michelson interferometer is terminated by a reflective phase-only SLM (Hamamatsu X15213-02) that forms the phase object (ϕ_{obj}) and introduces a constant phase offset for phase-shifting holography. The other arm is terminated by a mirror, and both arms are the same optical length. A half-wave plate placed between the 50/50 beamsplitter and SLM rotates the polarization to be along the optical axis of the SLM and rotates it back to vertical after reflecting from the SLM. The beam that interacted with the SLM and the reference beam reflect back through the telescope made from L3 and L4 and the first 50/50 beamsplitter before passing through another Keplerian telescope with a 3.2X magnification (L5 and L6). An adjustable aperture placed a distance f_2 = 12.5 cm from L5 (the Fourier plane of the SLM), limits the spatial bandwidth of the imaging system, but is only engaged when comparing the resolution of the quantum and classical experiments, Fig. 3.4. The image of the active area of the SLM is then brought to an electron-multiplying CCD camera (EMCCD, Andor iXon Ultra 888-EXF) by L6.

3.3.2 Quantum Experiment

In the quantum experiment, a narrow linewidth (< 5 MHz) 405 nm laser beam (Toptica TopMode 405) passes through an optical isolator (OI) and half-wave plate ($\lambda/2$) before being directed though a 0.5 mm-long beta-barium borate crystal (BBO) by a long-pass dichroic mirror (DM). The diamter of the 405 nm pump beam at the BBO crystal is ~ 1 mm. A 405 nm pump photon is converted to two 810 nm position-momentum entangled photons in the BBO crystal through degenerate type-I spontaneous parametric down-conversion. Both the entangled photons and pump beam pass through the same Keplerian telescope used in Fig. 3.1(a) consisting of two achromatic doublet lens (L3 and L4). The telescope images the output facet of the nonlinear crystal onto the active area of the SLM (green dotted line). A second long-pass dichroic mirror placed after L4 splits the pump beam and entangled photons so that only the 810 nm entangled photons interact with the SLM. The SLM imprints both the phase object and constant reference phase for phase-shifting holography on the entangled photons. Accordingly, the phase of the pump is held fixed. A 1.1 cm-diameter aperture is placed betwen the dichroic mirror and SLM to mimic the aperture of the half-wave plate just before the SLM in the classical experiment. The visibility of interference between successive down-conversion events is lower than 100 percent because the combined transmission of L3 and L4 is ~ 90 percent. To compensate for this and recover interference visibility, the polarization of the pump is set for imperfect phase-matching before the first pass through the nonlinear crystal using a half-wave plate ($\lambda/2$) and set for perfect phase matching using a double-passed quarter-wave plate ($\lambda/4$) between the first and second passes through the nonlinear crystal [86]. After the entangled photons reflect from the SLM and the pump reflects from a mirror, the pump and entangled photons are recombined at the dichroic mirror. They pass back through the telescope formed by L3 and L4 and through the nonlinear crystal. The first dichroic mirror then splits the pump and entangled photons, and the entangled photons pass through a 3.2X telescope that images the SLM onto the EMCCD. Like the classical experiment, an adjustable aperture is placed in the Fourier plane of the phase object to compare the resolution of the quantum experiment with the classical experiment.

3.3.3 Correcting Unwanted Aberrations

The active area of the SLM used in this experiment is not completely flat when a phase shift of zero radians is programmed on every pixel. Though the manufacturer supplies a calibration file to remove this effect, it did not completely remove the background phase in practice. Furthermore, the waveplates placed in the beam path between the two passes through the nonlinear crystal added additional phase aberrations that needed to be corrected. To mitigate unwanted background phase structures, phase-shifting holography was performed with no object programmed on the SLM. The measured phase was then used to cancel the unwanted phase structures in the experiment. Figure 3.2 shows the result of measuring aberrations with photons produced in SPDC. The measured aberration in Fig. 3.2 is the average of 100 measurements at each reference phase in Eq. (3.7). To obtain the uncertainty in the phase

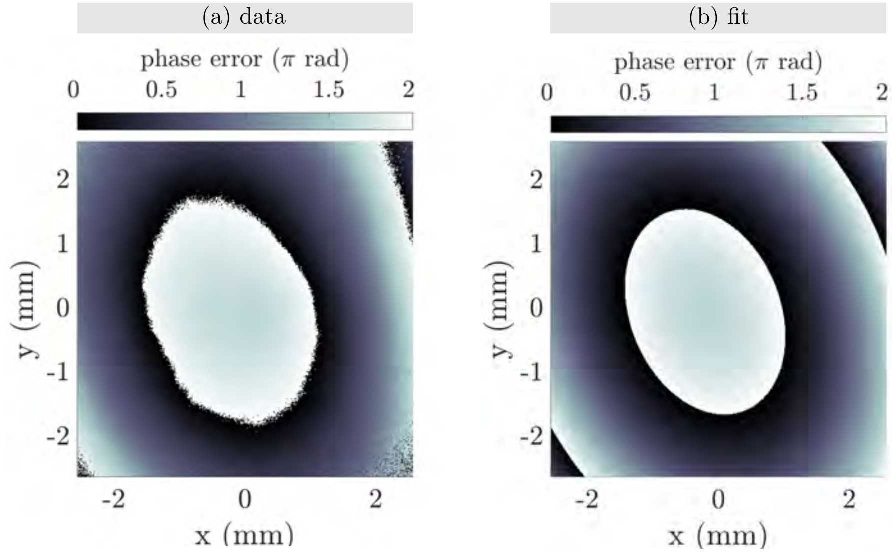

Figure 3.2: (a) Measured phase error of the optical system in Fig. 3.1 and (b) fit using a model of a bivariate quadratic. In the particular example above, the photons from SPDC were used to measure unwanted aberrations. Only the area of the SLM illuminated by the down-conversion photons was used for the calibration, and the measured phase is twice what each individual signal or idler photon experiences.

measurement, error propagation is performed using Eq. (3.7),

$$d\phi_{obj} = \sqrt{\left[\frac{\partial \phi_{obj}}{\partial P_{-\pi/4}}\sigma_{-\pi/4}\right]^2 + \left[\frac{\partial \phi_{obj}}{\partial P_{-3\pi/4}}\sigma_{-3\pi/4}\right]^2 + \left[\frac{\partial \phi_{obj}}{\partial P_{0}}\sigma_{0}\right]^2 + \left[\frac{\partial \phi_{obj}}{\partial P_{-\pi/2}}\sigma_{-\pi/2}\right]^2}, \tag{3.8}$$

where σ_j is the uncertainty in the intensity measured at each phase shift, $j = -\pi/4, -3\pi/4, 0, -\pi/2$.

Note that spatial dependence of $d\phi_{obj}$ has been suppressed in Eq. (3.8). The partial derivatives in Eq. (3.8) are as follows:

$$
\begin{aligned}
\frac{\partial \phi_{obj}}{\partial P_{-\pi/4}} &= \frac{P_0 - P_{-\pi/2}}{\left(P_0 - P_{-\pi/2}\right)^2 + \left(P_{-\pi/4} - P_{-3\pi/4}\right)^2} \\
\frac{\partial \phi_{obj}}{\partial P_{-3\pi/4}} &= -\frac{\partial \phi_{obj}}{\partial P_{-\pi/4}} \\
\frac{\partial \phi_{obj}}{\partial P_0} &= -\frac{P_{-\pi/4} - P_{-3\pi/4}}{\left(P_0 - P_{-\pi/2}\right)^2 + \left(P_{-\pi/4} - P_{-3\pi/4}\right)^2} \\
\frac{\partial \phi_{obj}}{\partial P_{-\pi/2}} &= -\frac{\partial \phi_{obj}}{\partial P_0}
\end{aligned}
\tag{3.9}
$$

Because the measured value of the phase flatness, Fig. 3.2(a), contains experimental uncertainty, a model of a bivariate quadratic is fit to the data and the result is used as the phase correction,

$$\phi_{err}(x, y) = a(x-b)^2 + c(y-d)^2 + e(x-f)(y-g) + h. \tag{3.10}$$

The model of Eq. (3.10) has eight fitting parameters, a, b, c, d, e, f, g, and h. The model is fit using maximum likelihood estimation assuming the phase data are Gaussian distributed random variables (i.e. the least squares method). The data [Fig. 3.2(a)] are modeled quite well by Eq. (3.10) [Fig. 3.2(b)]. The presence of higher-order aberrations account of the lack of perfect agreement between the fit and the data. In practice, the model corrects the aberrations quite well, and this aberration correction routine was performed during the alignment of both the quantum and classical experiments.

3.4 Results

3.4.1 Comparison of Classical and Quantum Phase Sensitivity

Figure 3.3 shows the results of a phase reconstruction experiment using classical and quantum phase-shifting holography. The phase object encoded on the SLM is shown in Fig. 3.3(a). A line cut through a portion of the object, Fig. 3.3(b), is approximately a rectangular function with a height of $\pi/2$ rad. The results of classical phase-shifting holography are shown in Fig. 3.3(c) and (d). For each reference phase shift used to construct the phase images in Fig. 3.3, ten frames are averaged together. The EMCCD is set to have an EM gain of 1000, an exposure time of 0.02 s, and is operated in photon-counting mode. The phase image in Fig. 3.3 agrees well with the phase object, but contains a slight astigmatism due to the use of plate-style 50/50 beamsplitters in the optical path. The camera is placed in a plane where the vertical direction is in focus to make fitting to the vertical line cut (blue line) more straightforward. The line cut and fit for the classical experiment are shown in Fig. 3.3(d). Using maximum likelihood estimation (MLE) with the model of a rectangular function, the maximum phase shift in the line cut is estimated to be 1.6(1) rad, consistent with the maximum phase shift of the encoded phase object. The uncertainty in the fit is obtained through Monte Carlo simulation.

The results of phase imaging using quantum light are shown in Fig. 3.3(e), where the location of the line cut is indicated by the green line. The phase image agrees well with the encoded phase object, albeit with twice the phase shift. The astigmatism associated with the plate-style dichroic mirrors is less present in the quantum experiment because they are half as thick as the 50/50 beamsplitters in the classical experiment. The double phase shift is clearly present in the line cut, Fig. 3.3(f). MLE returns a maximum phase shift of 3.3(1) rad, confirming the double phase shift effect. It is worth noting that quantum phase-shifting holography achieves an estimate of the phase with half the fractional uncertainty of the

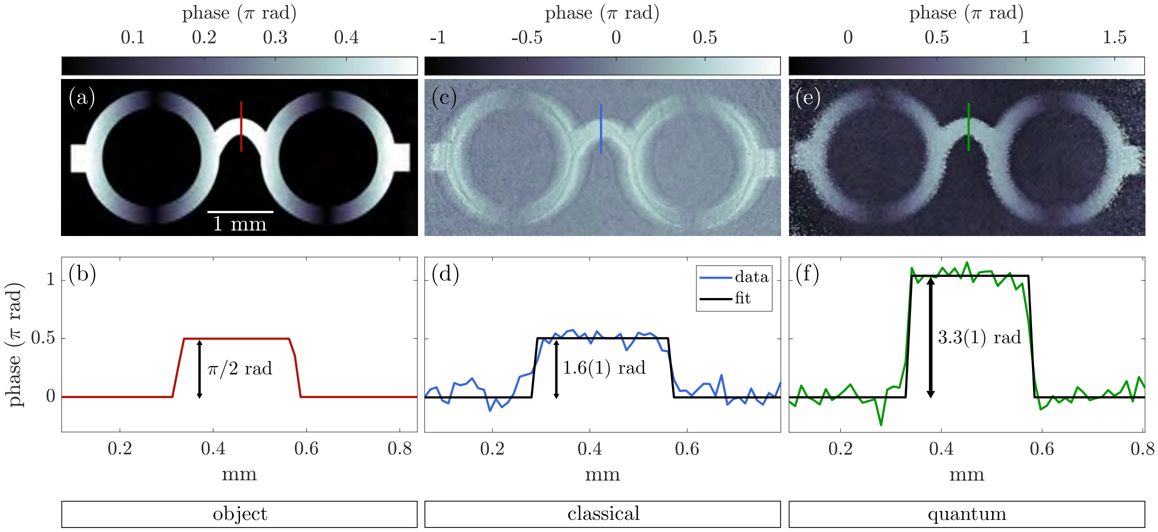

Figure 3.3: A comparison of phase-shifting holography using classical coherent light with a wavelength of 816 nm (c and d) and "which crystal" quantum interference between photons with a wavelength of 810 nm (e and f). The phase object (a) is an illustration of round eyeglasses, and a line cut through the nosepiece (red line) is approximately a rectangular function of height $\pi/2$ rad (b). The result of classical phase-shifting holography is shown in (c). The ringing around the edges of the classical phase image is due to astigmatism induced by the plate beamsplitters in Fig. 3.1(a), but the camera is placed in a plane where the vertical direction is in focus. A rectangular function is fit to a line cut through the nosepiece (blue line) using maximum likelihood estimation (d), returning a phase shift of 1.6(1) rad. The result of quantum phase-shifting holography is shown in (e), and the fit to a line cut through the nosepiece (green line) is shown in (f). With a maximum phase shift of 3.3(1) rad, the quantum phase-shifting holography result has approximately twice the phase shift and half the fractional uncertainty of classical phase-shifting holography.

classical phase-shifting holography method, even though the photons that interacted with the phase object were not half the wavelength. Of course, the improvement of fractional uncertainty using quantum phase-shifting holography cannot be achieved in environments with significant mechanical instability since the double phase shift would enhance the effect of mechanical vibrations on the phase uncertainty. The primary sources of noise in the measurement of the phase were background light and noise associated with the EM amplification in the EMCCD [11, 87].

3.4.2 Comparison of Classical and Quantum Imaging Resolution

Equation (3.6), though illustrative, implies an infinite spatial resolution. In reality, the spatial resolution of the quantum phase-shifting holography method described in Fig. 3.1(b) is limited by the width of the position correlation between the signal and idler photons and the apertures placed in the optical path [79, 88]. A comparison of the aperture-limited resolutions for quantum and classical phase-shifting holography are shown in Fig. 3.4. To perform these measurements, a horizontally oriented adjustable slit was placed a distance f_2 away from the lens L5 the telescope just before the camera. The location of the slit corresponded to the Fourier plane of the phase object and nonlinear crystal. The width of the slit was fixed at 4.5 mm for both the quantum and classical experiments. A series of three equally spaced bars along the horizontal direction formed the phase object, Fig. 3.4(a). Each bar had a phase of $\pi/2$ above the background. The space between each bar was equal to the width of a single bar. The spatial frequency of the bars in the top, middle, and bottom rows of Fig. 3.4 were 8 lp/mm, 10 lp/mm, and 13.3 lp/mm, respectively. The aperture-limited resolution was measured rather than the correlation-limited resolution because it is possible to increase the correlation-limited resolution by altering the magnification of the optical system between the crystal and object [79]. Nonetheless, the correlation-limited resolution

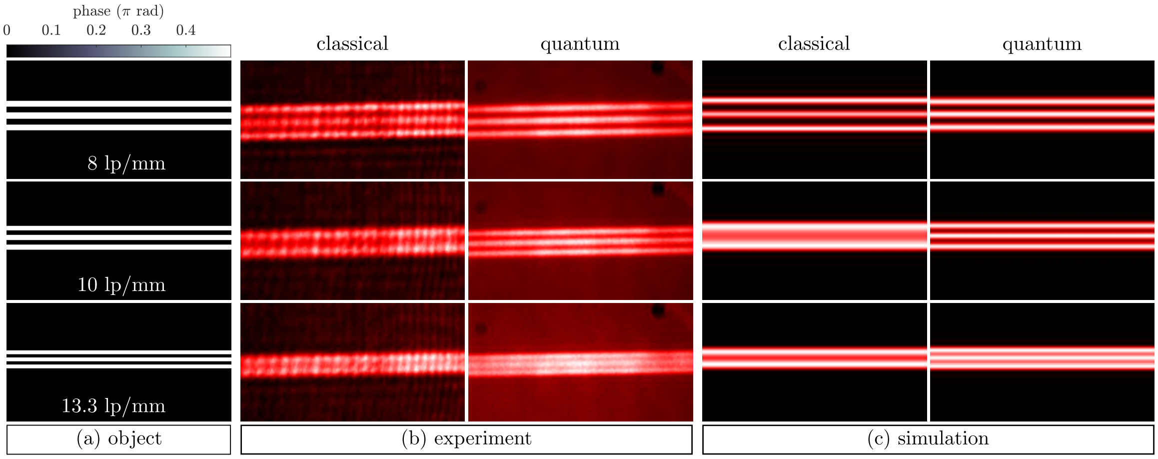

Figure 3.4: A comparison of resolution for classical phase-shifting holography and quantum phase-shifting holography. (a) A series of three horizontal bars with a maximum phase shift of $\pi/2$ were used to measure resolution. The spatial frequency of the bars varied from 8 lp/mm (top row) to 10 lp/mm (middle row) to 13.3 lp/mm (bottom row). (b) Experimental results (interferograms) indicate that the three bars are clearly resolved in both the quantum and classical experiments at a spatial frequency of 8 lp/mm (top row). However, only the quantum phase-shifting holography scheme can resolve the bars at a spatial frequency of 10 lp/mm (middle row) and 13.3 lp/mm (bottom row). (c) A simulation of the experiments in Fig. 3.1 agrees very closely with the experimental results in (b).

is estimated to be $\sim 30\ \mu$m (or $\sim$ 17 lp/mm) using a crystal of length 0.5 mm and using the optical system in Fig. 3.1(b). The resolution limit is assumed to be twice the standard deviation of the position correlation of the signal and idler.

The resolution measurements are shown in Fig. 3.4(b). Each image in Fig. 3.4(b) is the average of 100 frames collected by the camera with an EM gain 213 and exposure time of 0.22 s. Furthermore, the each image represents a single interferogram with the background in destructive interference and the bars in constructive interference. The three bars are clearly resolved at 8 lp/mm (top row) in both the classical (top left) and quantum experiments (top right). Extraneous fringes are present in the classical experiment due back-reflected light from lenses L3 and L4. Interestingly, these fringes do not appear in the quantum experiment because the back reflected light is not mode-matched with the entangled photons created on the second pass through the crystal. The quantum results have extraneous background noise due to broadband fluorescence created by the pump passing through lenses L3 and L4. At 10 lp/mm (middle row), the classical experiment is no longer able to resolve the three bars (middle left), but the three bars are clearly resolved in the quantum experiment (middle right). At 13.3 lp/mm (bottom row), the three bars are still resolved in the quantum experiment (bottom right) but with lower visibility than for bars at 10 lp/mm. The three bars at 13.3 lp/mm are not resolved in the classical experiment (bottom left).

The experimental results in Fig. 3.4(b) agree very closely with numerical simulation, Fig. 3.4(c). The simulation was performed using Fresnel propagation of the classical field and two-photon state in Eq. (3.1), and it included all apertures present in Fig. 3.1. Though the imaging systems in Fig. 3.1 are not extremely complex, the operator approach described in Ref. [89] simplifies the simulation significantly. The four primary operations used to perform the simulations are multiplication by a quadratic-phase exponential, Fourier transformation, and multiplication by a binary pupil function. Multiplication by a quadratic phase is defined as,

$$\mathcal{Q}[c]\{E(x)\} = \mathrm{e}^{ikcx^2/2}E(x). \tag{3.11}$$

Note that in Eq. (3.11), x is a stand-in variable for the space where $\mathcal{Q}$ is applied. As such, c must have units such that the argument of the exponential is unitless. Fourier transformation is defined in the usual way,

$$\mathcal{F}\{E(x)\} = \int_{-\infty}^{\infty} dx E(x)\mathrm{e}^{-i\kappa_x x} \tag{3.12}$$

Multiplication by a binary pupil function is defined as,

$$P[w]\{E(x)\} = (|x| <= w)E(x), \tag{3.13}$$

where w is half the width of the pupil. Free-space propagation and propagation through a material are defined in terms of Fourier transformation and multiplication by a quadratic phase,

$$R\left[\frac{d}{n}\right]E(x) = \mathcal{F}^{-1}\left\{Q\left[-\frac{d}{nk^2}\right]\left\{\mathcal{F}\{E(x)\}\right\}\right\}, \tag{3.14}$$

where n is the refractive index of the material through which the light propagates. Free-space propagation is accomplished by setting $n = 1$.

If $E(x)$ is the field just after the pupil between the first 50/50 beamsplitter and L3 in the classical experiment, the field at the SLM after the first pass through telescope defined by L3 and L4 is,

$$\begin{aligned} E_{SLM}(x) = \mathrm{e}^{i\phi_{bars}} R\left[f_4 - \frac{t_{50/50}\sqrt{2}}{n_{50/50}} - l_1\right] R\left[\frac{t_{50/50}\sqrt{2}}{n_{50/50}}\right] R[l_1] Q\left[-\frac{1}{f_4}\right] \cdots \\ \cdots P[w_{L4}] R[f_3 + f_4] Q\left[-\frac{1}{f_3}\right] P\left[w_{L3}\right] R[f_3] E(x). \end{aligned} \tag{3.15}$$

Brackets on the operators have been suppressed for neatness. w_{L3} and w_{L4} are the radii of lenses L3 and L4, respectively. The focal lengths of L3 and L4 are f_3 and f_4, respectively. The thickness and refractive index of the 50/50 beamsplitter just before the SLM are $t_{50/50}$ and $n_{50/50}$, respectively. The distance between L4 and the 50/50 beamsplitter is l_1, and the phase object on the SLM is ϕ_{bars}. Because the classical field is a beam as it propagates to the SLM, the effect of apertures in the optical system are largely insignificant on its propagation. For this reason, the reference field is recombined with the field that interacted with the SLM at the pupil between the first 50/50 beamsplitter and L3. The propagation of the field back through the telescope consisting of lenses L3 and L4 is accomplished by applying the operators in Eq. (3.15) in reverse order. The propagation from the pupil to the camera is described by,

$$
\begin{aligned}
E_{EMCCD}(x) = R[f_6]Q\left[-\frac{1}{f_6}\right]P[w_{L6}]R[f_6]P\left[\frac{d_{app}}{2}\right]\cdots \\
\cdots R[f_5]Q\left[-\frac{1}{f_5}\right]P[w_{L5}]R\left[f_5-\frac{t_{50/50}\sqrt{2}}{n_{50/50}}-l_2\right]\cdots \\
\cdots R\left[\frac{t_{50/50}\sqrt{2}}{n_{50/50}}\right]R[l_2]\left[E(x)+E_{SLM,2}(x)\right]. \qquad (3.16)
\end{aligned}
$$

In Eq. (3.16), $E_{SLM,2}(x)$ is the field at the pupil after back-reflecting from the SLM through the telescope formed by L3 and L4. The focal lengths of lens L5 and L6 are f_5 and f_6, respectively, and their radii are w_{L5} and w_{L6}. l_2 is the distance between the the pupil and the 50/50 beamsplitter. An adjustable slit placed f_2 after L5 acts as a spatial filter, limiting the angular spectrum that can pass to the EMCCD. Its width is d_{app} in Eq. (3.16).

In the simulation of the quantum experiment, the two-photon state is propagated through the optical system with the operators in Eqs. (3.11 – 3.14) acting on the signal and idler spaces individually. Thus, the propagation is very similar to the classical propagation shown in Eqs. (3.15) and (3.16), but for every classical operator, the are two operators applied to the two-photon state, one for the signal and one for the idler. This results in rather lengthy expressions for the propagation of the two-photon state, so the two-photon propagation expressions will not be listed here. After propagating the two-photon state, the marginal distribution for the signal photon was calculated to form the results in the "quantum" column of Fig. 3.4(c).

Like the experimental results, the simulation shows that the three bars are clearly resolved for all of the three spatial frequencies used. Furthermore, the simulation also reproduces the decrease in visibility for the quantum experimental data at a spatial frequency of 13.3 lp/mm. The classical simulation ("classical" column, Fig. 3.4(c)) reproduces the loss of resolution in the classical experiment for both the 10 lp/mm and 13.3 lp/mm data, whereby the three bars are only resolved as two bars. Quantum phase-shifting holography achieves a greater resolution than classical phase-shifting holography because the two-photon field created in SPDC has a larger spatial bandwidth than the laser beam used in the classical experiment [86]. The spatial bandwidth of SPDC is primarily controlled by the length of the nonlinear crystal and can be evaluated by considering the marginal of $|\psi_0(\boldsymbol{\kappa}_s, \boldsymbol{\kappa}_i)|^2$. Because the phase object is probed with spatially broadband light in the quantum experiment, more high spatial frequency content passes through the bandwidth-limiting aperture. This effect is similar in origin to the increase in spatial resolution granted by structured-illumination microscopy [90].

3.4.3 Pictorial Explanation of Quantum Resolution Enhancement

For the purpose of demonstration, an intuitive explanation of the resolution difference between classical and quantum illumination is shown in Fig. 3.5. Because collimated Gaussian laser beams have a fairly flat wavefront, the laser used for the classical phase imaging experiment is represented by a single ray in Fig. 3.5(a). A phase grating like the one used in the resolution measurement of Fig. 3.4 will cause a beam passing through it to develop diffrative orders around the incident zeroeth order beam (+1 and -1 in Fig. 3.5(a)). Generally, a phase grating will produce higher diffractive orders, but only the +1 and -1 orders are shown in Fig. 3.5(a). If an aperture is placed after the phase grating, its width can be adjusted so that the +1 and -1 diffractive orders are blocked, limiting the angular spectrum of the field that passes through the aperture. Thus, the field that passes through the aperture will not reproduce the image of the phase grating when interfered with a reference field.

The result is different if the phase grating is imaged with light that has a large angular spectrum, such as the signal and idler fields created in SPDC. Figure 3.5(b) shows one

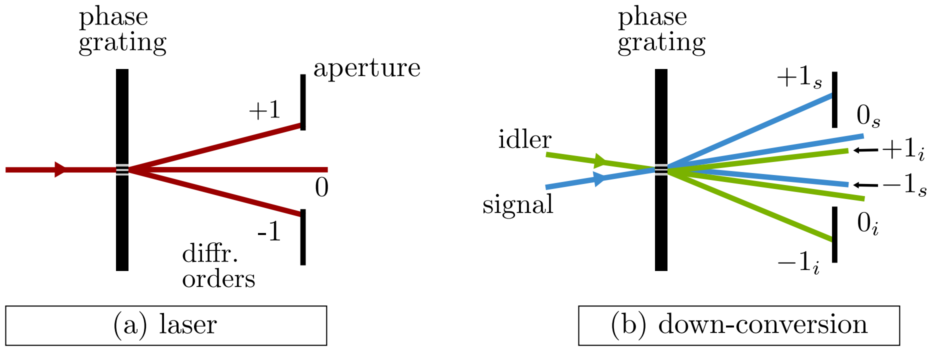

Figure 3.5: An intuitive picture of the resolution limit of (a) a laser beam interacting with a phase grating and (b) signal and idler photons produced from SPDC interacting with a phase grating.

such instance of imaging the same phase grating used in Fig. 3.5(a) with a signal and idler produced is SPDC. The angle of the incident signal and idler photons is not necessarily chosen according to an actual experiment, but it is assumed that they represent the maximum of the output angular spectrum of SPDC. The same spatial bandwidth-limiting aperture used in Fig. 3.5(a) is shown in Fig. 3.5(b). Notice that the +1 and -1 diffractive orders are now encoded on a higher spatial carrier frequency since the input signal and idler photons have a higher spatial frequency than the laser used in Fig. 3.5(a). Furthermore, because of the high angular correlation of the signal and idler, their angles of incidence on the phase grating are equal in magnitude but have an opposite sign. For this reason and because of the greater than zero absolute incidence angles of the signal and idler photons, the 0_s, -1_s, 0_i, and $+1_i$ diffractive orders pass through the aperture. As a result, the signal and idler fields that pass through the aperture will produce the image of the phase grating when interfered with a reference signal and idler field derived from another (or the same) nonlinear crystal pumped coherently.

3.4.4 Graphical Explanation of Quantum Resolution Enhancement

To provide a more quantitative demonstration of the resolution enhancement granted by spatially broadband illumination, the experiments in Fig. 3.1 are simulated with a phase

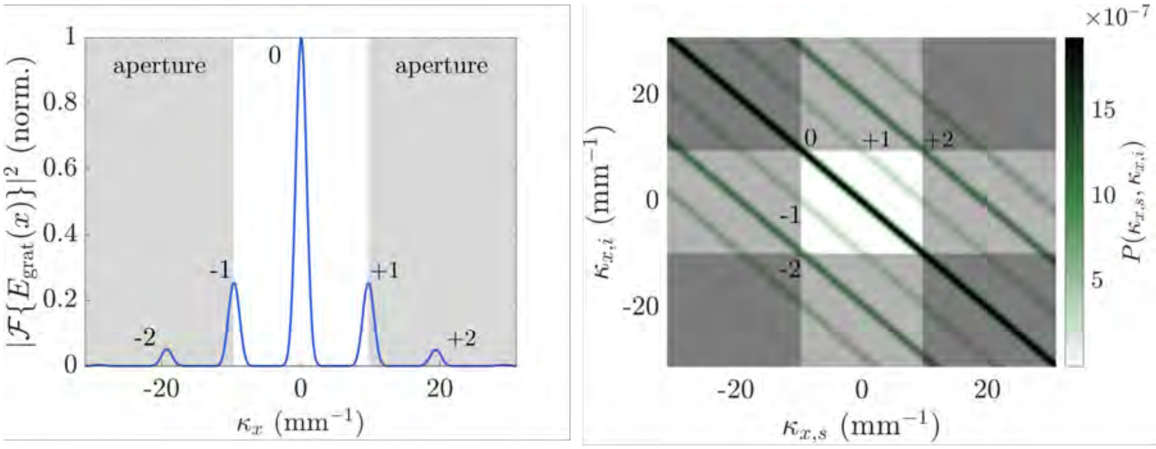

(a) classical angular spectrum (b) two-photon angular spectrum

Figure 3.6: A comparison of the effect of an aperture placed in the Fourier plane of (a) the classical interference pattern and (b) the quantum interference pattern formed by the phase object in Eq. 3.17 and a reference field. Diffractive orders of the classical and quantum interference patterns are labeled as -2, -1, 0, +1, and +2, accordingly. The width of the aperture, grey overlayed on the plots in (a) and (b), is the same in both the classical and quantum experiments. (a) The aperture blocks all but the zeroth and half the -1 and +1 diffractive orders in the classical experiment. (b) In the quantum experiment the -1, 0, +1, and half the -2 and +2 diffractive orders pass through the aperture due to the wide spatial bandwidth of the signal and idler photons.

object of the form:

$$\phi_{\text{obj}}(x) = \exp\left[i\frac{\pi}{2}\left(1 + \cos\left[k_{\text{grat}}x\right]\right)\right] \tag{3.17}$$

In the simulation, $k_{\text{grat}} = 2\pi/1.95\ \text{mm}^{-1}$. The simulation is stopped 12.5 cm after lens L5, where the angular spectrum is mapped to position according to $\boldsymbol{\kappa} = k\boldsymbol{\xi}/f$, where f is the focal length of the lens and $\boldsymbol{\xi}$ is the position in the focal plane of the lens. For simplicity, only one spatial dimension is considered. Figure 3.6 shows the result of the simulation. The angular spectrum of the classical field is shown in Fig. 3.6(a), where,

$$E_{\text{grat}}(x) \propto E(x)\left(1 + e^{i\phi_{\text{obj}}(x)}\right) \tag{3.18}$$

In the simulation, the input classical field, $E(x)$, is a collimated Gaussian beam of radius 3 mm at the SLM. It is worth noting that the phase in Eq. (3.17) is the phase in the SLM plane.

The field in the SLM plane is demagnified by a factor of 0.3 before passing through lens L5. Thus, the spacing between the diffractive orders in the Fourier domain is three times greater than $k_{\text{grat}} = 2\pi/1.95\ \text{mm}^{-1}$. The grey area of the plot in Fig. 3.6(a) indicates spatial frequencies that would be blocked by an on-axis aperture of width $6k_{\text{grat}}$ placed 12.5 cm behind lens L5. As indicated by the figure, this aperture would block half the -1 and +1 diffractive orders and higher diffractive orders.

The two-photon angular spectrum resulting from a simulation of the quantum experiment is shown in Fig. 3.6(b). The same aperture shown in Fig. 3.6(a) is overlayed on the signal and idler spaces in grey in Fig. 3.6(b). The first three diffractive orders for particular input signal and idler spatial frequencies (namely, $\kappa_{x,i} = -\kappa_{x,s} = 3k_{\text{grat}}$) are labeled. Note that the 0, +1, and half the +2 diffractive orders of the signal photon and the 0, -1, and half the -2 diffractive orders of the idler photon pass through the aperture for these particular illumination spatial frequencies. By the symmetry of the two-photon angular spectrum in Fig. 3.6(b), the 0, +1, and half the +2 diffractive orders of the *idler* photon and the 0, -1, and half the -2 diffractive orders of the *signal* photon pass through the aperture for illumination spatial frequencies of $\kappa_{x,i} = -\kappa_{x,s} = -3k_{\text{grat}}$. Thus, the quantum experiment achieves twice the resolution of the classical experiment by virtue of the fact that signal and idler photons have a wider spatial bandwidth than the laser used to illuminate the phase object in the the classical experiment. This is the same effect described in Fig. 3.5, but shown quantitatively in the simulated classical angular spectrum and two-photon angular spectrum of the experiments in Fig. 3.1. It is worth pointing out that the power of each diffractive order passing through the aperture in Fig. 3.6(b) will not be the same because the aperture will always pass more of the lower diffractive orders than the higher diffractive orders over the entire angular spectrum of the illumination source.

The intuitive diagram shown in Fig. 3.5 and the simulation plots shown in Fig. 3.6 allow one to form a mental picture of the physical origin behind the resolution enhancement provided by imaging with spatially broadband light. However, a very simple analytical expression for the mechanism behind this resolution enhancement can be obtained from basic Fourier Optics principles [91]. The derivation of this expression is summarized here.

Individually, the signal and idler photons produced in SPDC can be characterized as having a low degree of spatial coherence in the output plane of the nonlinear crystal that created them [92]. Under the assumption that fields at different points in the illumination source are statistically uncorrelated, it can be shown that the imaging system follows an intensity impulse response [93]:

$$I_{\mathrm{img}}(x,y) = \iint_{-\infty}^{\infty} |h(\xi - x, \eta - y)|^2 I_{\mathrm{obj}}(\xi,\eta)\, d\xi\, d\eta, \tag{3.19}$$

where $I_{\mathrm{obj}}(\xi,\eta)$ is the intensity in the object plane as a function of the object spatial coordinates ξ and η. The intensity in the image plane is I_{img}. The point-spread function for coherent imaging, or impulse response, is given by $h(x,y)$. It is defined as the inverse Fourier transform of the amplitude transfer function, $H(\kappa_x,\kappa_y)$,

$$h(x,y) = \mathcal{F}^{-1}\left\{H(\kappa_x,\kappa_y)\right\}. \tag{3.20}$$

The amplitude transfer function is simply the spatial profile of the bandwidth limiting aperture of the optical system, i.e. the exit pupil. Thus, using the convolution theorem of Fourier analysis, the angular spectrum of the image intensity under incoherent illumination is,

$$\mathcal{F}\left\{I_{\mathrm{img}}\right\} = H_{incoh}(\kappa_x,\kappa_y)\mathcal{F}\left\{I_{\mathrm{obj}}\right\}, \tag{3.21}$$

where $H_{incoh}(\kappa_x,\kappa_y)$ is the optical transfer function of the system. Using the autocorrelation theorem of Fourier analysis, it is immediately apparent that,

$$H_{incoh}(\kappa_x, \kappa_y) = H(\kappa_x, \kappa_y) * H(\kappa_x, \kappa_y). \tag{3.22}$$

For an amplitude transfer function that is a rectangular function, like that used in the experiments of Fig. 3.1, $\mathcal{H}$ is a triangular function of twice the width as the rectangular aperture. Thus, the resolution of the quantum experiment is twice that of the classical experiment. However, because the optical transfer function is a triangular function, the angular spectrum of the object is attenuated linearly as a function of the spatial frequency. This is the reason for the loss of visibility associated with the quantum results in Fig. 3.4 at 13.3 lp/mm.

In view of Fig. 3.6, it is natural to wonder why only a factor of 1.7 in resolution enhancement was observed in the experiment of Fig. 3.4. The reason a factor of two in resolution enhancement was not observed in Fig. 3.4 is that the resolution of the SLM used to make the phase object limited the maximum spatial frequency of the bars that could be used. At the maximum lp/mm used for the three bars in Fig. 3.4 (13.3 lp/mm) the width of each bar was three pixels on the SLM. At two pixels per bar, cross-talk between the pixels prevented the formation of clear three-bar object. In principle, the slit used to limit the bandwidth of the system could be adjusted to a smaller width and larger bars could have been used. However, the ratio of spontaneous emission from the pump to SPDC light passing through the slit prohibited the formation of a clear image in this case.

3.5 Conclusion

In this chapter, a phase-shifting holography method that relies upon the indistiguishability between photons produced in successive down-conversion events in a nonlinear crystal was demonstrated. When compared to classical phase-shifting holography, this method achieves twice the phase shift and ~ 1.7 times the resolution, in agreement with numerical simulation. By doubling the phase shift imparted to light interacting with a phase-only object, it was shown that it is possible to obtain half the fractional uncertainty in a measurement of the phase imparted by that object. This increase in signal-to-noise has a clear benefit in low-light imaging of light sensitive samples, which typically suffers from background noise being of nearly the same intensity as the signal. At the same time, this phase-shifting holography method avoids coincidence imaging, which can require data collection times on the order of tens of hours. Only ten seconds were required to collect all the data to construct the phase object in Fig. 3.3, which is much closer to the relevant time scale of biological imaging. Implementing the quantum phase-shifting holography technique in high numerical aperture imaging systems will require careful phase stabilization. Additionally, samples thicker than the biphoton birth zone in the nonlinear crystal or those with multiple scattering layers will produce a degraded phase image. It may be possible to achieve a higher spatial resolution by imaging the signal and idler photons in coincidence because the effective aperture experienced by the coincidence image is a convolution of the apertures for the individual signal and idler photons [88]. Furthermore, this scheme may be fundamentally more phase sensitive than classical phase-shifting holography due to the Heisenberg scaling of phase uncertainty [94], and future work would involve testing this feature. Furthermore, non-degenerate SPDC, where the signal and idler photons are different wavelengths, may allow for more sophisticated quantum-enhanced phase imaging techniques.

4. Beam Breakup with Polarization-Structured Beams

4.1 Introduction

Physical systems governed by wave mechanics are capable of evolving into configurations that concentrate energy into small regions of space. In optics, the concentration of nearly-parallel rays corresponding to different wavefronts into a small area is known as caustic formation [1, 2, 95, 96]. A familiar example of this behavior is the pattern of light formed on the bottom of a swimming pool caused by refraction from small waves on the water surface. Caustics have also been observed in the phase space trajectories of a driven two-level atomic system [97]. Caustic formation is a fundamentally linear phenomenon arising from the diffraction of light fields containing random phase perturbations [1, 2]. However, nonlinear self-phase modulation can enhance the formation of caustics from small initial phase perturbations [12, 98] or from a completely smooth beam [99] through counter-self-deflection [100]. In addition to caustic enhancement, self-action effects are responsible for the breakup of laser beams into small-scale filaments [101], the formation of nondiffracting beams known as spatial solitons [102–104], and the creation of optical phase singularities [105, 106]. The dynamical equations governing the motion of ocean waves also contain a self-phase modulation term that leads to the formation of rogue waves [107].

Optical communications [108], remote sensing, and lightning strike control [6, 7, 109, 110] are a few technologies that rely upon a careful understanding of the interplay between linear and nonlinear propagation effects. Encoding information in the orbital angular momentum (OAM) of light is a promising way to increase the information capacity of optical communication channels [111–114]. However, the amplification of azimuthal modulation instabilities cause OAM beams to break up during nonlinear propagation [16, 17, 115]. Beams carrying a space-varying polarization have been suggested as an alternative encoding scheme [116] that follows an algebra similar to the Poincaré sphere formalism for plane wave polarization [117]. Such beams are typically referred to as polarization-structured beams. As an added benefit, certain polarization-structured beams form the normal-mode basis of optical fiber waveguides [14, 117, 118].

Polarization-structured beams are solutions to the vector paraxial wave equation and can be categorized by the number of polarization states represented in their cross section. Radially, azimuthally, and spiral polarized beams, typically called *vector vortex* beams [119], trace a path on the Poincaré sphere, parameterized by the azimuthal angle in the beam's cross-section. Figure 4.1 shows an example of a radially polarized beam and the path it traces on the Poincaré sphere for various azimuthal angles in its transverse cross-section. Another class of beams, known as *full-Poincaré* beams, sweep out the entire surface area of the Poincaré sphere, parameterized by both the radial and azimuthal location in the beam [120]. Examples of full-Poincaré beams include *lemon*, *star*, and *monstar* topologies [121]. Figure 4.2 shows the polarization and intensity structure of the lemon and star full-Poincaré beams as well as their Poincaré sphere coverage. There is a final class of beams involving partially polarized light, referred to here as *volumetrically-full Poincaré* beams, that sweep out the entire volume of the Poincaré sphere, parameterized by radial, azimuthal, and axial position in the beam [122]. Volumetrically-full Poincaré beams will be the subject of Chap. 5.

Recent theoretical [15] and experimental [13] results have shown that vector vortex and

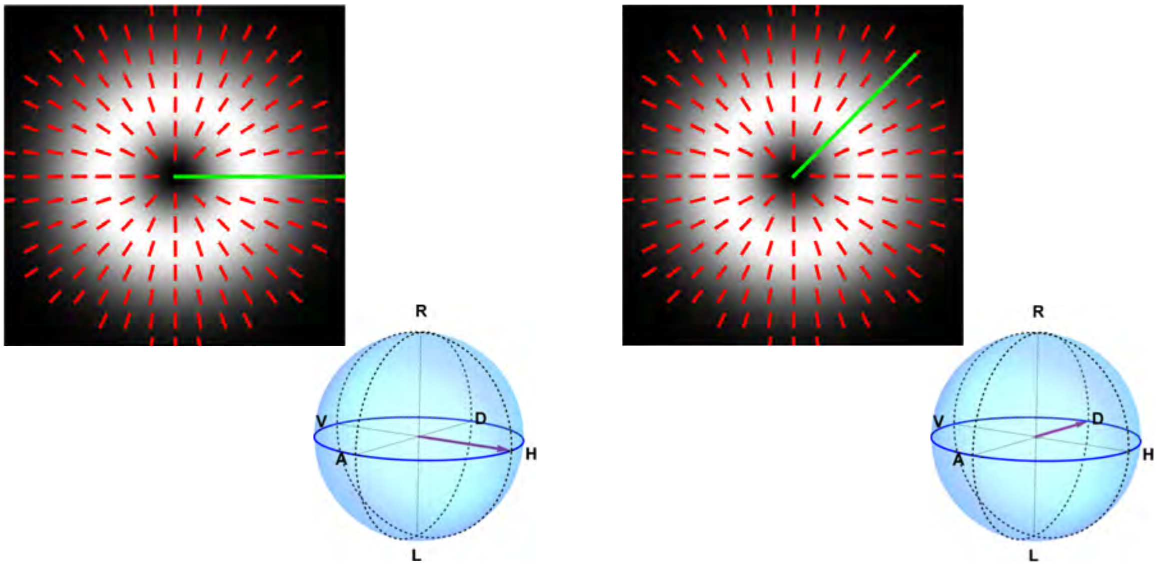
(a) 0 rad

(b) $\pi/4$ rad

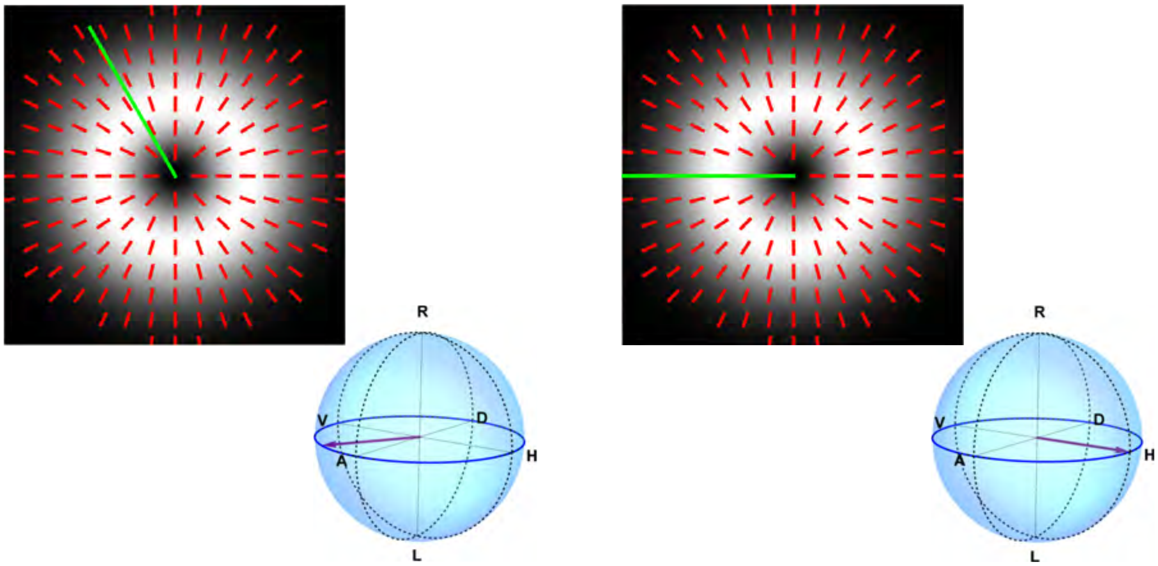
(c) $2\pi/3$ rad

(d) π rad

Figure 4.1: An example of a radially polarized vector vortex beam and the path (blue line on sphere) it forms on the Poincaré sphere for azimuthal angles of (a) 0 rad, (b) $\pi/4$ rad, (c) $2\pi/3$ rad, and (d) π rad in its cross-section (green line in beam profile). R and L represent right- and left- circular polarization states. Similarly, H and V represent horizontal and vertical polarization, and D and A represent diagonal and antidiagonal polarization. The purple arrow in the Poincaré sphere indicates the position along the path for a given azimuthal angle. Red lines overlayed on the beam profile represent the local polarization.

full-Poincaré beams are less prone to self-focusing and nonlinear beam breakup, with full Poincaré beams being the most resistant. Full-Poincaré beams are also less prone to linear beam breakup caused by atmospheric turbulence [123]. Conversely, certain polarization-structured beams formed from Hermite-Gauss modes are more susceptible to nonlinear collapse but in a predictable way that is stable against random phase modulations [124, 125]. These beams, sometimes referred to as hybrid vector beams, are the polarization-structured analog of necklace beams [126], which are known to have stable propagation in nonlinear self-focusing media.

In this chapter, it is shown through both experiment and simulation that full-Poincaré beams are less likely to develop caustics upon nonlinear propagation compared to a uniformly polarized Gaussian beam and to a uniformly polarized beam with the same intensity structure as full-Poincaré beams. This suppression of nonlinear caustic formation is studied in a saturable, nonlinear self-focusing medium. These findings add to the growing understanding of rogue phenomena and are the first to address nonlinear caustic formation in polarization-structured beams.

4.2 Background

4.2.1 Polarization-Structured Beams

Fully coherent polarization-structured beams can be decomposed into a superposition of orthogonally-polarized transverse spatial modes,

$$\mathbf{E}(\rho, \phi, \mathrm{z}, \mathrm{t}) = [E_a(\rho, \phi, z)\mathbf{e}_a + E_b(\rho, \phi, z)\mathbf{e}_b]\, \mathrm{e}^{-i\omega t}, \tag{4.1}$$

where $\mathbf{e}_a$ and $\mathbf{e}_b$ are (generally complex) orthogonal unit vectors. The inseparability of polarization and spatial mode in Eq. (4.1) has been the subject of investigations and debate

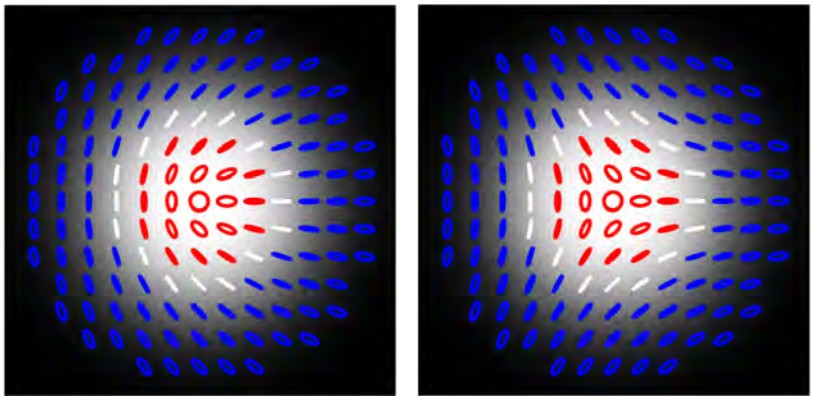

(a) lemon beam

(b) star beam

(c) Poincaré sphere coverage

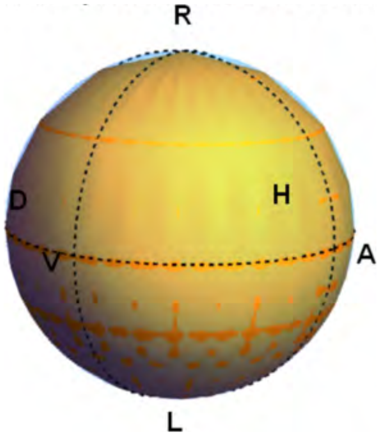

Figure 4.2: (a) A full-Poincaré lemon beam and (b) a full-Poincaré star beam. Red ellipses represent left-circular polarization, and blue represents right-circular polarization. White lines on the beam profile represent linear polarization. The line of linear polarization around the center of the lemon and star beams is known as an l-line. The point of perfect circular polarization at the center of the beam is known as a c-point. (c) The polarization states present in the lemon and star beams form a shell (gold) on the surface of the Poincaré sphere. In principle, this shell includes all states of full polarization, but only if the transverse extent of the beam is allowed to extend to infinity.

about its connection with measures of quantum entanglement [127, 128], though it describes a purely classical beam. Because the orthogonally polarized modes in Eq. (4.1) do not interfere with each other, some have suggested this as the reason for polarization-structured beams' stability against beam breakup [123, 129]. For lemon and star beams, E_a and E_b are the Laguerre-Gauss modes $\mathrm{LG}_{0,0}(\rho, \phi, \mathrm{z})$ and $\mathrm{LG}_{0,\pm1}(\rho, \phi, \mathrm{z})$, respectively. The first subscript in $\mathrm{LG}_{p,l}$ denotes the radial index and the second denotes the azimuthal index. Lemon and star beams are differentiated by the azimuthal index of the mode E_b, with a lemon beam having $l = +1$ and a star beam having $l = -1$.

4.2.2 Nonlinear Propagation

The nonlinear propagation of beams described by Eq. (4.1) can be modeled using coupled-mode Helmholtz equations [101, 130, 131],

$$\begin{aligned} \nabla^2 E_a &= -k_0^2 \left(1 + \chi_a\right) E_a \\ \nabla^2 E_b &= -k_0^2 \left(1 + \chi_b\right) E_b, \end{aligned} \tag{4.2}$$

where

$$\chi_i = \chi^{(1)} + \frac{8 n_0 \epsilon_0 c n_2}{3} \frac{|E_i|^2 + \mu |E_j|^2}{1 + \sigma \left(|E_i|^2 + \mu |E_j|^2\right)}, \tag{4.3}$$

for $i \neq j$. In Eqs. (4.2) and (4.3), k_0 is the free-space wave number, $\chi^{(1)}$ is the linear susceptibility, n_0 is the linear refractive index, and n_2 is the intensity-dependent refractive index. Equation (4.3) is a commonly used phenomenological model of cross-phase modulation in a saturable medium [13, 124, 132, 133]. The cross-coupling coefficient, μ, varies depending upon the nonlinear material under consideration. For atomic vapor nonlinearity, the specific atomic level system under consideration dictates the value of μ [134] and can even lead to the arrest of self-focusing under conditions of coherent population trapping [135]. The linear susceptibility and refractive index can be estimated from the full susceptibility for a two-level atomic system in the steady state, given by the following well-known expression [101]:

$$\chi = \left[N \left(\rho_{bb} - \rho_{aa}\right)^{(eq)} |\mu_{ab}|^2 \frac{T_2}{\epsilon_0 \hbar} \right] \frac{\Delta T_2 - i}{1 + \Delta^2 T_2^2 + \Omega^2 T_1 T_2}. \tag{4.4}$$

In Eq. 4.4, μ_{ab} is the dipole moment of the atomic transition under consideration, T_1 is the natural spontaneous emission lifetime, T_2 is the dipole dephasing time, $\Delta = \omega - \omega_{\mathrm{ab}}$ is the angular frequency detuning from line center, ω_{ab}, and N is the atomic number density. The on-resonance Rabi frequency, Ω, is given by the expression $\Omega = 2|\mu_{ab}||E|/\hbar$, and it describes the strength of the interaction. The equilibrium population density, $(\rho_{bb} - \rho_{aa})^{(eq)}$, is typically assumed to be -1.

In order to account for Doppler broadening of the susceptibility, it is necessary to convolve the full-susceptibility model (Eq. 4.4) with a Gaussian distribution of angular frequencies [136]:

$$g(\omega) = \frac{1}{\sigma_{\mathrm{dopp}} \sqrt{\pi}} \mathrm{e}^{-\left(\frac{\omega}{\sigma_{\mathrm{dopp}}}\right)^2}, \tag{4.5}$$

where $\sigma_{\mathrm{dopp}} = \omega_0 u / c$ with $u = \sqrt{2 k_B T / m}$. ω_0 is the angular frequency of the laser beam interacting with the Rb atoms. T is the temperature of the atomic vapor, and m is the mass of a Rb atom. Thus, the susceptibility takes the form,

$$\chi_{\mathrm{Dopp}}(\omega) = \int g(\omega') \chi(\omega - \omega') d\omega' \tag{4.6}$$

The saturation coefficient, σ, is proportional to the inverse of the saturation intensity. The theoretical value of σ for a two-level atomic system can be used to estimate its value in experiment [101]:

$$\sigma(\Delta) = \frac{\hbar^2}{4|\mu_{ab}|^2 T_1 T_2} \left(1 + \Delta^2 T_2^2\right) \tag{4.7}$$

The intensity-dependent refractive index coefficient, n_2, is estimated by taking the low-intensity limit of the Doppler-broadened index of refraction for a two-level atom [137, 138]:

$$n_2 = \frac{4\pi^{7/2}}{3}\frac{\mu_{ab}^4 N}{c\epsilon_0^2 h^3}\left(\frac{T_2}{k^2u^2}\right)x\mathrm{e}^{-x^2} \tag{4.8}$$

The experimental configuration shown in Fig. 4.3 is well described by $n_0 = 1 - 6\times10^{-5}$, $n_2 = 1.5\times10^{-10}\ \mathrm{m}^2/\mathrm{W}$ [138], $\mu = 0.3$, and $\sigma = 3.9\times10^{-9}\ \mathrm{m}^2/\mathrm{V}^2$. All values except μ and σ were obtained by considering the particular two-level transition described in Fig. 4.3 [101, 139]. μ and σ were obtained by qualitatively matching the simulation of Eq. 4.2 with experiment results. From the right-hand-side of Eqs. (4.2) and (4.3) it is clear that the refractive index experienced by one mode is influenced by the intensity profile of the other mode. The resulting cross-coupling behavior [140] leads to the modification of the self-focusing distance of the composite beam, as mentioned in Refs. [15, 124, 125]. In the absence of cross-coupling ($\mu = 0$), the intensity-dependent susceptibility on the right-hand-side of Eqs. (4.2) leads to the enhancement of caustic formation through self-focusing [12, 98]. This effect is the result of small phase perturbations being amplified through a four-wave mixing process in the nonlinear medium [101].

4.2.3 Intensity Statistics of Beam Breakup

The spatially-resolved intensity statistics of beams undergoing breakup can be modeled by the following probability density function [98],

$$p(I) = N\mathrm{e}^{-\zeta\left(\frac{I}{\langle I\rangle}\right)^{\gamma}}, \tag{4.9}$$

where N is a normalization coefficient, ζ describes the width of the distribution, γ describes the tails of the distribution, and I is the intensity at each transverse location in the beam.

Brackets denote an average over the transverse spatial coordinates. Fully-developed speckle patterns follow exponential intensity statistics, corresponding to $\gamma = 1$ [141]. Upon the development of caustics, intrabeam intensities will begin to follow a long-tailed distribution, characterized by $0 < \gamma < 1$ [98]. A long-tailed intensity distribution is an indicator of rogue high intensity peaks within the beam, in analogy with rogue ocean waves.

4.3 Experiment

The experimental setup for generating FP beams and measuring caustic formation is shown in Fig. 4.3. To generate FP beams, a narrow linewidth (~ 200 kHz) diagonally polarized Gaussian beam with a radius of ~ 5 mm enters a system of two spatial light modulators (SLM). The first SLM is programmed with a blazed computer-generated hologram (CGH) that encodes an $\mathrm{LG}_{0,1}$ onto a carrier spatial frequency [142] for the horizontally polarized portion of the beam only. The face of the first SLM is imaged onto the second SLM using a $4f$ system, and the polarization of the beam is rotated by 90° so that the second SLM acts only on the portion of the beam that did not interact with the first SLM. The second SLM then uses a CGH to encode an $\mathrm{LG}_{0,0}$ onto a carrier spatial frequency that exactly overlaps with the $\mathrm{LG}_{0,1}$ created on the first SLM. The radius of the generated beam (~ 1 mm) is approximately five times smaller than the radius of the input Gaussian beam, resulting in minimal influence of the underlying Gaussian structure on the generated beam. This scheme can be configured to generate any fully coherent polarization structured beam within the spatial bandwidth of the SLMs.

The generated beam then travels to a third SLM that imprints the same random phase mask on both polarization components of the beam. To do this, the SLM is divided into two regions, and one region is imaged onto the other using a $4f$ system containing a 90° polarization rotation. Each half of the third SLM contains the same random phase mask

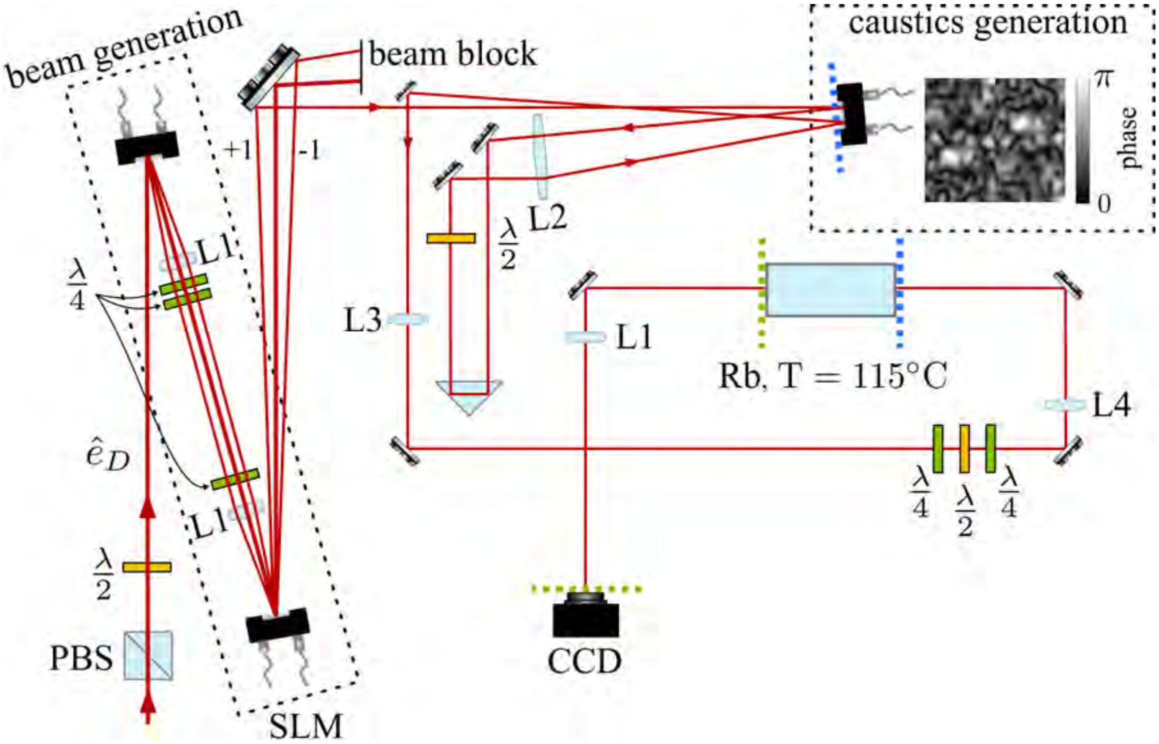

Figure 4.3: The experimental setup for measuring spatially resolved intensity statistics. A diagonally polarized narrow-linewidth laser beam (+0.6 GHz above the ^{87}Rb D$_2$ F = 1 → F′ = 2 transition) enters a system of two spatial light modulators (SLM) capable of generating any fully coherent polarization-structured beam (beam generation). Each SLM acts upon a different orthogonal polarization component of the beam, and the face of the first SLM is imaged onto the face of the second using a $4f$ system. A third SLM divided into two regions, imparts the same spatially random phase to each polarization component of the beam. The face of the third SLM (dotted blue line) is imaged onto the entrance facet of a 7.5 cm-long Rb cell using a Keplerian telescope with a magnification of $-3/4$ (L3 and L4). The polarization is transformed to the circular basis using a series of half- and quarter-wave plates ($\lambda/2$ and $\lambda/4$, respectively). The output facet of the Rb cell (dotted green line) is imaged onto a CCD camera (CCD) to collect pixel intensity statistics. The lens focal lengths are f = 20 cm (L1), f = 30 cm (L2), f = 1 m (L3), f = 75 cm (L4); polarizing beamsplitter (PBS).

up to a reflection about the horizontal and vertical axes to compensate for the coordinate reflection imparted by the intervening $4f$ system. The correlation length of random phase features in the mask is 450 μm, and the maximum phase shift in the mask is π radians. The face of the third SLM is imaged onto the input facet of an anti-reflection-coated Rb vapor cell using a Keplerian telescope with a magnification of $-3/4$, and the polarization of the beam is transformed to the circular basis. Because the two polarization components travel along a common path, they experience a relative optical delay that is negligible compared to their individual coherence lengths ($\sim$477 m). Thus, at the input of the vapor cell, the FP beam has a lemon topology with an overall random phase,

$$\mathbf{E}(\rho, \phi, z) = \mathrm{e}^{i\phi_{\mathrm{rand}}(\rho,\phi,z)} \left[\mathrm{LG}_{0,0}\mathbf{e}_{\mathrm{L}} + \mathrm{LG}_{0,1}\mathbf{e}_{\mathrm{R}}\right] \tag{4.10}$$

The 7.5 cm-long vapor cell contains natural abundance Rb and is heated to 115 °C to achieve a high number density of Rb atoms $\left(\sim 10^{19}\ \mathrm{atoms/m^3}\right)$ in the cell. The laser is blue-detuned to +0.6 GHz above the ^{87}Rb $\mathrm{D_2}$ $\mathrm{F} = 1 \rightarrow \mathrm{F}' = 2$ transition and experiences a self-focusing nonlinearity. At the maximum power used in this experiment (130 mW), the $\mathrm{LG}_{0,0}$ beam experiences a maximum nonlinear phase shift of $\sim 2\pi$ rad. The field at the output facet of the Rb cell is then imaged onto a camera to collect pixel intensity statistics. We investigated scenarios where n_2 was less than zero during the undertaking of this experiment but observed no rogue intensity peaks at any power, consistent with Ref. [143].

4.4 Results

4.4.1 Comparison of Intensity Statistics

Figure 4.4 shows intensity statistics collected for three different beams: a lemon beam (FP), a uniformly polarized beam with the same intensity structure as a lemon beam (FPA), and a

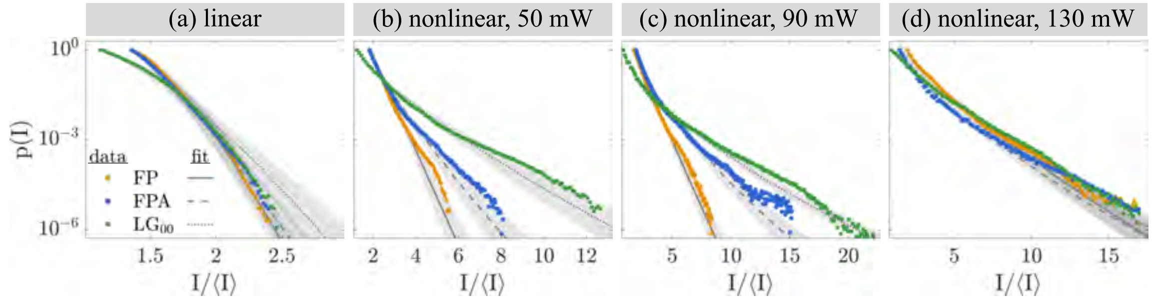

γ(FP)	1.38(9)	1.02(6)	0.96(3)	0.82(2)
γ(FPA)	1.24(8)	0.84(4)	0.72(2)	0.76(2)
γ(LG_{00})	1.4(1)	0.79(3)	0.66(1)	0.87(2)

Figure 4.4: The experimentally obtained intensity statistics of FP (orange diamonds), FPA (blue circles), and $LG_{0,0}$ (green squares) beams after (a) linear and (b,c,d) nonlinear propagation. The solid, dashed, and dotted lines are Eq. (4.9) fitted to the FP, FPA, and $LG_{0,0}$ data, respectively. The value of γ obtained from fitting Eq. (4.9) to each dataset is shown at the bottom of the figure. The shaded area indicates the one standard deviation uncertainty in the fits. Under linear propagation, all beams have very similar intensity statistics that display no caustic formation. Under nonlinear propagation, the uniformly polarized $LG_{0,0}$ and FPA beams begin to display caustic formation that increases with increasing beam power (b and c). For the same beam powers, the polarization-structured FP beam maintains exponential intensity statistics with no caustics present. The suppression of caustics afforded by the polarization structure of the beam is no longer present at a beam power of 130 mW.

uniformly polarized $LG_{0,0}$ beam with the same beam waist as the $LG_{0,0}$ component of the FP beam. Each histogram is comprised of pixel intensities from the imaging camera for 500 trials with different random phase masks. The frames from the camera are truncated to include only pixels within a region that contains nonzero intensity when all frames from the 500 trial collection are averaged together. The frame sizes for the FP and FPA trials are similar, but the frame sizes are smaller for the $LG_{0,0}$ trials–as expected for the smaller $LG_{0,0}$ beam. The pixel intensities are divided by the average intensity observed in all trials. Equation (4.9) is fit to the tails of the histograms using maximum likelihood estimation to measure the “tailiness" of the intensity distribution. Uncertainties in the fits were obtained through Monte Carlo simulation.

When the beam power is low ($\sim$ 4 mW) and the Rb vapor is at room temperature, the beams propagate linearly through the cell, Fig. 4.4(a). Under linear propagation, the FP, FPA, and $LG_{0,0}$ behave almost identically with no caustic formation present, as indicated by $\gamma > 1$. In fact, the beams do not even display speckle pattern statistics under these conditions. In Fig. 4.4(b) the cell temperature is increased to 115 °C and the beam powers are increased to 50 mW. The $LG_{0,0}$ and FPA beams begin to develop long-tailed intensity statistics, $\gamma < 1$, indicating the presence of caustics. Under these same conditions, the FP beam displays speckle-pattern statistics. Thus, the tendency of the beam to display nonlinear caustics is seen to be suppressed through use of a polarization structured beam. As the beam powers are increased to 90 mW, Fig. 4.4(c), the intensity histograms for the $LG_{0,0}$ and FPA beams develop longer tails while the FP beam maintains Gaussian amplitude statistics. At the maximum achievable beam power of our system, 130 mW, all beams display similar long-tailed intensity statistics, Fig. 4.4(d).

The suppression of caustic enhancement in the polarization-structured beam can be attributed to two primary effects. The first is that FP beams can be treated as a mutually incoherent superposition of an $LG_{0,0}$ and an $LG_{0,\pm1}$ beam. This leads to the decrease in linear beam breakup from phase perturbations [123] through an effect known as complementary diffraction, as described in Ref. [129]. The second effect contributing to the suppression of nonlinear caustic formation is the cross-phase modulation between the two modes comprising the FP beam. Mutual interaction can stabilize the beam under nonlinear propagation [13, 15, 132]. The suppression of caustic enhancement afforded by polarization structure does not persist at higher powers, as indicated by the results of Fig. 4.4(d). Furthermore, caustic enhancement also appears to saturate at higher powers because γ has increased for all but the FP beam at 130 mW.

4.4.2 Simulation of Nonlinear Propagation

Figure 4.5 compares the experimentally obtained polarization and intensity structure of the FP beam [Fig. 4.5(a)] to numerical simulation [Fig. 4.5(b)] for both linear and nonlinear propagation after the implementation of a random phase mask. The simulation was performed by numerically solving Eqs. (4.2) using a split-step Fourier method that accounts for nonparaxiality [131] with a beam power of 90 mW. The simulation results display good qualitative agreement with experiment. Under linear propagation, the intensity structure does not change dramatically because the maximum of the random phase mask (π rad) is small compared with that which typically leads to caustics ($\sim 8\pi$ rad)[12]. Remarkably, after nonlinear propagation, the lemon polarization topology of the FP beam changes very little, despite the dramatic change in its intensity structure. This is likely due to the fact that the fields in each circular polarization component of the FP beam experience similar nonlinear phase shifts due to the cross-phase terms in Eqs. 4.2. If the coupling coefficient, μ, were equal to unity, the polarization structure would not change at all because both circular polarization components would experience the exact same nonlinear phase. That is, there would be no nonlinear birefringence [130]. In this case, the polarization structure would be the same for both linear and nonlinear propagation results.

In Fig. 4.5(c) we simulate the intensity statistics of FP, FPA, and $LG_{0,0}$ beam after nonlinear propagation for beam powers of 90 mW. The FP beam is the least likely to develop rogue intensity peaks and the $LG_{0,0}$ is the most likely to develop rogue intensity peaks, in agreement with experiment. Compared with experiment, the FP beam has slightly longer-tailed statistics in simulation. This is likely due to small differences in the intensity structure of the beam in experiment and simulation. Nonetheless, the model of Eqs. (4.2) and (4.3) describe the experimental results quite well.

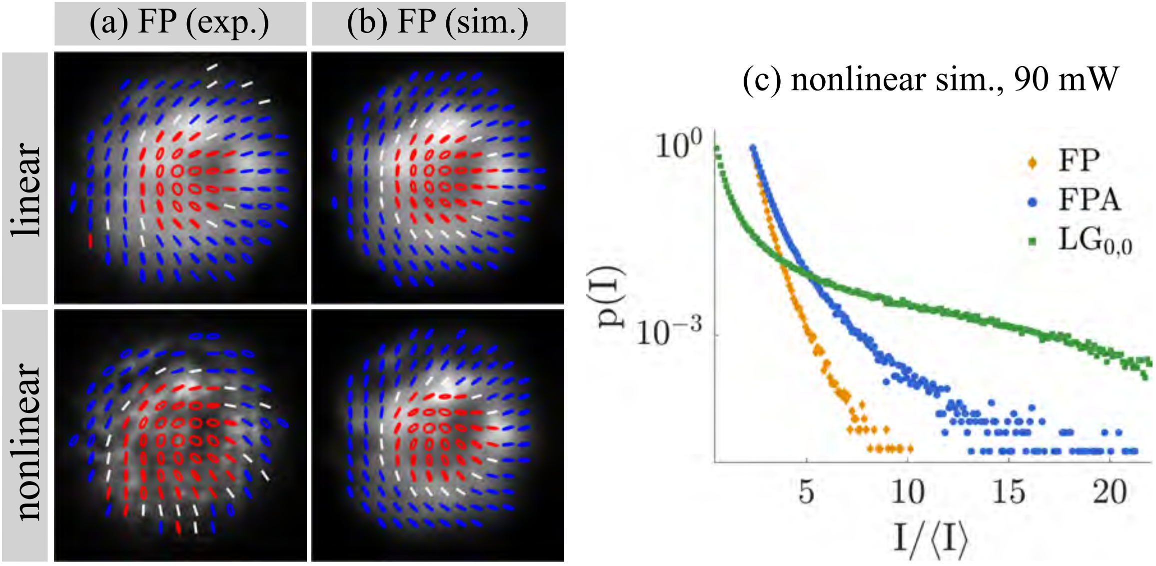

Figure 4.5: Comparison of experimental and simulation results for linear and nonlinear propagation at a beam power of 90 mW. The polarization handedness in (a) and (b) is indicated by color, where red, blue, and white indicate left-circular, right-circular, and linear polarization respectively. The same random phase mask is used in (a) and (b). The intensity structure does not change dramatically after linear propagation because the maximum phase of the phase mask is many times smaller than the maximum phase at which caustics usually develop (~8π rad) (top). However, the intensity structure changes dramatically upon nonlinear propagation over the same distance (bottom). Nonetheless, the polarization structure remains similar to the linear result. The polarimetry simulation (b) shows good qualitative agreement with the experimental results (a). (c) In the numerical simulation of nonlinear propagation with 500 different random phase masks, the FP beam has shorter-tailed statistics than either the FPA or $LG_{0,0}$ beams, in agreement with experiment (Fig. 4.4). The random phase masks used in obtaining (c) have the same parameters as those used in experiment.

4.5 Conclusion

This chapter demonstrated that a full-Poincaré lemon beam is less susceptible to developing caustics upon propagation through a saturable, nonlinear self-focusing medium than either a uniformly polarized beam with the same intensity structure or a uniformly polarized $\mathrm{LG}_{0,0}$ beam with the same waist as the $\mathrm{LG}_{0,0}$ component of the lemon beam. The experiment was simulated by numerically solving coupled-mode Helmholtz equations for a beam propagating through a saturable self-focusing medium, resulting in good agreement with experiment. These results add to the growing understanding of rogue behavior [12, 98], and they bear upon the use of polarization-structured beams to control nonlinear self-focusing processes in remote sensing [6, 7, 109], optical communications [118], and laser engineering [144]. The extent to which polarization structure is maintained during nonlinear self-focusing warrants further study. Such investigations would extend the field of singular optics into the nonlinear domain [121, 145], potentially revealing topologically protected quantities that could be used for information transfer.

5. Generation of volumetrically-full Poincaré beams

5.1 Introduction

Laser beams with spatially-varying amplitude, phase, or polarization beyond that of a uniformly polarized Gaussian beam have garnered a significant amount of attention over the last few decades [146, 147]. These beams are generally referred to as structured light. As shown in the previous chapter and in other studies, polarization-structured beams are a promising candidate for communications and high power applications. Additionally, radially polarized beams can achieve a tighter focus [148], potentially increasing the precision of laser trapping [149] and increasing the resolution in confocal microscopy [150]. Full-Poincaré and vector vortex beams are fully polarized beams with polarization structure. However, other types of polarization-structured beams that include states of partial and full polarization also exist. While fully polarized beams, such as full-Poincaré and vector vortex beams, have been studied extensively, partially polarized beams with polarization structure have not yet generated as much research. Fully polarized beams with polarization structue only contain two mutually incoherent beams, resulting in two-beam coupling effects under nonlinear propagation. This coupling is responsible for the the modification of the critical power of self-focusing, which can lead to an increased resistance to beam breakup [15].

Because partially polarized polarization-structured beams can be comprised of an incoherent superposition of many spatial modes, they may hold promise for further increasing the resistance to beam breakup beyond that of fully polarized polarization-structured beams. One such partially polarized beam that contains every polarization state on the surface and interior of the Poincaré sphere was developed by Beckley et al., referred to here as volumetrically-full Poincaré (VFP) beams [122]. In this chapter, a method of generating polarization-structured beams comprised of at most two temporally incoherent beams of opposite orbital angular momenta or a relative inversion about the horizontal axis is presented. This method is used to generate a VFP beam. The results and methods of this chapter add to the quickly growing field of structured light generation and may have an impact on studies of "classical entanglement" and beam dynamics in complex and nonlinear media.

5.2 Background

A VFP beam is comprised of an incoherent superposition of two FP beams of opposite helicity [122],

$$\mathbf{VFP}(\rho,\theta,z) = a_1\mathbf{FP}_+(\rho,\theta,z) + a_2\mathbf{FP}_-(\rho,\theta,z), \tag{5.1}$$

where,

$$\mathbf{FP}_\pm(\rho,\theta,z) = \mathrm{LG}_{0,0}(\rho,\theta,z)\boldsymbol{e}_\mathrm{L} + \mathrm{LG}_{0,\pm1}(\rho,\theta,z)\boldsymbol{e}_\mathrm{R} \tag{5.2}$$

The coefficients a_1 and a_2 in Eq. 5.1 are uncorrelated stocastic variables of equal amplitude. That is, $\langle a_1 a_2^*\rangle = \langle a_2 a_1^*\rangle = 0$ and $\langle |a_1|^2\rangle = \langle |a_2|^2\rangle$, where brackets denote an average over the exposure time of the camera that records the beam profile. For the sake of simplicity, we have ignored any phase difference between the beams on the R.H.S of Eq. 5.2, but such a phase difference would impart a rigid rotation to the polarization structure [120]. The unit vectors $\boldsymbol{e}_\mathrm{L}$ and $\boldsymbol{e}_\mathrm{R}$ denote left- and right-circular polarization, respectively. The Stokes parameters' dependence upon ρ, θ, and z reveal how every polarization state is present at some location in the VFP beam,

$$\begin{aligned}
s_0 &= |\mathrm{LG}_{0,0}|^2 \left[1 + \tilde{\rho}^2\right] \\
\frac{s_1}{s_0} &= \frac{2\tilde{\rho}}{(1 + \tilde{\rho}^2)} \cos\theta \cos\theta_{\mathrm{G}}(z) \\
\frac{s_2}{s_0} &= \frac{-2\tilde{\rho}}{(1 + \tilde{\rho}^2)} \cos\theta \sin\theta_{\mathrm{G}}(z) \\
\frac{s_3}{s_0} &= \frac{\tilde{\rho}^2 - 1}{1 + \tilde{\rho}^2}.
\end{aligned} \tag{5.3}$$

where $\tilde{\rho} = \sqrt{2}\rho/w(z)$, $w(z)$ is the beam radius, and $\theta_{\mathrm{G}}(z)$ is the Gouy phase [151] of the $\mathrm{LG}_{0,0}$ beam. Aside from the dependence upon $\theta_{\mathrm{G}}(z)$, Eqs. 5.3 are the parametric equations of a unit disk in the Poincaré sphere with a normal vector that is perpendicular to the s_3-axis. As the Gouy phase changes, the disk rotates about the s_3-axis, eventually sweeping the entire volume of the Poincaré sphere. Because the Gouy phase depends upon z as $-\arctan(z/z_{\mathrm{R}})$, where z_{R} is the Rayleigh range, half of the disk's rotation occurs within $\pm z_{\mathrm{R}}$. The full π rotation of the disk only occurs for propagation from $z = -\infty$ to $z = +\infty$.

Figure 5.1 shows the Poincaré sphere coverage and transverse polarization structure of the VFP beam at three locations along the beam's propagation: $z = -1.7z_{\mathrm{R}}$, $z = 0$, and $z = 1.7z_{\mathrm{R}}$. In each plane of constant z, there are two regions where the degree of polarization is zero. These correspond to areas where the polarizations of the constituent FP beams are orthogonal. Full polarization occurs in regions where the polarizations of the constituent FP beams are the same. The lack of states at the top of the Poincaré sphere is a result of the finite numerical precision of the VFP beam's representation in the computer coupled with the finite window size chosen in Fig. 5.1. It is worth noting that it is not possible to obtain polarization states at the very top of the Poincaré sphere because perfectly right-circularly polarized states only exist infinitely far from the propagation axis of the beam.

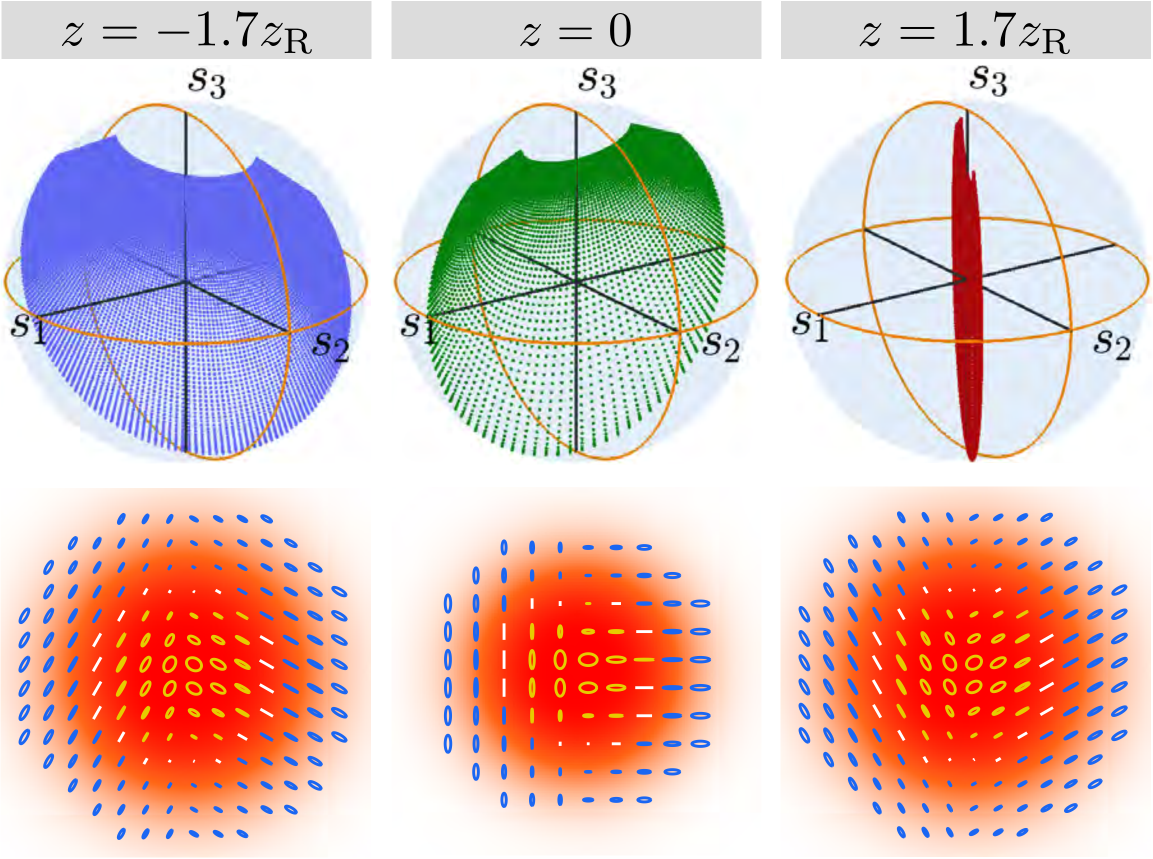

Figure 5.1: Poincaré sphere coverage (top row) and transverse polarization structure (bottom row) of a VFP beam at three positions along the beam's propagation. (top row) As the beam propagates, the polarization states present in the beam form a disk in the Poincaré sphere that rotates about the s_3 axis. (bottom row) The transverse polarization structure of the VFP beam contains varying degrees of polarization, as indicated by the relative size of the polarization ellipse. Upon propagation, the local polarization at a point in the beam undergoes a rotation. Yellow, blue, and white ellipses indicate left-circular, right-circular, and linear polarization, respectively. Beam sizes are scaled differently to aid visual inspection.

5.3 Experiment

The experimental setup for generating a VFP beam is shown in Fig. 5.2. In the "coherence control system" stage, a 780 nm tunable diode laser (Toptica DL pro 780) is coupled into a phase-shifting electro-optic modulator (EOM) (AdvR WPM-K0780-P85P85ALO) via a polarization-maintaining fiber (PMF). The EOM is driven with amplified white noise (noise with equal power at all frequencies) to broaden the linewidth of the laser used to generate the VFP beam. Because the laser has a free-running bandwidth of approximately 200 kHz, one FP beam used to create the VFP beam would have to be delayed by more than 500 m relative to the other in order to create the incoherent superposition of two FP beams necessary for the VFP beam. By decreasing the coherence length (increasing the bandwidth) of the laser, the relative delay distance can be brought down to a more manageable distance. The process of using a phase-only device to broaden the laser linewidth is described below.

5.3.1 Linewidth Broadening with Phase-only Devices

When driven with white noise, the operation of the phase-shifting EOM used in Fig. 5.2 is to add a random phase to the input to the device,

$$E_{\text{noise}}(r,t) = E_{\text{in}}(r,t)\mathrm{e}^{iag_{\text{rand}}(t)}. \tag{5.4}$$

In Eq. (5.4), $g_{\text{rand}}(t)$ is function that varies randomly between $-1/2$ and $1/2$ with time and has a flat spectrum over a given bandwidth. The peak-to-peak amplitude of the random phase shift is dictated by a. The input to the EOM is a single mode fiber, so $E_{\text{in}}(r,t)$ is a CW Gaussian mode. Because the spatial dependence is insignificant for the following treatment, it will be suppressed. Generally, the underlying bandwidth of E_{in} will influence

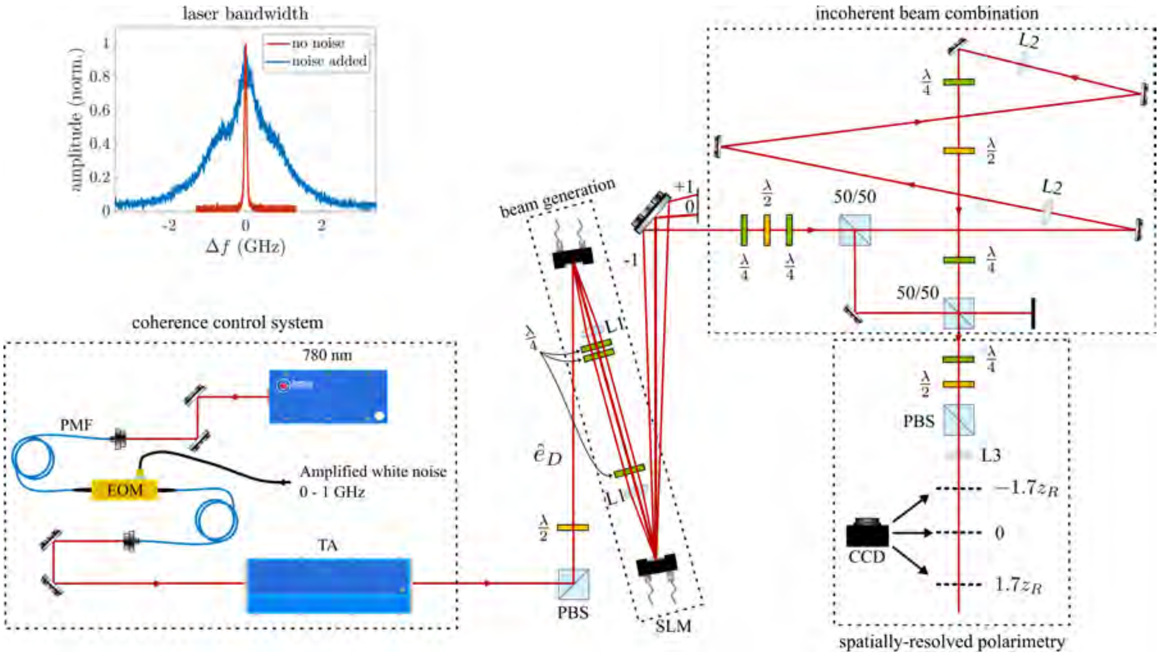

Figure 5.2: Experimental setup for generating a VFP beam. 780 nm: tunable diode laser; PMF: polarization-maintaining fiber; EOM: phase-shifting electro-optic modulator; TA: tapered amplifier; PBS: polarizing beamsplitter; $\lambda/2$: half-wave plate; SLM: spatial light modulator; L1: $f = 20$ cm lens; $\lambda/4$: quarter-wave plate; 50/50: 50/50 beamspliter; L2: $f = 2.5$ m lens; L3: $f = 1$ m lens; CCD: camera.

the bandwidth of E_{noise}. In particular, the bandwidth of E_{noise} is as follows:

$$\mathcal{F}\left\{E_{\text{noise}}\right\} = \mathcal{F}\left\{E_{\text{in}}\right\} * \mathcal{F}\left\{\mathrm{e}^{iag_{\text{rand}}(t)}\right\}, \tag{5.5}$$

which follows directly from the Fourier convolution theorem. For the narrowband laser used in Fig. 5.2, $\mathcal{F}\left\{E_{\text{in}}\right\} \approx \delta(\omega - \omega_0)$, where ω_0 is the central angular frequency of the laser. As a result of the sifting property of the delta function, the spectrum of E_{noise} is centered at ω_0 and dictated by the bandwidth of the added phase noise:

$$\mathcal{F}\left\{E_{\text{noise}}\right\}(\omega_0) \approx \mathcal{F}\left\{\mathrm{e}^{iag_{\text{rand}}(t)}\right\}(\omega_0). \tag{5.6}$$

It is now necessary to choose a value of the peak-to-peak phase shift, a, that will result in E_{noise} having the same bandwidth as g_{rand}. In practice, it is not possible to arrive at an analytical expression for the bandwidth of an arbitrary phase-only signal, but it is very straighforward to obtain the spectrum of E_{noise} from simulation.

Figure 5.3 shows a simulation of the spectrum of Eq. 5.4 for various values of a. For simplicity, it is assumed that $E_{\text{in}}(t) = \exp(-i\omega_0 t)$, where $\omega_0 = 2\pi * 3.84 * 10^{14}$ rad/s. Each spectrum is obtained from an average of 100 different realizations of Eq. (5.4). In each realization, g_{rand} is constructed by creating an array of random numbers and multiplying its spectrum by a rectangular function of width $\omega_0/5$. After transforming the bandwidth-limited signal back to the temporal domain, it is normalized so that varies between $-1/2$ and $1/2$ and is multiplied by a. As the peak-to-peak phase shift imparted by the randomly driven EOM is increased from $a = 2\pi$ to $a = 6.5\pi$ the bandwidth of the light increases. For values of a less than 6.5π, a narrow central peak at ω_0 is present. Interestingly, the bandwidth of E_{noise} depends on a in a nonlinear way. At $a = 6.5\pi$, the random phase noise dominates the bandwidth of E_{noise} rather than the strong central peak at ω_0. For the EOM used in

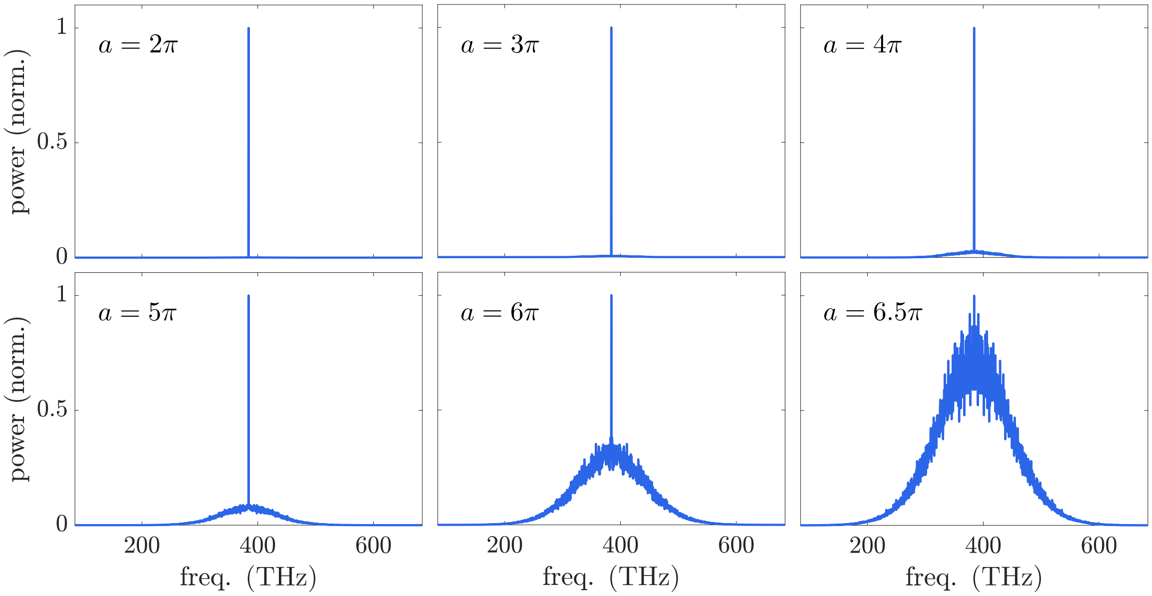

Figure 5.3: The simulated spectrum of a CW beam multiplied by a randomly varying phase. The value of a in the upper left corner of each panel is the peak-to-peak phase shift imparted by the random phase. The central frequency of the CW beam is 384 THz. In each panel, the bandwidth of the noise is 77 THz. For values of a lower than 6.5π, the narrow central peak associated with the underlying carrier beam dominates. However, at $a = 6.5\pi$ the bandwidth of the noise dominates the spectrum.

Fig. 5.2, a phase shift of $\sim 6.5\pi$ can be achieved by driving it with a peak-to-peak voltage corresponding to a power of 39 dBm. The inset plot in the upper left corner of Fig. 5.2 shows the effect of driving the EOM in Fig 5.2 with 1 GHz bandwidth white noise at 39 dBm. Before measuring the spectrum of the light exiting the EOM, the beam is then coupled into a tapered amplifier (TA) with a flat gain profile over the bandwidth of the beam (Toptica BoosTA). The spectrum of the beam is measured after the TA with and without noise (upper-left inset) using a scanning Fabry-Perot interferometer (FPI) (Thorlabs SA210-5B), confirming the broadening of the spectrum to approximately 1 GHz from the added phase noise. With no phase noise added, the measured bandwidth corresponds to the resolution of the FPI (67 MHz). The use of phase-only devices to broaden a laser's linewidth is described in more detail in Ref. [152].

5.3.2 VFP Beam Generation

In the "beam generation" stage of Fig. 5.2, the beam's polarization is rotated to diagonal before reflecting from two spatial light modulators (SLM) with coinciding image planes. Each SLM acts on a different orthogonal linear polarization. The SLMs are programmed with computer-generated holograms [142] such that the beam produced on the -1 diffractive order is $\mathrm{LG}_{0,0}\mathbf{e}_\mathrm{V} + \mathrm{LG}_{0,1}\mathbf{e}_\mathrm{H}$. Because both polarization components traverse the same optical path, this method of beam generation is inherently phase stable. In the "incoherent beam combination" stage, the polarization components of the generated beam are transformed to the circular basis to produce an FP_+ beam with the polarization of the two constituent modes exchanged before the beam is split into two paths by a 50/50 beamsplitter. The transmitted path consists of a 10 m imaging delay line with one extra reflection than the reflected path and a series of quarter-wave and half-wave plates to correct for polarization rotations induced by the dielectric mirrors. The extra reflection of the delayed FP beam reverses it's helicity relative to the beam reflected from the first 50/50 beamsplitter. The two FP beams are then recombined at a second 50/50 beamsplitter. The 10 m freespace delay between the two beams ensure that they combine incoherently since the coherence length of the beams is ~ 95.4 mm. After recombination, the beam travels through a quarter-wave plate, a half-wave plate, a polarizing beamsplitter and an $f = 1$ m lens to perform spatially resolved polarimetry at three longitudinal positions around the beam waist: $z = -1.7z_{\mathrm{R}}$, $z = 0$, and $z = 1.7z_{\mathrm{R}}$.

5.4 Results

Figure 5.4 shows the results of generating a VFP beam with the setup in Fig. 5.2. The experimentally generated VFP beam agrees closely with the ideal theoretical VFP beam shown in Fig. 5.1. Like an ideal VFP beam, the Poincaré sphere coverage is a disk that rotates about the s_3-axis. However, the Poincaré sphere coverage for the experimentally generated VFP beam is a disk with nonzero thickness. The deviation from an ideal thickness of zero is primarily due to the imperfect retardation of the quarter- and half-wave plates that control the polarization. The lack of states near the s_3 pole of the disks can be attributed to finite sensor size and bit depth of the camera. That is to say, pure right-circular polarization is only present far from the center of the beam, where the intensity is low and the edges of the camera sensor are located. The low signal-to-noise ratio far from the center of the beam is responsible for the increased noise present near the s_3 pole. The rotation angle of the disk at each longitudinal position is estimated using maximum likelihood (ML) fitting with the model of a plane containing the s_3-axis and one free parameter describing the angle of the plane relative to the s_1-axis. Monte Carlo simulation was used to determine the uncertainty in the fits. ML fitting returns the following values of the rotation angle for $z = -1.7z_{\mathrm{R}}$, 0, and $1.7z_{\mathrm{R}}$, respectively: $\phi = -44.03(1)^\circ$, $12.03(3)^\circ$, $59.58(1)^\circ$. Ideally, the angle of the disk at

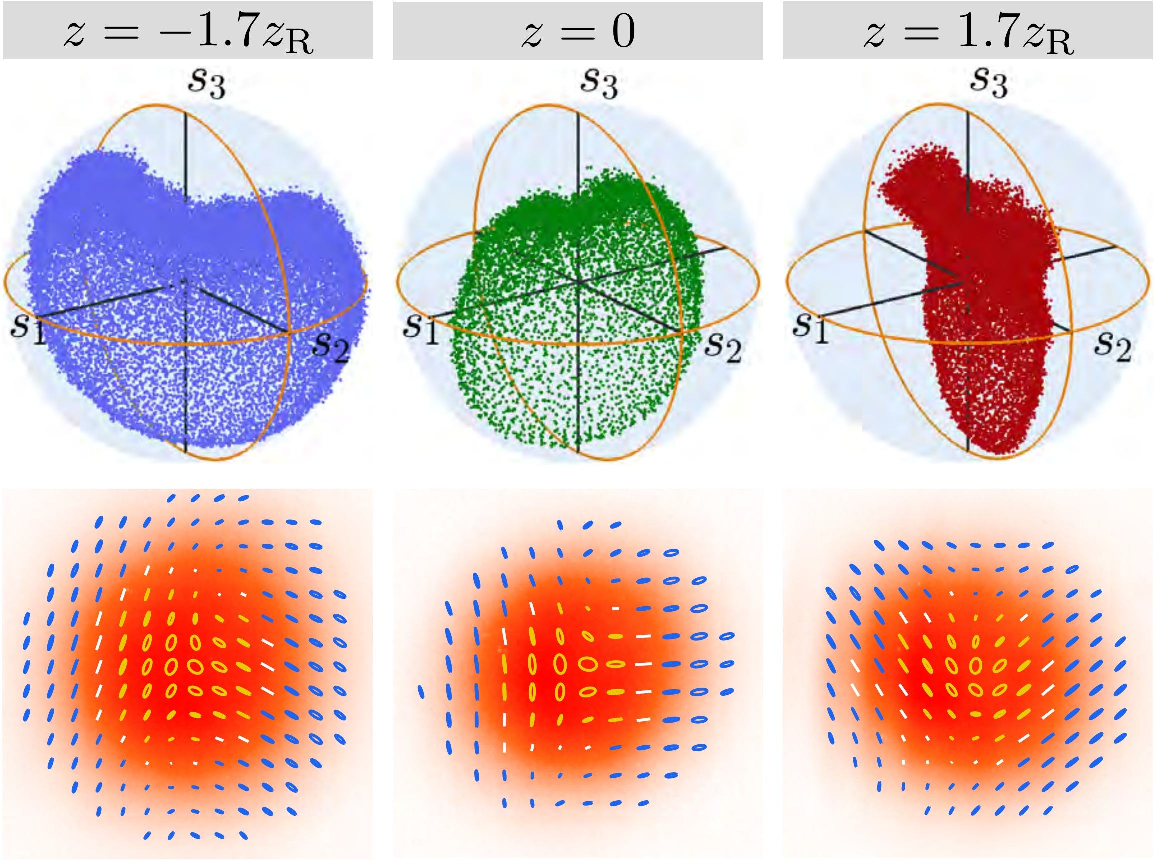

Figure 5.4: Experimentally measured Poincaré sphere coverage (top row) and transverse polarization structure (bottom row) of a VFP beam. Generally, the experimental results are in close agreement with the theoretical results of Fig. 5.1.

$z = -1.7z_R$, 0, and $1.7z$R should be approximately −59.53°, 0°, and 59.53°, respectively. The difference between the ideal VFP beam and the experimental results can be primarily attributed to the waveplates used to control and measure the polarization, as well as the uncertainty in the exact location of the beam waist.

5.5 Conclusion

In conclusion, this chapter has reported an optical system capable of producing fully and partially polarized beams with varying amounts of temporal coherence. Using this system, a volumetrically-full Poincaré beam was generated for the first time to our knowledge. While past reports of VFP beam generation have relied upon the incoherent addition of polarimetry data taken sequentially from two full Poincaré beams of opposite helicity [122], our method produces a VFP beam available in real time. With minimal reconfiguration (amounting to blocking beams), our system can generate any arbitrary fully polarized polarization-structured beam with varying amounts of temporal coherence. Furthermore, this system can be used to generate beams that consist of either a coherent or an incoherent superposition of polarization-structured beams of opposite helicity or a relative inversion about the horizontal axis, though phase stabilization would be necessary for coherent combination. The results of this chapter add a method of generating polarization-structured beams with regions containing varying degrees of polarization to the quickly growing toolbox of structured light generation. Polarization-structured beams like the VFP beam generated in this chapter will continue to advance the fields of imaging, nonlinear optics, and communications.

6. Summary and Outlook

Controlling and characterizing phase distortions in optical systems is an inevitable barrier to advancement in many areas of optics. These phase distortions can take the form of linear and nonlinear phase distortions. Linear phase distortions impact the fields of high resolution imaging, optical communications, and applications involving free-space propagation through the atmosphere, among others. Nonlinear phase distortions can lead to unpredictable beam breakup and caustic generation in areas of physics such as remote atmospheric sensing, lighting-strike control, and directed energy defense systems. By leveraging the strong spatial correlations of entangled photons, this thesis has provided ways to handle linear phase distortions in quantum-enabled modes of imaging. Furthermore, the effects of nonlinear phase distortions were minimized using polarization-structured light.

Chapter 2 presented a new method of aberration correction whereby phase distortions (aberrations) introduced in the path of one entangled photon in an entangled photon pair is cancelled nonlocally by introducing the proper conjugate aberration into the path of its entangled partner photon. The effect of aberrations and their subsequent cancellation on a measurement of transverse entanglement were shown. Furthermore, the extent to which aberration cancellation can be achieved and its dependence on experimental parameters was analyzed, providing limits for this nonlocal aberration cancellation scheme. The results and methods of Chap. 2 add a new *quantum* protocol to the adaptive optics toolbox.

In Chap. 3, a quantum method of imaging phase-only objects was presented, and it was shown to be twice as sensitive as classical phase imaging. Furthermore, the resolution of this quantum phase imaging scheme achieved approximately 1.7 times the resolution of classical quantitative phase imaging, though the resolution enhancement was not quantum in origin. The physical origin of the interference that enabled this method, namely induced coherence without induced emission, was described theoretically. Numerical simulations of both the quantum and classical imaging systems agreed closely with experimental results. Because the phase object was only illuminated with approximately 40 photons/s/μm^2, the quantum phase imaging method in Chap. 3 is well-suited for imaging light-sensitive biological samples. When compared to low-light quantum imaging protocols that rely upon measuring photons in coincidence, data collection times using our method are nearly three orders of magnitude faster. As a result, Chap. 3 presents a quantum imaging method that is ready for real-world application.

Nonlinear phase distortions, namely nonlinear optical caustics, were the subject of Chap. 4, and the results of Chap. 4 showed that polarization-structured full-Poincaré beams can transmit more power than uniformly polarized beams without developing into caustics. Numerical simulations of a phenomenological nonlinear self-focusing model agreed well with experimental results. Importantly, the results of this chapter were obtained without using a high power laser system. Instead, a moderately powered laser (approximately 100 mW) was tuned close to the D2 transition in atomic Rb vapor to achieve similar nonlinear self-focusing conditions. Chapter 4 adds more understanding to the literature surrounding the behavior and uses of polarization-structured light.

With an eye toward the future, Chap. 5 describes a method of generating polarization-structured beams that contain states of both full and partial polarization. Such beams could further increase the resistance of high intensity laser beams to nonlinear beam breakup and may find use in optical communications, imaging, or remote sensing. This method is demonstrated by generating a beam that contains every possible state of polarization at some location in its transverse and longitudinal extent, a volumetrically-full Poincaré beam. Structured light generation has received a significant amount of attention over the last couple of decades, and our method represents a new to addition to this popular area of research.

New experiments that extend the ideas of this thesis are already underway within our group. A two-color version of the experiment in Chap. 2 has been constructed and is awaiting data collection. Additionally, nonlocal aberration cancellation is being explored by members of our group as an encryption method similar to orthogonal optical coding. We are currently constructing a high numerical aperture microscope in conjunction with researchers at the Pacific Northwest National Lab to apply quantum-enhanced phase imaging in the study of Chlamydomonas reinhardtii, a light-sensitive alga studied for biofuel production. We are also developing ways to use non-degenerate SPDC to improve quantitative phase imaging. Building upon the results of Chap. 4, our group is generating polarization knot beams and studying their behavior under nonlinear propagation. An experiment is also underway to measure the stability of volumetrically-full Poincaré beams under conditions of small-scale filamentation. The experiments listed above will improve upon the ideas presented in this thesis and create new ways to utilize, mitigate, and characterize phase distortions in quantum and nonlinear optical systems.

Bibliography

[1] M. Berry and C. Upstill, “IV Catastrophe Optics: Morphologies of caustics and their diffraction patterns”, in Progress in Optics, Vol. 18, edited by E. Wolf (1980), pp. 257–346.

[2] M. Born and E. Wolf, *Principles of optics* (Cambridge University Press, Cambridge, UK, 1999) Chap. 3, pp. 136–138.

[3] R. W. Boyd, *Nonlinear optics*, Fourth edition. (Academic Press, San Diego, 2020) Chap. 1, p. 5.

[4] E. M. Nagasako, R. W. Boyd, and G. S. Agarwal, “Quantum fluctuations as the origin of laser beam filamentation”, in Coherence and Quantum Optics VII, edited by J. H. Eberly, L. Mandel, and E. Wolf (1996), pp. 637–638.

[5] M. Malik, M. O’Sullivan, B. Rodenburg, M. Mirhosseini, J. Leach, M. P. J. Lavery, M. J. Padgett, and R. W. Boyd, “Influence of atmospheric turbulence on optical communications using orbital angular momentum for encoding”, Opt. Express **20**, 13195 (2012).

[6] J. Kasparian et al., “White-light filaments for atmospheric analysis”, Science **301**, 61 (2003).

[7] T. Produit et al., “The laser lightning rod project”, Eur. Phys. J. Appl. Phys. **93**, 10504 (2021).

[8] J. Hecht, “Laser weapons not ready for missile defense”, IEEE Spectrum (2017).

[9] Y. Niwa, T. Matsuo, K. Onai, D. Kato, M. Tachikawa, and M. Ishiura, “Phase-resetting mechanism of the circadian clock in *Chlamydomonas reinhardtii*”, Proceedings of the National Academy of Sciences **110**, 13666 (2013).

[10] Q. Thommen, B. Pfeuty, P. Schatt, A. Bijoux, F.-Y. Bouget, and M. Lefranc, “Probing entrainment of Ostreococcus tauri circadian clock by green and blue light through a mathematical modeling approach”, Frontiers in Genetics **6**, 65 (2015).

[11] H. Defienne, M. Reichert, and J. W. Fleischer, “General model of photon-pair detection with an image sensor”, Phys. Rev. Lett. **120**, 203604 (2018).

[12] A. Safari, R. Fickler, M. J. Padgett, and R. W. Boyd, “Generation of caustics and rogue waves from nonlinear instability”, Phys. Rev. Lett. **119**, 203901 (2017).

[13] F. Bouchard, H. Larocque, A. M. Yao, C. Travis, I. De Leon, A. Rubano, E. Karimi, G.-L. Oppo, and R. W. Boyd, “Polarization shaping for control of nonlinear propagation”, Phys. Rev. Lett. **117**, 233903 (2016).

[14] S. Ramachandran, P. Kristensen, and M. F. Yan, “Generation and propagation of radially polarized beams in optical fibers”, Opt. Lett. **34**, 2525 (2009).

[15] L. Sá and J. Vieira, “Self-focusing of multiple interacting Laguerre-Gauss beams in Kerr media”, Phys. Rev. A **100**, 013836 (2019).

[16] W. J. Firth and D. V. Skryabin, “Optical solitons carrying orbital angular momentum”, Phys. Rev. Lett. **79**, 2450 (1997).

[17] M. S. Bigelow, P. Zerom, and R. W. Boyd, “Breakup of ring beams carrying orbital angular momentum in sodium vapor”, Phys. Rev. Lett. **92**, 083902 (2004).

[18] A. Einstein, B. Podolsky, and N. Rosen, “Can quantum-mechanical description of physical reality be considered complete?”, Phys. Rev. **47**, 777 (1935).

[19] J.-P. W. MacLean, J. M. Donohue, and K. J. Resch, “Direct characterization of ultrafast energy-time entangled photon pairs”, Phys. Rev. Lett. **120**, 053601 (2018).

[20] J. C. Howell, R. S. Bennink, S. J. Bentley, and R. W. Boyd, “Realization of the Einstein-Podolsky-Rosen paradox using momentum- and position-entangled photons from spontaneous parametric down conversion”, Phys. Rev. Lett. **92**, 210403 (2004).

[21] P. G. Kwiat, K. Mattle, H. Weinfurter, and A. Zeilinger, “New high-intensity source of polarization-entangled photon pairs”, Phys. Rev. Lett. **75**, 4337 (1995).

[22] A. Mair, A. Vaziri, G. Weihs, and A. Zeilinger, “Entanglement of the orbital angular momentum states of photons”, Nature **412**, 313 (2001).

[23] K. W. Chan, J. P. Torres, and J. H. Eberly, “Transverse entanglement migration in Hilbert space”, Phys. Rev. A **75**, 050101 (2007).

[24] J. D. Franson, “Nonlocal cancellation of dispersion”, Phys. Rev. A **45**, 3126 (1992).

[25] A. M. Steinberg, P. G. Kwiat, and R. Y. Chiao, “Dispersion cancellation in a measurement of the single-photon propagation velocity in glass”, Phys. Rev. Lett. **68**, 2421 (1992).

[26] O. Minaeva, C. Bonato, B. E. A. Saleh, D. S. Simon, and A. V. Sergienko, “Odd- and even-order dispersion cancellation in quantum interferometry”, Phys. Rev. Lett. **102**, 100504 (2009).

[27] J. M. Lukens, A. Dezfooliyan, C. Langrock, M. M. Fejer, D. E. Leaird, and A. M. Weiner, “Orthogonal spectral coding of entangled photons”, Phys. Rev. Lett. **112**, 133602 (2014).

[28] J. H. Shapiro, “Dispersion cancellation with phase-sensitive Gaussian-state light”, Phys. Rev. A **81**, 023824 (2010).

[29] V. Torres-Company, J. P. Torres, and A. T. Friberg, "Shaping the ultrafast temporal correlations of thermal-like photons", Phys. Rev. Lett. **109**, 243905 (2012).

[30] J. W. Goodman, *Introduction to Fourier optics* (Roberts and Company, Englewood, CO, 2005).

[31] C. Bonato, A. V. Sergienko, B. E. A. Saleh, S. Bonora, and P. Villoresi, "Even-order aberration cancellation in quantum interferometry", Phys. Rev. Lett. **101**, 233603 (2008).

[32] L. A. P. Filpi, M. V. da Cunha Pereira, and C. H. Monken, "Experimental observation of aberration cancellation in entangled two-photon beams", Opt. Express **23**, 3841 (2015).

[33] H. Defienne, M. Reichert, and J. W. Fleischer, "Adaptive quantum optics with spatially entangled photon pairs", Phys. Rev. Lett. **121**, 233601 (2018).

[34] S. Cialdi, D. Brivio, E. Tesio, and M. G. A. Paris, "Nonlocal compensation of pure phase objects with entangled photons", Phys. Rev. A **84**, 043817 (2011).

[35] D. S. Simon and A. V. Sergienko, "Correlated-photon imaging with cancellation of object-induced aberration", J. Opt. Soc. Am. B **28**, 247 (2011).

[36] D. V. Strekalov, A. V. Sergienko, D. N. Klyshko, and Y. H. Shih, "Observation of two-photon "ghost" interference and diffraction", Phys. Rev. Lett. **74**, 3600 (1995).

[37] T. B. Pittman, Y. H. Shih, D. V. Strekalov, and A. V. Sergienko, "Optical imaging by means of two-photon quantum entanglement", Phys. Rev. A **52**, R3429 (1995).

[38] M. H. Rubin, D. N. Klyshko, Y. H. Shih, and A. V. Sergienko, "Theory of two-photon entanglement in type-II optical parametric down-conversion", Phys. Rev. A **50**, 5122 (1994).

[39] S. P. Walborn, C. H. Monken, S. Pádua, and P. H. Souto Ribeiro, "Spatial correlations in parametric down-conversion", Phys. Rep. **495**, 87 (2010).

[40] L. Mandel and E. Wolf, *Optical coherence and quantum optics* (Cambridge University Press, Cambridge, UK, 2013).

[41] M. H. Rubin, "Transverse correlation in optical spontaneous parametric down-conversion", Phys. Rev. A **54**, 5349 (1996).

[42] R. W. Boyd, *Nonlinear optics*, Fourth edition. (Academic Press, San Diego, 2020) Chap. 1, pp. 23–26.

[43] R. W. Boyd, *Nonlinear optics*, Fourth edition. (Academic Press, San Diego, 2020) Chap. 2, p. 78.

[44] A. K. Jha and R. W. Boyd, "Spatial two-photon coherence of the entangled field produced by down-conversion using a partially spatially coherent pump beam", Phys. Rev. A **81**, 013828 (2010).

[45] E. Giese, R. Fickler, W. Zhang, L. Chen, and R. W. Boyd, “Influence of pump coherence on the quantum properties of spontaneous parametric down-conversion”, Phys. Scr. **93**, 084001 (2018).

[46] J. W. Goodman, *Introduction to Fourier optics* (Roberts and Company, 2005) Chap. 2, p. 8.

[47] R. S. Bennink, S. J. Bentley, and R. W. Boyd, “"Two-photon" coincidence imaging with a classical source”, Phys. Rev. Lett. **89**, 113601 (2002).

[48] F. Ferri, D. Magatti, A. Gatti, M. Bache, E. Brambilla, and L. A. Lugiato, “High-resolution ghost image and ghost diffraction experiments with thermal light”, Phys. Rev. Lett. **94**, 183602 (2005).

[49] J. E. Greivenkamp, *Field guide to geometrical optics* (SPIE Press, Bellingham, WA, USA, 2004), p. 70.

[50] G. J. Gbur, *Mathematical methods for optical physics and engineering* (Cambridge University Press, Cambridge, UK, 2011) Chap. 18, pp. 655–662.

[51] M. Born and E. Wolf, *Principles of optics*, 7th ed. (Cambridge University Press, Cambridge, UK, 1999) Chap. 9, pp. 523–525.

[52] E. Goodwin and W. J. C., *Field guide to interferometric optical testing* (SPIE Press, Bellingham, WA, USA, 2006), p. 24.

[53] S. Mancini, V. Giovannetti, D. Vitali, and P. Tombesi, “Entangling macroscopic oscillators exploiting radiation pressure”, Phys. Rev. Lett. **88**, 120401 (2002).

[54] D. S. Tasca, S. P. Walborn, P. H. Souto Ribeiro, F. Toscano, and P. Pellat-Finet, “Propagation of transverse intensity correlations of a two-photon state”, Phys. Rev. A **79**, 033801 (2009).

[55] D. Branning, S. Bhandari, and M. Beck, “Low-cost coincidence-counting electronics for undergraduate quantum optics”, Am. J. Phys. **77**, 667 (2009).

[56] T. S. Larchuk, M. C. Teich, and B. E. A. Saleh, “Statistics of entangled-photon coincidences in parametric downconversion”, Annals of the New York Academy of Sciences **755**, 680 (1995).

[57] A. N. Black, E. Giese, B. Braverman, N. Zollo, and R. W. Boyd, “Nonlocal aberration cancellation with entangled photons”, in Proc. of the 49th winter colloquium on the physics of quantum electronics (2019).

[58] R. S. Aspden, N. R. Gemmell, P. A. Morris, D. S. Tasca, L. Mertens, M. G. Tanner, R. A. Kirkwood, A. Ruggeri, A. Tosi, R. W. Boyd, G. S. Buller, R. H. Hadfield, and M. J. Padgett, “Photon-sparse microscopy: visible light imaging using infrared illumination”, Optica **2**, 1049 (2015).

[59] F. Zernike, “How I discovered phase contrast”, Science **121**, 345 (1955).

[60] G. Nomarski, “Microinterféromètre differntielle à ondes polarisées”, J. Phys. Radium **16**, 9 (1955).

[61] J. H. Bruning, D. R. Herriott, J. E. Gallagher, D. P. Rosenfeld, A. D. White, and D. J. Brangaccio, "Digital wavefront measuring interferometer for testing optical surfaces and lenses", Appl. Opt. **13**, 2693 (1974).

[62] I. Yamaguchi and T. Zhang, "Phase-shifting digital holography", Opt. Lett. **22**, 1268 (1997).

[63] E. Cuche, P. Marquet, and C. Depeursinge, "Spatial filtering for zero-order and twin-image elimination in digital off-axis holography", Appl. Opt. **39**, 4070 (2000).

[64] V. Giovannetti, S. Lloyd, L. Maccone, and J. H. Shapiro, "Sub-Rayleigh-diffraction-bound quantum imaging", Phys. Rev. A **79**, 013827 (2009).

[65] M. Reichert, H. Defienne, and J. W. Fleischer, "Massively parallel coincidence counting of high-dimensional entangled states", Scientific Reports **8**, 7925 (2018).

[66] H. Defienne, M. Reichert, and J. W. Fleischer, "Adaptive quantum optics with spatially entangled photon pairs", Phys. Rev. Lett. **121**, 233601 (2018).

[67] A. N. Black, E. Giese, B. Braverman, N. Zollo, S. M. Barnett, and R. W. Boyd, "Quantum nonlocal aberration cancellation", Phys. Rev. Lett. **123**, 143603 (2019).

[68] N. H. Valencia, S. Goel, W. McCutcheon, H. Defienne, and M. Malik, "Unscrambling entanglement through a complex medium", Nature Physics **16**, 1112 (2020).

[69] T. Aidukas, P. C. Konda, A. R. Harvey, M. J. Padgett, and P.-A. Moreau, "Phase and amplitude imaging with quantum correlations through Fourier ptychography", Scientific Reports **9**, 10445 (2019).

[70] H. Defienne, B. Ndagano, A. Lyons, and D. Faccio, "Polarization entanglement-enabled quantum holography", Nature Physics **17**, 591 (2021).

[71] R. Camphausen, Á. Cuevas, L. Duempelmann, R. A. Terborg, E. Wajs, S. Tisa, A. Ruggeri, I. Cusini, F. Steinlechner, and V. Pruneri, "A quantum-enhanced wide-field phase imager", Science Advances **7**, eabj2155 (2021).

[72] X. Y. Zou, L. J. Wang, and L. Mandel, "Induced coherence and indistinguishability in optical interference", Phys. Rev. Lett. **67**, 318 (1991).

[73] G. B. Lemos, V. Borish, G. D. Cole, S. Ramelow, R. Lapkiewicz, and A. Zeilinger, "Quantum imaging with undetected photons", Nature **512**, 409 (2014).

[74] J. H. Shapiro, D. Venkatraman, and F. N. C. Wong, "Classical imaging with undetected photons", Scientific Reports **5**, 10329 (2015).

[75] A. C. Cardoso, L. P. Berruezo, D. F. Ávila, G. B. Lemos, W. M. Pimenta, C. H. Monken, P. L. Saldanha, and S. Pádua, "Classical imaging with undetected light", Phys. Rev. A **97**, 033827 (2018).

[76] I. Kviatkovsky, H. M. Chrzanowski, E. G. Avery, H. Bartolomaeus, and S. Ramelow, "Microscopy with undetected photons in the mid-infrared", Science Advances **6**, eabd0264 (2020).

[77] A. V. Paterova, H. Yang, Z. S. D. Toa, and L. A. Krivitsky, "Quantum imaging for the semiconductor industry", Applied Physics Letters **117**, 054004 (2020).

[78] D. A. Kalashnikov, A. V. Paterova, S. P. Kulik, and L. A. Krivitsky, "Infrared spectroscopy with visible light", Nature Photonics **10**, 98 (2016).

[79] B. Viswanathan, G. B. Lemos, and M. Lahiri, "Resolution limit in quantum imaging with undetected photons using position correlations", Opt. Express **29**, 38185 (2021).

[80] M. Reichert, H. Defienne, and J. W. Fleischer, "Optimizing the signal-to-noise ratio of biphoton distribution measurements", Phys. Rev. A **98**, 013841 (2018).

[81] T. Gregory, P.-A. Moreau, E. Toninelli, and M. J. Padgett, "Imaging through noise with quantum illumination", Science Advances **6**, eaay2652 (2020).

[82] P. A. Morris, R. S. Aspden, J. E. C. Bell, R. W. Boyd, and M. J. Padgett, "Imaging with a small number of photons", Nature Communications **6**, 5913 (2015).

[83] A. Nomerotski, "Imaging and time stamping of photons with nanosecond resolution in Timepix based optical cameras", Nuclear Instruments and Methods in Physics Research Section A: Accelerators, Spectrometers, Detectors and Associated Equipment **937**, 26 (2019).

[84] O. Wolley, T. Gregory, S. Beer, T. Higuchi, and M. Padgett, "Quantum imaging with a photon counting camera", Scientific Reports **12**, 8286 (2022).

[85] D. Bouchet, J. Dong, D. Maestre, and T. Juffmann, "Fundamental bounds on the precision of classical phase microscopes", Phys. Rev. Applied **15**, 024047 (2021).

[86] G. Frascella, E. E. Mikhailov, N. Takanashi, R. V. Zakharov, O. V. Tikhonova, and M. V. Chekhova, "Wide-field SU(1,1) interferometer", Optica **6**, 1233 (2019).

[87] E. Lantz, J.-L. Blanchet, L. Furfaro, and F. Devaux, "Multi-imaging and Bayesian estimation for photon counting with emccds", Monthly Notices of the Royal Astronomical Society **386**, 2262 (2008).

[88] I. F. Santos, M. A. Sagioro, C. H. Monken, and S. Pádua, "Resolution and apodization in images generated by twin photons", Phys. Rev. A **67**, 033812 (2003).

[89] J. W. Goodman, *Introduction to Fourier optics* (Roberts and Company, 2005) Chap. 5, p. 116.

[90] S. Chowdhury, A.-H. Dhalla, and J. Izatt, "Structured oblique illumination microscopy for enhanced resolution imaging of non-fluorescent, coherently scattering samples", Biomed. Opt. Express **3**, 1841 (2012).

[91] J. W. Goodman, *Introduction to Fourier optics* (Roberts and Company, Englewood, CO, 2005).

[92] P. H. S. Ribeiro, C. H. Monken, and G. A. Barbosa, "Measurement of coherence area in parametric downconversion luminescence", Appl. Opt. **33**, 352 (1994).

[93] J. W. Goodman, *Introduction to fourier optics* (Roberts and Company, Englewood, CO, 2005).

[94] R. Nold, C. Babin, J. Schmidt, T. Linkewitz, M. T. P. Zaballos, R. Stöhr, R. Kolesov, V. Vorobyov, D. M. Lukin, R. Boppert, S. Barz, J. Vu čkovi ć, J. C. M. Gebhardt, F. Kaiser, and J. Wrachtrup, "Quantum optical microphone in the audio band", PRX Quantum **3**, 020358 (2022).

[95] V. I. Arnol'd, "Critical points of smooth functions and their normal forms", Russ. Math. Surv. **30**, 1 (1975).

[96] R. Thom, *Structural stability and morphogenesis* (W. A. Benjamin, Inc., Reading, MA, 1975) Chap. 5.

[97] M. Naghiloo, D. Tan, P. M. Harrington, P. Lewalle, A. N. Jordan, and K. W. Murch, "Quantum caustics in resonance-fluorescence trajectories", Phys. Rev. A **96**, 053807 (2017).

[98] D. Pierangeli, F. Di Mei, C. Conti, A. J. Agranat, and E. DelRe, "Spatial rogue waves in photorefractive ferroelectrics", Phys. Rev. Lett. **115**, 093901 (2015).

[99] A. M. Deykoon, M. S. Soskin, and G. A. Swartzlander, "Nonlinear optical catastrophe from a smooth initial beam", Opt. Lett. **24**, 1224 (1999).

[100] G. A. Swartzlander and A. E. Kaplan, "Self-deflection of laser beams in a thin nonlinear film", J. Opt. Soc. Am. B **5**, 765 (1988).

[101] R. W. Boyd, *Nonlinear optics*, Fourth edition. (Academic Press, San Diego, 2020) Chap. 7, p. 322.

[102] R. Y. Chiao, E. Garmire, and C. H. Townes, "Self-trapping of optical beams", Phys. Rev. Lett. **13**, 479 (1964).

[103] G. A. Swartzlander and C. T. Law, "Optical vortex solitons observed in Kerr nonlinear media", Phys. Rev. Lett. **69**, 2503 (1992).

[104] Z. Chen, M. Segev, and D. N. Christodoulides, "Optical spatial solitons: historical overview and recent advances", Reports on Progress in Physics **75**, 086401 (2012).

[105] T. Ackemann, E. Kriege, and W. Lange, "Phase singularities via nonlinear beam propagation in sodium vapor", Optics Communications **115**, 339 (1995).

[106] L. Kreminskaya, M. Soskin, and A. Khizhnyak, "The Gaussian lenses give birth to optical vortices in laser beams", Optics Communications **145**, 377 (1998).

[107] A. Chabchoub and M. Fink, "Time-reversal generation of rogue waves", Phys. Rev. Lett. **112**, 124101 (2014).

[108] L. G. Wright, Z. Liu, D. A. Nolan, M.-J. Li, D. N. Christodoulides, and F. W. Wise, "Self-organized instability in graded-index multimode fibres", Nature Photonics **10**, 771 (2016).

[109] D. W. Koopman and T. D. Wilkerson, “Channeling of an ionizing electrical streamer by a laser beam”, Journal of Applied Physics **42**, 1883 (1971).

[110] X. M. Zhao, J.-C. Diels, C. Y. Wang, and J. Elizondo, “Femtosecond ultraviolet laser pulse induced lightning discharges in gases”, IEEE Journal of Quantum Electronics **31**, 599 (1995).

[111] G. Gibson, J. Courtial, M. J. Padgett, M. Vasnetsov, V. Pas’ko, S. M. Barnett, and S. Franke-Arnold, “Free-space information transfer using light beams carrying orbital angular momentum”, Opt. Express **12**, 5448 (2004).

[112] N. Bozinovic, Y. Yue, Y. Ren, M. Tur, P. Kristensen, H. Huang, A. E. Willner, and S. Ramachandran, “Terabit-scale orbital angular momentum mode division multiplexing in fibers”, Science **340**, 1545 (2013).

[113] Y. Yan et al., “High-capacity millimetre-wave communications with orbital angular momentum multiplexing”, Nature Communications **5**, 4876 (2014).

[114] Y. Zhou, B. Braverman, A. Fyffe, R. Zhang, J. Zhao, A. E. Willner, Z. Shi, and R. W. Boyd, “High-fidelity spatial mode transmission through a 1-km-long multimode fiber via vectorial time reversal”, Nature Communications **12**, 1866 (2021).

[115] L. T. Vuong, T. D. Grow, A. Ishaaya, A. L. Gaeta, G. W. ’t Hooft, E. R. Eliel, and G. Fibich, “Collapse of optical vortices”, Phys. Rev. Lett. **96**, 133901 (2006).

[116] H. Larocque, A. D’Errico, M. F. Ferrer-Garcia, A. Carmi, E. Cohen, and E. Karimi, “Optical framed knots as information carriers”, Nature Communications **11**, 5119 (2020).

[117] G. Milione, H. I. Sztul, D. A. Nolan, and R. R. Alfano, “Higher-order Poincaré sphere, Stokes parameters, and the angular momentum of light”, Phys. Rev. Lett. **107**, 053601 (2011).

[118] A. Sit, R. Fickler, F. Alsaiari, F. Bouchard, H. Larocque, P. Gregg, L. Yan, R. W. Boyd, S. Ramachandran, and E. Karimi, “Quantum cryptography with structured photons through a vortex fiber”, Opt. Lett. **43**, 4108 (2018).

[119] Q. Zhan, “Cylindrical vector beams: from mathematical concepts to applications”, Adv. Opt. Photon. **1**, 1 (2009).

[120] A. M. Beckley, T. G. Brown, and M. A. Alonso, “Full Poincaré beams”, Optics Express **18**, 10777 (2010).

[121] G. Gbur, *Singular optics*, Series in optics and optoelectronics (CRC Press, Boca Raton, 2017).

[122] A. M. Beckley, T. G. Brown, and M. A. Alonso, “Full Poincaré beams II: partial polarization”, Optics Express **20**, 9357 (2012).

[123] Y. Gu, O. Korotkova, and G. Gbur, “Scintillation of nonuniformly polarized beams in atmospheric turbulence”, Opt. Lett. **34**, 2261 (2009).

[124] S.-M. Li, Y. Li, X.-L. Wang, L.-J. Kong, K. Lou, C. Tu, Y. Tian, and H.-T. Wang, "Taming the collapse of optical fields", Scientific Reports **2**, 1007 (2012).

[125] H. Hu, D. Luo, C. Pan, Y. Qin, Y. Zhang, D. Wei, H. Chen, H. Gao, and F. Li, "Collapse of hybrid vector beam in Rb atomic vapor", Opt. Lett. **46**, 2614 (2021).

[126] M. Soljačić, S. Sears, and M. Segev, "Self-trapping of "necklace" beams in self-focusing Kerr media", Phys. Rev. Lett. **81**, 4851 (1998).

[127] J. H. Eberly, X.-F. Qian, A. A. Qasimi, H. Ali, M. A. Alonso, R. Gutiérrez-Cuevas, B. J. Little, J. C. Howell, T. Malhotra, and A. N. Vamivakas, "Quantum and classical optics–emerging links", Physica Scripta **91**, 063003 (2016).

[128] E. Karimi and R. W. Boyd, "Classical entanglement?", Science **350**, 1172 (2015).

[129] K. Khare, P. Lochab, and P. Senthilkumaran, *Orbital angular momentum states of light*, 2053-2563 (IOP Publishing, 2020).

[130] G. Agrawal, *Nonlinear fiber optics*, Sixth edition. (Academic Press, London, England, 2019).

[131] M. D. Feit and J. A. Fleck, "Beam nonparaxiality, filament formation, and beam breakup in the self-focusing of optical beams", J. Opt. Soc. Am. B **5**, 633 (1988).

[132] M. S. Bigelow, Q.-H. Park, and R. W. Boyd, "Stabilization of the propagation of spatial solitons", Phys. Rev. E **66**, 046631 (2002).

[133] J. R. Salgueiro and Y. S. Kivshar, "Single- and double-vortex vector solitons in self-focusing nonlinear media", Phys. Rev. E **70**, 056613 (2004).

[134] L. Cheng, Z. Zhang, L. Zhang, D. Ma, G. Yang, T. Dong, and Y. Zhang, "Manipulation of a ring-shaped beam via spatial self- and cross-phase modulation at lower intensity", Phys. Chem. Chem. Phys. **21**, 7618 (2019).

[135] M. Jain, A. J. Merriam, A. Kasapi, G. Y. Yin, and S. E. Harris, "Elimination of optical self-focusing by population trapping", Phys. Rev. Lett. **75**, 4385 (1995).

[136] P. Siddons, C. S. Adams, C. Ge, and I. G. Hughes, "Absolute absorption on rubidium D lines: comparison between theory and experiment", Journal of Physics B: Atomic, Molecular and Optical Physics **41**, 155004 (2008).

[137] D. H. Close, "Strong-field saturation effects in laser media", Phys. Rev. **153**, 360 (1967).

[138] C. F. McCormick, D. R. Solli, R. Y. Chiao, and J. M. Hickmann, "Saturable nonlinear refraction in hot atomic vapor", Phys. Rev. A **69**, 023804 (2004).

[139] D. Steck, *Rubidium 87 D line data* (2021).

[140] P. K. Vudyasetu, D. J. Starling, and J. C. Howell, "All optical waveguiding in a coherent atomic rubidium vapor", Phys. Rev. Lett. **102**, 123602 (2009).

[141] J. W. Goodman, *Speckle phenomena in optics* (Society of Photo-Optical Instrumentation Engineers, Bellingham, 2020) Chap. 3, p. 29.

[142] V. Arrizón, U. Ruiz, R. Carrada, and L. A. González, "Pixelated phase computer holograms for the accurate encoding of scalar complex fields", J. Opt. Soc. Am. A **24**, 3500 (2007).

[143] H. Frostig, E. Small, A. Daniel, P. Oulevey, S. Derevyanko, and Y. Silberberg, "Focusing light by wavefront shaping through disorder and nonlinearity", Optica **4**, 1073 (2017).

[144] R. H. Jordan and D. G. Hall, "Free-space azimuthal paraxial wave equation: the azimuthal Bessel–Gauss beam solution", Opt. Lett. **19**, 427 (1994).

[145] M. S. Soskin and M. V. Vasnetsov, "Nonlinear singular optics", Pure and Applied Optics: Journal of the European Optical Society Part A **7**, 301 (1998).

[146] H. Rubinsztein-Dunlop et al., "Roadmap on structured light", Journal of Optics **19**, 013001 (2016).

[147] A. Forbes, "Structured light from lasers", Laser & Photonics Reviews **13**, 1900140 (2019).

[148] R. Dorn, S. Quabis, and G. Leuchs, "Sharper focus for a radially polarized light beam", Phys. Rev. Lett. **91**, 233901 (2003).

[149] J.-B. Béguin, J. Laurat, X. Luan, A. P. Burgers, Z. Qin, and H. J. Kimble, "Reduced volume and reflection for bright optical tweezers with radial Laguerre-Gauss beams", Proceedings of the National Academy of Sciences **117**, 26109 (2020).

[150] W. T. Tang, E. Y. S. Yew, and C. J. R. Sheppard, "Polarization conversion in confocal microscopy with radially polarized illumination", Opt. Lett. **34**, 2147 (2009).

[151] R. W. Boyd, "Intuitive explanation of the phase anomaly of focused light beams", J. Opt. Soc. Am. **70**, 877 (1980).

[152] J. M. Wheeler, J. N. Chamoun, and M. J. F. Digonnet, "Optimizing coherence suppression in a laser broadened by phase modulation with noise", Journal of Lightwave Technology **39**, 2994 (2021).